LASER TRAPPING OF ATOMS AND CAVITY QUANTUM ELECTRODYNAMICS IN FIBRE-TIP MICROCAVITIES

Jian Dong
Lincoln College

A thesis submitted for the degree of Doctor of Philosophy
Hilary Term 2014
Supervised by Dr. Axel Kuhn

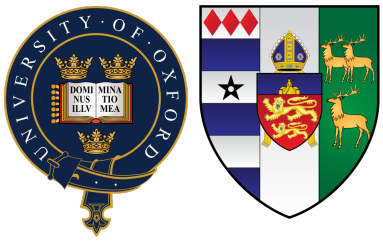

Clarendon Laboratory
Department of Physics
University of Oxford

Dedicated to my parents, Zhen Jing and Liang Feng Dong. To whom I owe my every success and whom I love more than they realise.

ABSTRACT

Constructing a quantum network comprising of matter-based *stationary* qubits and photonic *flying* qubits is a key goal towards scalable quantum computing. Individually trapped neutral atoms are amongst the most promising candidates for stationary qubits, while single photons emitted from optical cavities appears to be the best approach to forming flying qubits. This thesis presents a fast and versatile method to trap and transport an array of neutral atoms, with the aid of a spatial light modulator (SLM). We demonstrate trapped ^{87}Rb atoms adapting to the arbitrary and dynamic potential landscapes imposed by the SLM. On top of this we also investigate the inclusion of fibre-tip cavities into the experiment. In these microcavities, the mirrors are replaced by ablated fibre-tip faces, coated in a highly reflective dielectric stack. These have the benefit of small geometries, increasing their scalability; which in turns leads to extremely small mode volumes, allowing for strong coupling with atoms inside the cavity modes. We construct and characterise a high finesse $\mathcal{F} = 120,000$ fibre-tip cavity constructed from two single mode fibres.

ACKNOWLEDGEMENTS

Firstly and foremost I would like to thank my supervisor, Dr. Axel Kuhn. His guidance, support and patience have been amazing and the results in this thesis would not have been close to possible without him. I would like to thank my lab mates: Cecilia Muldoon, for the countless hours of fun in the lab and her friendship throughout my time here; Dustin Stuart, for his willingness to always help out no matter how busy he is himself; and Lukas Brandt, for setting up the foundations of the experiment. I would also like to thank the rest of the group: Oliver Barter, Annemarie Holleczek, Jerome Dilley, Gunnar Langfahl and Peter Nisbet-Jones for any help they have given me over the years. Outside the group I would like to thank all my friends at Lincoln College and throughout the University for the good times we shared, it has been an period of my life which I will look back on with great fondness.

CONTENTS

ACRONYMS

AFM Atomic Force Microscope

AOM Acousto-Optic Modulator

CCD Charge Coupled Device

DMD Digital Mirror Device

EMCCD Electron Multiplying Charge Coupled Device

FSR Free Spectral Range

FWHM Full-Width Half-Maximum

MOT Magneto-Optical Trap

MOST Magneto-Optical Surface Trap

PDH Pound-Drever-Hall

PID Proportional-Integral-Differentive

ROC Radius of Curvature

QED Quantum Electrodynamics

SEM Scanning Electron Microscope

SLM Spatial Light Modulator

TEM Transverse Electromagnetic

TOF Time-of-Flight

1

INTRODUCTION

Quantum computation has the potential of becoming a revolutionary new form of computation in the 21st century. By exploiting fundamental quantum properties (notably entanglement), it can achieve processing powers and solve problems inaccessible to classical computers. The most famous applications at present are Shor's algorithm for factorising large numbers [1], the complexity of which is the foundation of the public-key cryptography system used for most internet encryption; Grover's algorithm for searching large data sets [2]; and quantum simulation, where an entire system is created over which we have complete control and that mimics the dynamics of a more complex system [3, 4, 5].

The fundamental unit of processing in a quantum computer is the quantum bit (qubit), represented theoretically by a vector in a complex two dimensional vector space [6]. Like a classical bit, it can be in logical states $|0\rangle$ or $|1\rangle$; however, unlike a classical bit, it can also be prepared in

a coherent superposition of two states such as $\frac{1}{\sqrt{2}}(|0\rangle + |1\rangle)$. The advantage this provides over a classical bit is best illustrated with an example. In a classical computer, a register composed of four bits can be in one of 16 possible binary represented states. If this register were instead composed of four qubits, it could be prepared in a quantum superposition of all 16 configurations at once, allowing it to simultaneously represent 16 numbers. This gives the quantum computers *inherent quantum parallelism* [7], meaning that any given mathematical operation can be performed on all the represented numbers in the superposition at the same time.

The basic components of a quantum computer are much the same as for standard computation. We require a logic unit (a way to implement a universal set of one-qubit and two-qubit gates), memory (storage of the qubit information), initialisation (as well defined initial quantum state) and output (an efficient measurement technique) methods, and an interconnecting bus (to transfer information to create two qubit entaglement). These requirements, together with their scalability form the *DiVicenzo criteria* for constructing a viable quantum computer [8]. Building a quantum computer is difficult and while no ideal qubit implementation yet exists, research is being conducted in many systems including Rydberg atoms [9, 10], quantum dots [11, 12, 13] and super-

conducting circuits [14, 15]. However the most promising technologies to date involve trapped atoms/ions with single photons.

These are arranged into a scalable quantum network consisting of matter-based *stationary* qubits forming an array, and photonic *flying* qubits connecting the nodes [16, 17]. Popular candidates for stationary atoms include trapped ion strings [18, 19, 20], magnetically trapped atoms above atom chips [21, 22] and optically trapped individual atoms [23, 24]. While single photon sources from optical cavities provide a suitable implementation of flying qubits [25, 26, 27]. This scheme theoretically satisfies all of the DiVicenzo criteria, with many aspects having already been demonstrated experimentally [28].

We propose the use of a spatial light modulator (SLM) to create arbitrarily shaped dipole trapping potentials. The SLM, which is easily re-configurable, can be used to trap an array of neutral atoms (which constitute our stationary qubits) and guide them as we desire. So far we have investigated how trapped atoms adapt to changes in potential landscape, and used this to move them to varying locations. We wish to use this precise atomic control to place atoms within optical cavities to enhance interaction between photon and atom, which is otherwise weak in free space. This would allows us to entangle the atom with a photon emitted from the cavity [25], providing our flying qubit.

In the theory of quantum electrodynamics (QED), the seemingly stochastic process of spontaneous emission of a photon from an excited atom can be considered as a stimulated emission induced by the vacuum fluctuations of a quantized electromagnetic field. This interaction with vacuum is dependent on the number of electromagnetic modes with which the atom is interacting. With the use of a resonant optical cavity, it is possible to engineer one vacuum interaction to be dominant over the rest, enhancing the change of spontaneous emission into that particular mode. The strength of this enhancement will depend on the specific characteristics on the cavity, which is explored in detail in Chapter 5. In the case where the coupling of the atom to the vacuum mode of the cavity, g is less than the emission rate into free space γ or the decay of a photon from the cavity κ, we lie in the *weak coupling* regime. This means that photons are lost from the atom-cavity system faster than the characteristic interaction time between the atom and the cavity. The emission of light by such a system is therefore irreversible, just as for emission into free space. Although it is possible to perform quantum computation through a network of weakly coupled atom-cavities systems, via measurement based schemes such as [29], a strongly coupled atom-cavity network is the focus of this thesis. For $g > \kappa, \gamma$ we enter the *strong coupling* regime, where the atom emits a photon into a

resonant mode and can be re-absorbed by the atom at a rate faster than it is lost from the mode. This allows for the internal state of an atom to be coherently transferred to a photon. If this photon leaks out of the cavity, propagates along a transmission line to another atom in a cavity, it can be mapped on the quantum state of the second atom. This is basis of the quantum internet of distributed quantum systems [16] and is the goal of our experiment.

There are many implementations of optical cavities used in active areas of research. These including high quality Fabry-Pérot cavities [30], toroidal cavities [31] and tapered fibres [32]. But the two types best suited to our experiment were photonic band-gap cavities [33, 34, 35] and fibre-tip cavities [36, 37, 38, 39]. For reasons explained in Section 4.3, photonic bandgap crystals proved not viable, and so we proceed with a fibre-tip cavity design.

Fibre-tip microcavities are fabricated by ablating the tip of a bare fibre with a high power laser, creating a smooth concave depression [40]. These are then coated with a highly reflective dielectric coating, forming the mirrors of the cavity. They have the advantage of having an extremely small geometry, which in turn leads to small cavity mode volumes. This allows for high cooperativities and strong coupling with atoms placed inside the mode. We have constructed such a cavity using

two coated single mode fibres and charactered its finesse and polarisation dependence.

Beyond this introduction, the thesis is presented in three major parts. Part I mainly focuses on the proposed system of delivering individually dipole trapped atoms. The results presented were collected in conjunction with Cecilia Muldoon. I worked closely with her to set up the dynamic dipole trapping apparatus and collect the data. Her thesis [41] presents the more technical aspects of the experiment and our results are published in [42]. Contribution to the experiment also came from Lukas Brandt, who set up the foundations of the experiment and the MOST [43], and who presented the feasibility report of the scheme [44]; as well from Dustin Stuart, who helped in the analysis of the collected data and presentation of the paper, and who continues a redesigned version of the experiment. Chapter 2 outlines the theory behind the trapping techniques used to achieve our goal. Chapter 3 gives a conceptual description of the main components which make up the scheme, as well as summarising the most important experimental aspects. Chapter 4 presents our recorded data, demonstrating that atoms can be trapped in single or multiple static traps of arbitrary shapes; and that is possible to transport these atoms in a controlled manner using a ballistic 'release and recapture' method.

Part II focuses on cavity QED and the interaction of our trapped atoms with cavity light. The work presented in this part was undertaken by myself. Chapter 5 provides a detailed background on the theory of cavity QED and explains the benefits which make cavities a popular choice for light-matter experiments. Chapter 6 introduces fibre-tip microcavities, detailing their advantages over conventional Fabry-Pérot cavities; it also contains a proposed redesign of the dipole trap experiment with a view to including these cavities. Chapter 7 describes the fabrication technique of creating the fibre tips. Chapter 8 covers the experimental setup of creating a cavity formed from two single mode fibres, and characterises its major features.

Finally, Part III is a conclusion which provides a quick update on the current state of the dipole trapping experiment and an outlook for the formation of a quantum network.

Part I

LASER TRAPPING AND TRANSPORT OF ATOMS

2

OPTICAL TRAPPING OF NEUTRAL ATOMS

As briefly outlined in the introduction, the ultimate goal of the experiment is to use a scalable array of optical traps to dynamically control the motion of cold atoms. The eventual aim being the use of these traps to move atoms in and out of optical micro-cavities in order to realise pairwise entanglement or quantum gate operations through cavity QED [45]. The first step is to investigate the principles behind the optical traps we use and how they are loaded with the desired atoms.

2.1 THE DIPOLE TRAP

The *optical dipole trap* will be our primary mechanism for confining and moving the atoms in our experiment. The interaction between an external electromagnetic field with the dipole moment of an atom perturbs the energy levels in what is known as the *a.c. Stark effect* or *light shift*. Fig. 2.1 shows that for a given transition driven by an intense laser

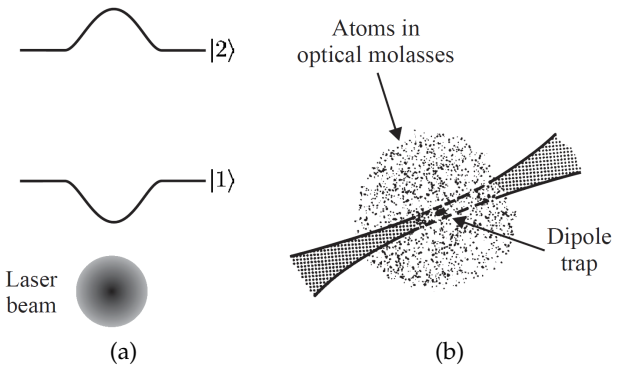

Figure 2.1: (a) The perturbation on atomic energy levels caused by an intense laser beam of Gaussian cross-section. For a laser frequency less than the atomic resonance, the a.c. Stark effect forms a potential well in the ground state energy, causing atoms to be attracted towards areas of high intensity. (b) Since dipole traps provide no intrinsic cooling, atoms to be loaded are generally pre-cooling via techniques such as the optical molasses or magneto-optical trap. Figure taken from [46].

(e.g. from the ground state to an excited state), red detuning of the beam causes the two levels of the transition to move apart; shifting the ground state down and the excited state up. The magnitude of the shift is directly proportional to the intensity of the incoming radiation, producing a potential of the form:

$$U_{dipole} \simeq \frac{\hbar\Omega^2}{4\delta} \equiv \frac{\hbar\Gamma}{8}\frac{\Gamma}{\delta}\frac{I}{I_{sat}} \tag{2.1}$$

where Ω is the Rabi frequency and δ the detuning of the trapping light away from the closest allowed atomic transition (negative for red detuning). Γ is the decay rate of this transition, I the intensity of the trapping light and I_{sat} the saturation intensity for the trapped atom. The result-

ing potential well causes atoms to experience a force towards areas of high intensity, known as the *dipole force*.

Notice that the dipole force is proportional only to the displacement of the atom from the point of maximum intensity: a restorative force with no damping term. Dipole traps are also typically very shallow (in the 100 μK regime). These factors usually mean that any atoms loaded into such traps must be first be pre-cooled.

2.2 THE MAGNETO-OPTICAL TRAP

A combination of strong damping and confinement makes the *magneto-optical trap* (MOT) extremely easy to load and one of the most widely used traps in atomic physics experiments. It provides the ideal candidate for producing a source of cold atoms with which to load our dipole traps. The MOT is based on a technique known as the *optical molasses*, which makes use of six counter propagating laser beams to provide Doppler cooling along three orthogonal axes. A Doppler cooling transition is chosen within the atom which is to be trapped and the cooling beams are slightly red detuned from this transition, such that any atom with a component of velocity towards the beam will be closer to resonance and more likely to absorb photons. Any excited atom then

decays, re-emitting the photon in a random direction. The overall effect, illustrated in fig. 2.2, is a net force on the atom from the incoming beam, proportional to the speed of the atom along that direction. This force is referred to as the *scattering force* due to its reliance on the random scattering of incoming photons for the transfer of momentum. With three pairs of counter propagating beams we can cool the atom in all directions.

If we wish to apply this technique to atoms which exhibit more complex structures than the simple two level example, there must exist a closed cooling transition within the atom to allow for Doppler cooling. That is, once excited, the atom must decay back into a state which belongs to the cooling transition, since the process relies on scattering of many photons.

The result of the molasses is however, just cooling. Since the force experienced by the atom is proportional to speed only and independent of position, it experiences only a damping force and no restoring force. To convert the molasses into a trap, a magnetic field is introduced. Fig. 2.3 shows two coils set up in an anti-Helmholtz configuration to form a magnetic quadrupole field, the centre of which has zero field and uniform field gradient. This centre is aligned to coincide with where the beams of the optical molasses intersect to form the trapping region.

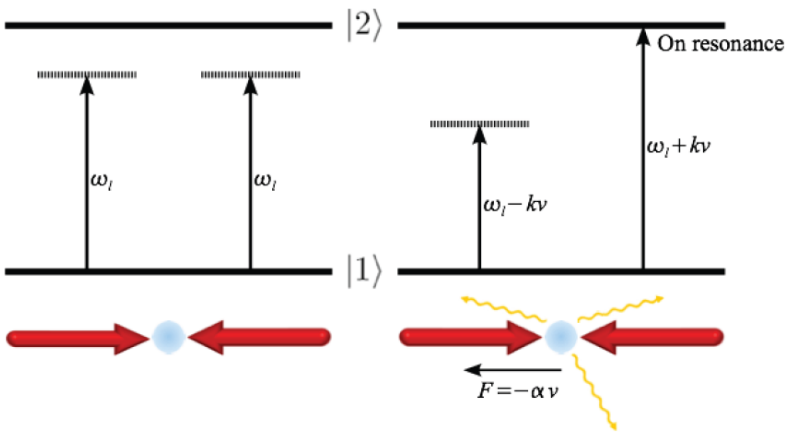

Figure 2.2: A pair of slightly red-detuned counter propagating laser beams incident on a stationary atom exerts no force on average, because the scattering rate is the same for each beam. Due to the Doppler effect, a moving atom experiences one of the beams as closer to resonance and the other further away. This leads to more scattering in the direction opposite to the atom's velocity. Figure taken from [46].

The magnetic field does not trap the atoms in and of itself, but merely serves to produce a position dependent Zeeman shift within atomic energy levels. Displacement of an atom from the centre of the field causes an uniform Zeeman shift which brings a particular magnetic energy level closer to the frequency of the detuned molasses beam, increasing excitation probability. Fig. 2.4 demonstrates that the correct polarization for each beam must now be chosen to correspond to each Zeeman shift, as specified by the dipole selection rules. This results in the inclusion of a spatially dependent restoring term in the scattering force experienced by the atom. Any trapped atoms now undergo damped harmonic motion within the MOT.

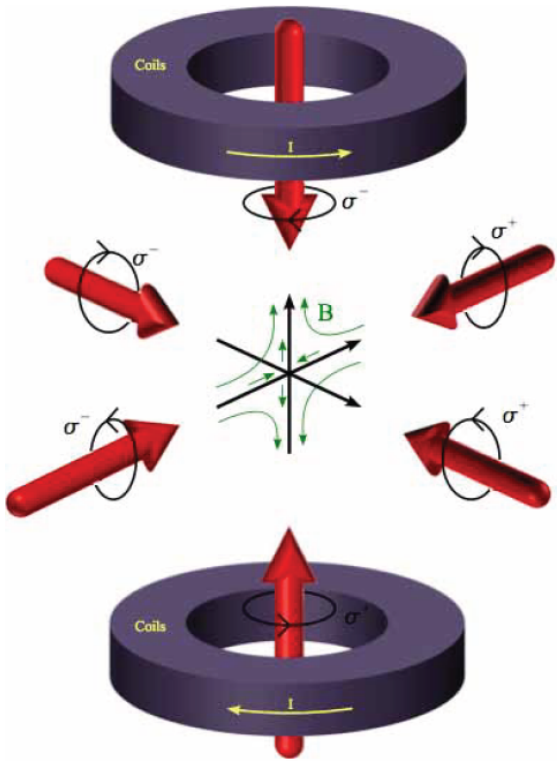

Figure 2.3: A magneto-optical trap results from a combination of an optical molasses and a pair of anti-Helmholtz coils, which generate a quadrupole magnetic field that increases linearly away from the zero point. The three orthogonal pairs of molasses beams have the requisite circular polarisation states and intersect at the centre of the pair of coils in opposite directions. Figure taken from [46].

2.2.1 *The Magneto-Optical Surface Trap*

The standard MOT must be implemented in free space, to allow all the molasses beams to cross at the centre. For reasons detailed in the following chapter, the experimental setup for our presented atomic transport method includes a dielectric mirror just below the trapping plane of the atoms. The inclusion of this mirror severely limits the optical ac-

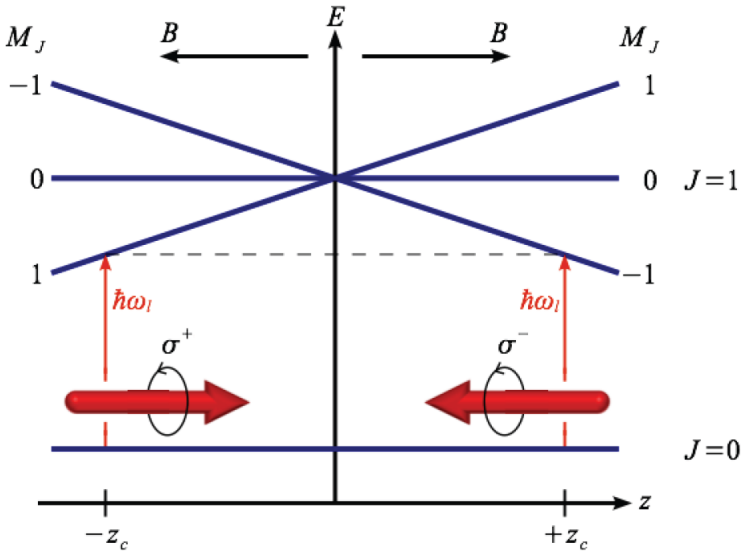

Figure 2.4: The mechanism of a magneto-optical trap illustrated for the case of an atom with a J = 0 to J = 1 transition. In the magnetic field gradient the Zeeman splitting of the sub-levels depends on the atom's position. Two counter propagating beams of circularly polarised light illuminate the atom and the selection rules for transitions between the Zeeman states lead to an imbalance in the radiative force from the laser beams that pushes the atom back towards the centre of the trap. This is not to scale; the Zeeman energy is much smaller than the optical transition energy. Figure taken from [46].

cess needed for the operation of a conventional MOT, requiring us to consider an alternative design.

The magneto-optical *surface* trap (MOST) is an adaptation of the MOT designed for cold atom experiments close to dielectric surfaces [47]. In this scheme, two axes of the molasses are created by reflecting two counter propagating, oppositely circularly polarised beams, incident at 45° to the mirror surface. Due to the finite width of the beams, a triangular region of overlapping light exists just above the surface, as show in fig. 2.5. By taking advantage of the fact that helicity of a beam

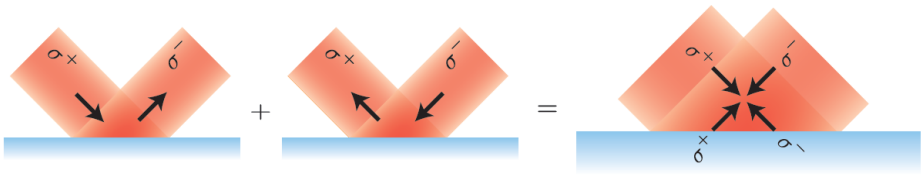

Figure 2.5: This demonstrates how an optical molasses can be formed just above a mirror surface. Two counter propagating beams of opposite circular polarisation incident the mirror at 45° to the surface. Their helicities are reversed upon reflection to effectively create two pairs of molasses beams in a triangular area just above the mirror surface. A third counter propagating circularly polarised beam runs parallel to the mirror surface and orthogonally to the two reflected beams, intersects the triangular area, forming the final molasses axes.

is inverted upon reflection, two of the three pairs of beams required for the molasses effectively exist within this area. A third retro-reflected beam, running parallel to the surface of the mirror and orthogonally to the two reflected beams, intersects the triangular area to complete the molassas.

For a MOST, the quadrupole field can still be produced by a pair of anti-Helmholtz coils, simply tilted at 45° with respect to the mirror. However, due to the nature of our vacuum chamber, this would restrict access along an optical axis crucial to our experiment. To circumvent this problem, it is possible to create an approximate quadrupole field by superimposing the magnetic field produced by a U-shaped wire, with an uniform bias field (detailed in fig. 2.6). By making the connecting bar within the U-shape flatter and wider, a much better quadrupole can be approximated near the zero point [47].

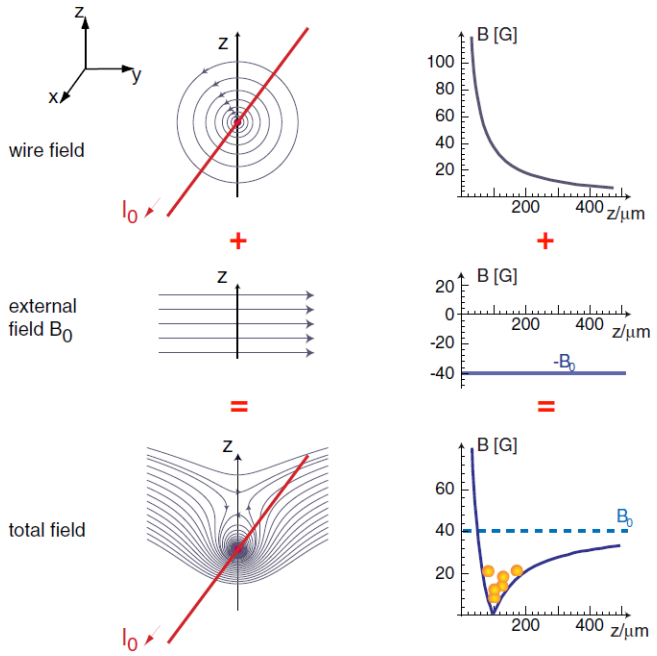

Figure 2.6: Combining the circular magnetic field from a straight wire with a constant bias produces a field which is approximately quadrupole in one dimension. By bending the wire into a U-shape we can extend this approximation to all three dimensions. Figure taken from [48].

One inevitable aspect of the U-shaped rod is that two dimensions of the field it produces will always be coupled, making it impossible to move the centre of the MOST (and hence trapped atoms) independently along one of the two axes. To overcome this, we use two pairs of external Helmholtz coils to add constant bias fields in the axes orthogonal to the original bias, allowing for a better degree of control over the position of the quadrupole zero point.

Fig. 2.7 shows a fluorescence image of the MOST we used as a source of cold atoms in our experiment. We observe the MOST using a CCD camera with a field of view of approximately 12 mm, which means that

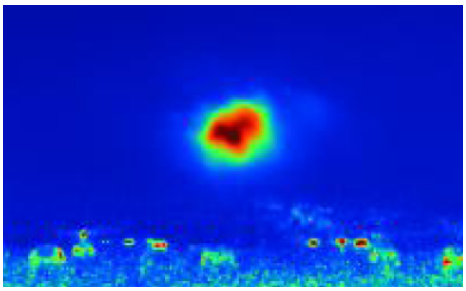

Figure 2.7: False colour fluorescence image of the MOST used in our experiment. The cloud lies ~ 1-2 mm above the surface of the mirror, and has a radius of ~ 200 μm. It contains approximately 10^7 atoms at a temperature of ~ 280 μK.

the MOST in this picture lies about 1-2 mm above the surface of the mirror. The closest the MOST can be brought to the mirror is about 0.2 mm; if it is brought any closer, the number of trapped atoms becomes negligible. In order to load cold atoms from this MOST into our optical dipole traps, the cloud is positioned ~ 500 μm above the surface of the mirror. At that distance, the cloud has a radius of ~ 120 μm, and contains approximately 10^5 atoms. Its temperature, measured by the time-of-fight (TOF) method [49], is ~ 280 μK.

3

DYNAMIC MANIPULATION OF TRAPPED ATOMS

To achieve the full control over the translational degrees of freedom of an array of trapped atoms, we require a fast and effective way of forming or rearranging multiple dipole traps. In this chapter we describe how our experiment utilises a unique spatial light modulator (SLM) which can generate arbitrary trapping potentials and change them at high speed.

3.1 RECONFIGURABLE DIPOLE TRAPS

Spatial light modulators are devices for imprinting a spatially varying amplitude or phase pattern on a beam of light. The most widely used type of SLM is the liquid-crystal display (LCD), which has the advantage of the ability to fully control both the intensity and phase of transmitted light. However, its major disadvantage is that it is slow, lacking the refresh rates required for dynamic control of trapped atoms. For

our experiment we use a Digital Mirror Device[1] (DMD) as our SLM, which consists of an array of 1024 by 768 individually addressable micro-mirrors. Each mirror is 13.7 μm by 13.7 μm in size and can be tilted by $\pm 12^{\circ}$ to create binary light patterns. The two tilts correspond to the 'on' and 'off' positions, such that if light is incident at the correct angle, the 'on' position will direct light along a chosen optical axis, and the 'off' position will reflect the light into a beam dump. The DMD has a maximum refresh rate of between 4-40 kHz, depending on how much of the array is changed. This is sufficient to allow us to display high speed movie sequences which are fast enough for dynamic control of atoms.

Fig. 3.1 shows a schematic for our experiment. Dipole trapping light from a high power laser is incident on the DMD. The surface of the DMD is imaged using a two lens microscope system onto a trapping plane within the atom cloud produced by the MOST. The MOST pre-cools the atoms and is switched off just before we load the atoms into the dipole traps. The microscope has a (de)magnification of 57:1, meaning, that given their size, individual micro-mirrors cannot be resolved. A diffraction limited spot of 1 μm corresponds to a block of 4×4 mirrors which implies that although the discrete nature of the mirrors pre-

1 Texas Instruments DMD Discovery 1100

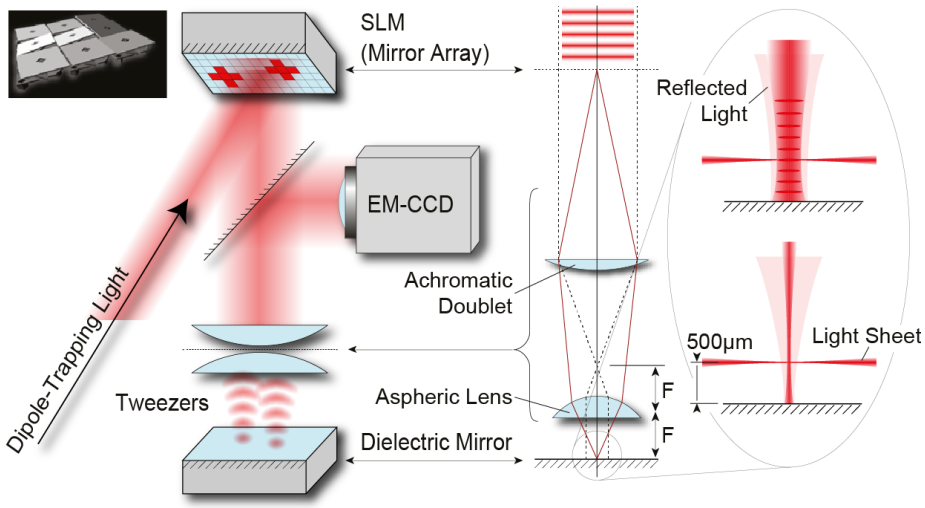

Figure 3.1: The schematic of our concept for the formation of an array of dynamic dipole traps. Trapping light is incident upon a SLM, the surface of which is imaged through a two lens microscope to form arbitrary potential landscapes which can trap and guide atoms. The incoming light is reflected back along the same optical path with a dielectric mirror placed just below the image plane of the dipole traps, creating a standing wave to aid axial confinement. A thin sheet of resonant light illuminates only the atoms trapped in the image plane, and a highly sensitive EMCCD camera is used to observe the resulting atomic fluorescence through a dichroic mirror.

vents the creation of smooth grayscale, we can mimic up to 16 levels of intensity by dithering the mirror pattern on the otherwise binary DMD.

A usual consequence of dipole traps formed by single beams is that they give tight radial confinement, but are weak along the axial direction. The microscope system we use consists of an achromatic doublet and aspheric lens (NA = 0.54, focal length = 20 mm) close to the trapped atoms, which provides the smallest possible foci for our dipole traps. This not only gives the best axial confinement, but it also allows

us to create the very small diameter ($\sim 1\,\mu m$) traps required to contain individual atoms (discussed in the next section).

Although this tight focus allows for good axial confinement for small traps, we may often wish to use larger traps, as we will see in the next chapter. To improve axial confinement for larger traps ($\gtrsim 20\,\mu m$) we include a dielectric mirror just below the focal point of the aspheric lens, which reflects the trapping light back along the same optical path. The interference between the incoming and reflected light leads to a standing wave and planes of high intensity $\lambda/2$ apart, as shown in fig. 3.2. This offers some degree of longitudinal confinement with atoms which are cold enough confined to the anti-nodal planes. The effect only partially applies for traps $\lesssim 20\,\mu m$ since the reflected beam diverges too quickly in smaller traps to offer a well defined standing wave. Early on in the experiment, we published a proposal paper presenting the basic outline and feasibility of the scheme [44]. Exact details regarding the depths and atomic confinement of the standing wave dipole traps can be found there.

To detect the trapped atoms, we illuminate them with a very thin sheet of resonant light which runs parallel to the surface of the dielectric mirror. It causes the atoms trapped in the image plane of the dipole traps to fluoresce while atoms above and below remain dark. The micro-

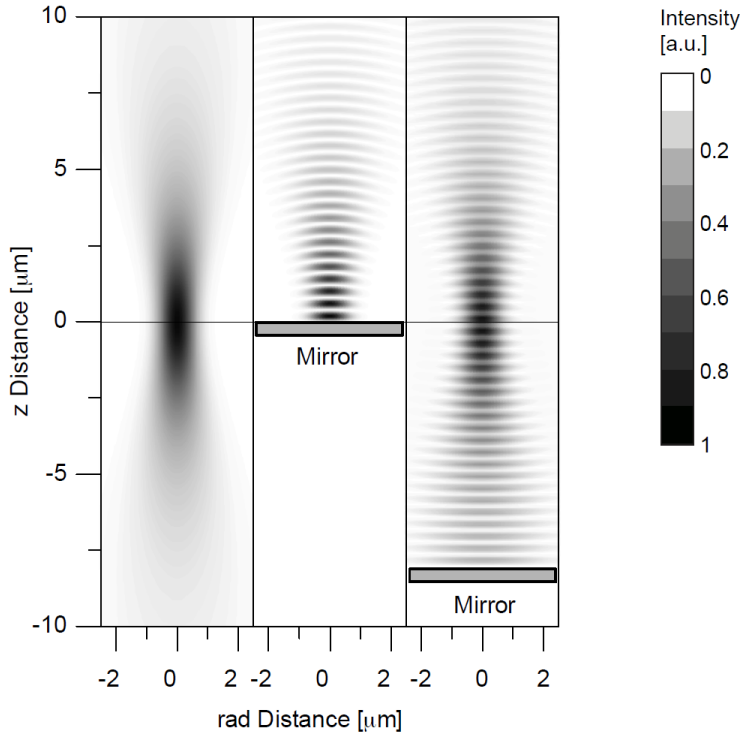

Figure 3.2: The intensity distribution of a focused beam of light (with beam waist of 0.78 μm) for different distances L between the dielectric mirror surface and the focal plane. The leftmost picture is for the case with no mirror present ($L \to \infty$), representing a pure forward travelling dipole trap beam with no axial modulation. The middle picture shows a beam which is reflected at its focal plane ($L = 0$). This trap exhibits a perfect standing wave pattern, but atoms cannot be trapped precisely at the beam waist. The picture right picture shows a retro-reflected beam whose focus lies $L = 8\,\mu m$ above the mirror surface. Here the axial intensity modulation is notably less than in the previous case, but allows us to trap atoms at the focus of the beam. Figure taken from [44].

scope setup is confocal, with the trapped atoms being detected through the same two lens system which produces the dipole traps. The florescence light is separated out from the reflected trapping light with a dichroic filter and directed into a highly sensitive electron multiplying charge-coupled device (EMCCD) camera for observation.

3.2 TRAPPING SINGLE ATOMS

Ideally, we would like our reconfigurable setup to dynamically control the motional degrees of freedom of a single cold atom, or an array of separately trapped single atoms. It is therefore essential that there exists a way to efficiently and reliably load single atoms into our dipole traps. For tightly focused dipole traps ($\lesssim 1\,\mu m$), a mechanism known as the *collisional blockade* gives rise to a significant departure from the Poissonian statistics in favour of single atom loading [50].

The effect occurs when atoms are loaded from a MOT into tightly confined dipole traps, relying on light-assisted collisions between atoms in the presence of the optical molasses. Provided that the molasses

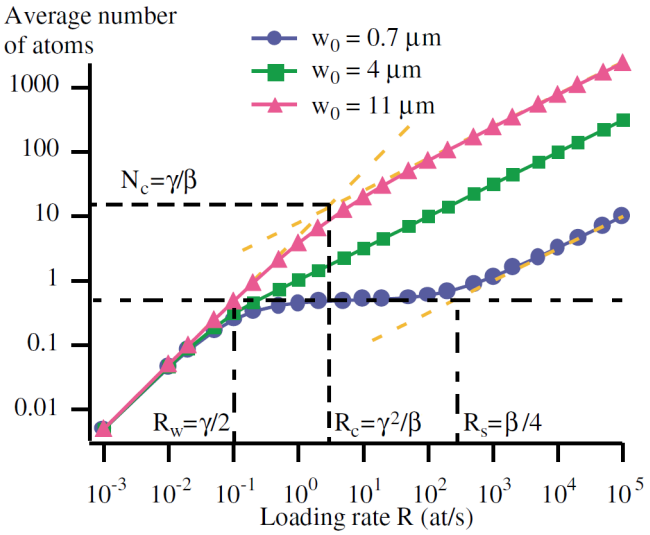

Figure 3.3: Average number of atoms in a dipole trap as a function of the loading rate R for different waist values. For $w_0 = 0.7\mu m$, the collisional blockade regime is clearly seen. Figure taken from [51].

is strong enough to saturate the transition, the rate equation for the change of atom number N within the dipole trap is given by:

$$\frac{dN}{dt} = R - \gamma N - \beta' N(N-1) \tag{3.1}$$

where R is the loading rate of the trap and γ and β' are constants. The $-\gamma N$ term represents the single body loss and $-\beta' N(N-1)$ the two-body loss. For large values of R (*strong* loading), $\langle N \rangle$ becomes large and the collisional term becomes important. The average number of atoms is then limited by the collisions, so that $\langle N \rangle = R/\beta$. The cross-over between weak and strong loading is defined by a critical atom number $N_c = \gamma/\beta$, associated with a critical loading rate $R_c = \gamma^2/\beta$, above

which the collisional term becomes dominant. The rate of two atom collisions between two atoms with identical cross sections σ trapped in a volume V is given by:

$$\beta = \frac{2\sigma v}{V} \tag{3.2}$$

where v is the velocity of the atoms.

Since β is inversely proportional to the trap volume, meaning that for sufficiently small traps, two-body decay dominates. Pairs of atoms are expelled from tiny traps ensuring that the atom number is either zero or one. The simplest way to analyse this regime is with the use of a classical Monte-Carlo simulation, with random atom arrivals, including one-body and two-body decays. This is carried out in [51] and the results are shown in fig. 3.3. All the distributions are actually sub-Poissonian, but the effect is particularly apparent in the blockade regime (0.7 µm waist example).

By using tailored optical fields to manipulate the collisions between the pairs, the reliability to load a single atom into a trap can be brought above 80 % [52]. The trapping volumes and atomic temperatures necessary to make use of the collisional blockade mechanism should be attainable in our experiment [44].

3.3 LASER SETUP

Fig. 3.4 shows the experimental setup of our schematic. This section will give a general overview of the setup depicted, focusing on the most important and relevant details. Further details of the experimental setup are written in [43] and [41]; the specifications and exact technical details of the equipment can be found in these.

The atom trapping itself is done within a sealed vacuum chamber to minimise collisions with background gas. The pressure inside the vacuum chamber is as low as 10^{-11} bar, obtained with a combination of turbo pumping under heat, titanium sublimation and an ion getter pump. A rubidium dispenser releases rubidium gas into the vacuum chamber by means of sublimation when active. Most of the optics and laser equipment used to operate the experiment sit outside the vacuum chamber; the exceptions being the aspheric lens used to focus the dipole trapping light, the dielectric mirror used to create the partial standing wave, and the U-shaped wire used to create the approximate quadrupole field for the MOST.

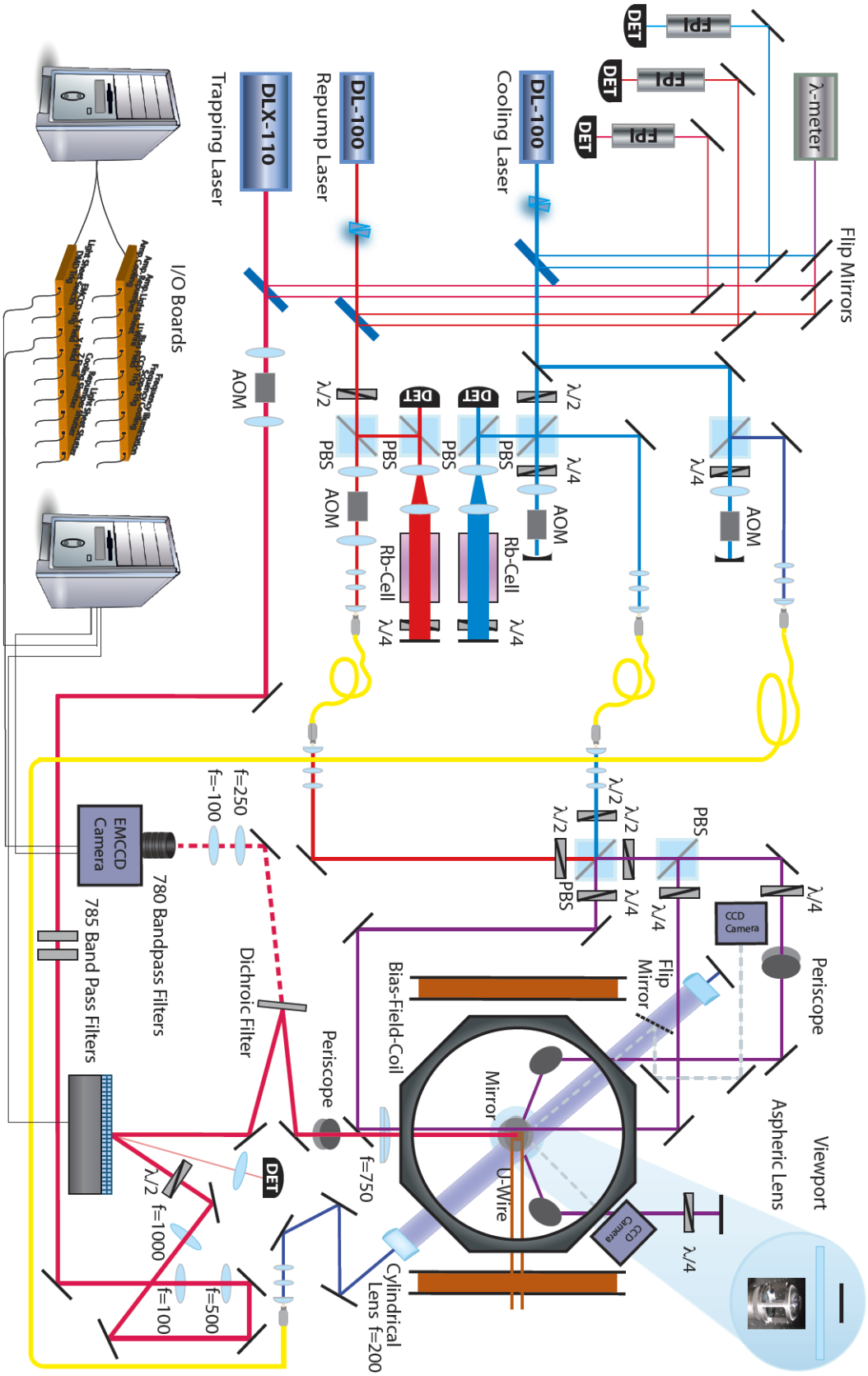

Figure 3.4: The overall experimental setup of our dynamic dipole trapping scheme. Figure taken from [41].

3.3.1 *Rubidium and the MOST*

Due to their simple electronic structure (resulting from having only one valence electron), alkali metals are often chosen for atomic cooling and trapping experiments. In our experiment we work with Rubidium and more specifically the ^{87}Rb (27.8 %) isotope. Although this isotope is less abundant than ^{85}Rb (72.2 %), it has a simpler level structure making it easier to work with. In addition, the transition frequency from ground to the first excited state is accessible with readily available near infrared semiconductor diode lasers.

The ground state of ^{87}Rb is $5^2S_{1/2}$ and the first excited state is split by spin-orbit coupling into $5^2P_{3/2}$ and $5^2P_{1/2}$. The transition from the ground state into the $|J' = \frac{1}{2}\rangle$ level is called the D1 line, and has a wavelength of 795 nm; the transition from the ground state to the $|J' = \frac{1}{2}\rangle$ level is called the D2 line, and has a wavelength of 780 nm. In our experiment we work with the latter transition.

Fig. 3.5 shows the hyperfine energy level diagram of the D2 line. The nuclear spin of $I = \frac{3}{2}$ gives a total angular momentum of $|F = 1, 2\rangle$ and $|F' = 0, 1, 2, 3\rangle$ for the ground and excited states respectively. The transition between $|F = 2\rangle$ and $|F' = 3\rangle$ is a *cycling transition*, meaning that an atom excited into the $|F' = 3\rangle$ state can only decay back to the

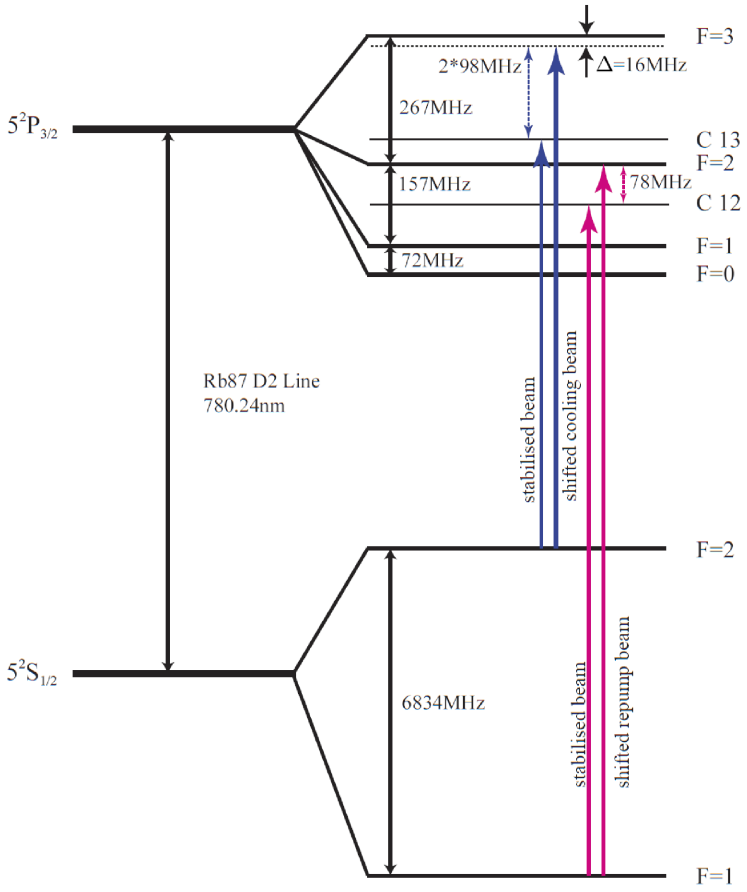

Figure 3.5: The D2 transition of ^{87}Rb. Molasses cooling occurs on the $|F = 2\rangle \rightarrow |F' = 3\rangle$ transition with a 16MHz detuning. A repump for the $|F = 1\rangle \rightarrow |F' = 2\rangle$ transition is required to return any atoms lost due to collisions or off resonance excitation back to the main cooling cycle.

$|F = 2\rangle$ in accordance with the selection rules. This forms a closed cooling transition, allowing the optical molasses to be used as a cooling technique, and a MOST to be created.

We use two lasers to operate the MOST in the lab. The first laser, which we will refer to as the *cooling laser*, is used to drive the main $|F = 2\rangle \leftrightarrow |F' = 3\rangle$ cycling transition with a detuning of 16 MHz. Off resonance excitations can occasionally leave the atom in the $|F' = 2\rangle$ state, which decays into $|F = 1\rangle$ half of the time [53]. In addition, atomic collisions can cause state flips from $|F = 2\rangle$ to $|F = 1\rangle$. Atoms in the $|F = 1\rangle$ state do not interact with the cooling laser and are quickly lost. It is therefore important we include a *repump laser* to optically pump any escaping atoms back into the $|F' = 2\rangle$ state, which will decay into $|F = 2\rangle$ half the time to rejoin the main cycling transition.

Both cooling and repump lasers are external cavity grating stabilised diode lasers[2] tuned to run at 780.24 nm. The output of the bare laser diodes are collimated and incident on a diffraction grating angled such that the first order for a specified wavelength is directed back into the diode, encouraging lasing on a mode of that wavelength. The output of the external cavity, which is the zeroth order of the grating, is a single frequency narrow-band beam. A piezo is used to fine tune the angle

2 Toptical DL100

of the grating and external cavity length, allowing for precise, wide range tunability of the output frequency. The beam emerging from the external cavity passes through an optical isolator, to prevent optical feedback into the diode.

The cooling laser is operated with an output power of 97 mW, and the repump a power of 78 mW. The beam emerges from each laser with an elliptical beam profile, so it is passed through an anamorphic prism pair, compressing its major axes and making it circular. Glass plates are used to split off small fractions of light. The reflection off the front surface is sent to a wavemeter, which provides a constant wavelength reference. The reflection off the back surface enters a Fabry-Pérot cavity, which allows us to see if the laser is running in single mode.

3.3.2 *Laser Stabilisation*

In order for the MOST to function, the frequency of the cooling and repump lasers must be very precise. The frequency of the cooling laser must be stable within a MHz, to ensure that the 16 MHz detuning remains constant throughout the experiment. Furthermore, the frequency of the lasers must not drift away from the required setting over time. The obtain this level of precision and stability, we lock the laser to a

specific spectral line of rubidium using the Pound-Drever-Hall (PDH) technique [54]. A small fraction of the laser light is siphoned off to perform Doppler free saturated absorption spectroscopy (which is explained in fig. 3.6) on a rubidium vapour reference cell. The local oscillator inside a PDH module[3] is used to generate a 20 MHz modulation of the laser light, producing *sidebands* at ± 20 MHz which are used as reference for the phase measurement of the main peak (the *carrier*). The probe beam from the spectroscopy, which consists of the two side bands along with a phase shifted carrier component, is measured using a photodiode and mixed down with the local oscillator signal. The resulting electronic readout gives a measure of how far the carrier is off resonance, with the sign of the signal indicating whether it is above or below resonance. This error signal is then input into a proportional-integral-derivative (PID) negative feedback module[4] which adjusts the feedback grating and current supply of the laser in such a way as to drive the error signal to zero (whereby the laser will be on resonance). This technique gives long term laser stabilisation to a bandwidth of roughly 100kHz.

The cooling laser is locked onto the $C1 - 3$ crossover line and sent through an acousto-optic modulator (AOM) set at 98MHz. The AOM

3 Toptica PDH 110
4 Toptica PID 110

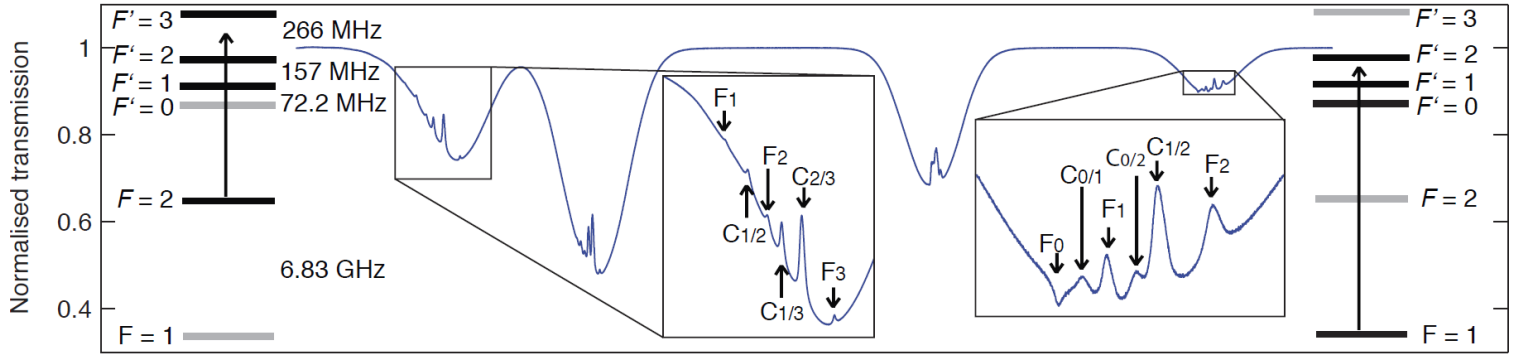

Figure 3.6: At room temperature, Doppler broadening is usually the dominant contribution to the linewidth in atomic spectra of gases. Saturated absorption spectroscopy uses a strong optical pump beam to saturate a group of atoms with a particular velocity. A probe beam of the same frequency propagates in the opposite direction, so interacts with the group of atoms of the same speed travelling in the opposite direction. The frequency is scanned and when the two beams interact with the same group of atoms (those with little speed along the beam axis), a narrow peak is observed in the absorption spectrum. This technique can be used to achieve much higher resolutions of atomic energy levels. A consequence of the technique is the creation of spectral lines halfway between two atomic energy levels, called crossover lines. This arises when the pump beam saturates the atoms in a velocity group via one atomic transition, and the probe beam interacts with the same group of atoms via a second transition of different frequency. This figure shows the full absorption spectrum for the D2 line of rubidium. The two middle peaks are for ^{85}Rb and the outer two for ^{87}Rb.

uses a piezo to generate sound waves within a crystal to diffract and frequency shift incoming light. The beam is sent through in a dual pass configuration, whereby the first order of the passing light is retro-reflected back into the AOM and frequency shifted again. This shifts the light 196MHz to the $|F = 2\rangle \leftrightarrow |F' = 3\rangle$ Doppler cooling transition, leaving a detuning of 16 MHz, as show in fig. 3.5. The repump laser is locked onto the $C1 - 2$ crossover line and is shifted 78 MHz to the $|F = 1\rangle \leftrightarrow |F' = 2\rangle$ transition using an AOM in a single pass configuration.

After the beams pass through the AOMs, they are coupled into single mode polarisation maintaining fibres. These fibres provide stability against beam pointing shifts and outputs a clean Gaussian beam profile. Finally, the cooling and repump lasers are are combined using a polarising beam splitter cube. The combined beam is subsequently split into the requisite MOST beams, with $\lambda/4$ waveplates being used to ensure each beam has the correct helicity. Each MOST beam has a power of approximately 8 mW, equivalent to an intensity of $10 I_{sat}$ for rubidium.

3.3.3 *The Light Sheet*

The light sheet, used to illuminate the dipole trapped atoms in the image plane, is created by siphoning small amount of light from the

cooling laser after stabilisation on the $C1-3$ crossover line. The beam passes through an AOM in the double pass configuration, shifting the frequency by 214 MHz and allowing it to run slightly above the $|F = 2\rangle \leftrightarrow |F' = 3\rangle$ transition. The 2 MHz blue detuning is to account for the slight a.c. Stark shift experienced by the atoms while inside a dipole trap.

The sheet is produced by focusing the beam down using a cylindrical lens to a thickness of 9.7 μm with a Rayleigh length of 100 μm. It is retro-reflected to balance any scattering force exerted and avoid pushing atoms out of the trap. The total power within the light sheet is 7 μW, which gives rise to a scattering rate of 16 photons/μs.

3.3.4 *Dipole Trapping Light*

The DMD is illuminated using a high power tapered amplified laser diode[5] with a maximum output power of 800 mW. It is operated at $\lambda = 785$ nm, meaning it is red-detuned by 5 nm from the D2 line in ^{87}Rb. This relatively small detuning is chosen to achieve a reasonable trap depth at light intensities below the damage threshold of the DMD ($5\,W/mm^2$). After taking into account various optical loses (e.g. bad

5 Toptical DLX110

beam profile, loss on mirrors, loss going through various filters and the vacuum chamber window), and the optical magnification of 57, this results in an intensity of approximately $30\,W/mm^2$ in the focal plane of the imaging system. This corresponds to a maximum potential depth of $U_0 = k_B \cdot 100\,\mu K$.

4

ARBITARY TRAPPING AND CONTROLLED TRANSPORT

In this chapter we demonstrate the versatility and potential scalability of our scheme. We investigate how the DMD can be used to confine and transport atoms in separate traps by creating arbitrarily shaped and easily reconfigurable potential landscapes. The results of our experiment were published in [42]; the following sections from the paper are adapted to better fit this thesis.

4.1 ATOMS TRAPPED IN ARBITRARY POTENTIALS

The view observed by the EMCCD, through the top of the microscope, is well-suited for arbitrarily manipulating and observing atoms in a two-dimensional plane. However, atoms are in general trapped in a vertical column perpendicular to the image plane. Obviously, atoms get transferred into the standing-wave dipole trapping beams at various

heights above the mirror, so that observing all atoms by fluorescence imaging through the microscope would normally give rise to blurry pictures. As we are primarily interested only in those atoms trapped in or near to the image plane, we resolved that issue using the light sheet mentioned in previous chapters to isolate fluorescence to the image plane of the EMCCD and avoid excitation of atoms being out-of-focus. Independent optical characterisation of our imaging system (detailed in [41]) shows that the it has a resolution of $1 \pm 0.2\,\mu m$, which also limits the edge sharpness of any trapping potential.

We can control the light pattern in the image plane of the traps by changing the configuration of the micro-mirrors on on the DMD. The fluorescence images taken through the microscope reveal that the shape of dipole trapped atom clouds adapt to fit the imposed trapping geometry. Fig. 4.1 shows atoms confined to a series of circular flat-bottom traps. The traps are created by displaying disks of different radii on the homogeneously illuminated DMD. Normally, one would expect the atoms to fill the trap, such that the radius of the atom cloud equals the trap radius. This is indeed found for traps of large size, which demonstrates that the atoms adapt to the imposed trapping geometries. Deviations are only found for very small traps, where some atoms trapped away from the image plane appear out of focus.

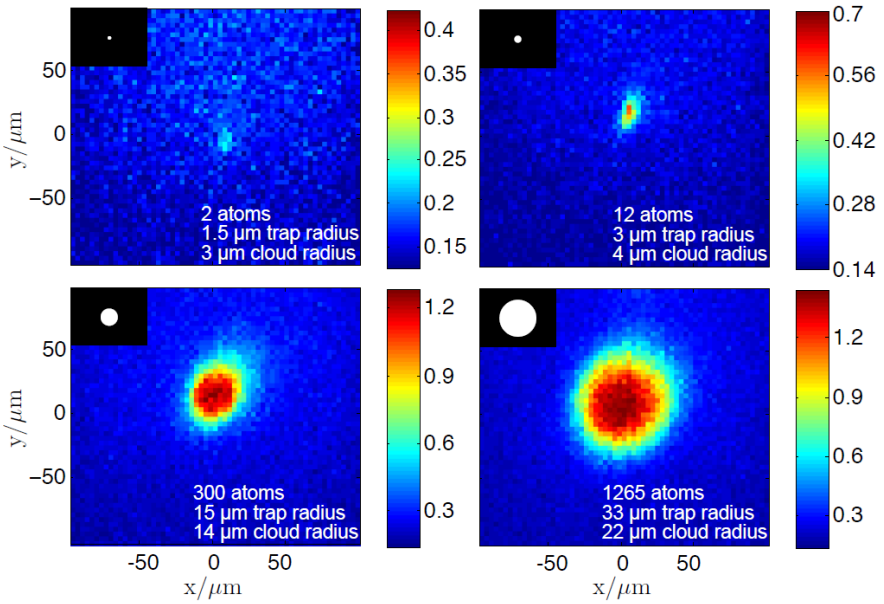

Figure 4.1: 200 µm × 200 µm EMCCD captured fluorescence images of atoms trapped in single static round traps of different sizes. Each image is an average over 20 consecutive trap loading cycles. The colour scale has units of atoms per μm^2. The actual patterns on the DMD used to produce the traps are shown in top left of the respective insets using the same length scale.

The approximate atom number in each trap was deduced from fluorescence images averaged over 20 loading cycles. During each cycle, the light sheet is flashed on for 90 µs, within which a single atom emits ~1400 photons. Of these, 21 photons are detected, corresponding to an overall photon detection efficiency of $\eta_{tot} = 1.5 \pm 0.2\,\%$. This is the product of the collection efficiency of the lens system $\eta_{lens} = 7.6\,\%$, the losses along the optical path $\eta_{loss} = 51\,\%$, and the quantum efficiency of the camera $\eta_{QE} = 41\,\%$. We found that the largest trap (Ø 65 µm) contained 1270 ± 170 atoms, the large trap (Ø 30 µm) contained 300 ± 40 atoms, the medium trap (Ø 6 µm) 12 ± 2 atoms, and the smallest ob-

served trap (Ø 3 μm) 2.0 ± 0.3 atoms. This is very close to the single-atom regime, which one might reach by application of the collisional blockade technique described in Chapter 3. Presumably this effect limits the atom number to one in the smallest possible traps (1.0 μm waist) in our setup. However, we were not able to discriminate individual atoms from the background light that is scattered of the dielectric mirror behind the trap.

The lifetime of atoms in all traps is approximately 50 ms, and does not change significantly with the size of the trap. Primarily, it is restricted by the diffusion of atoms along the trapping beam, which leads to a decrease in atom density at the site of the light sheet. Most other losses, e.g. losses due to background gas collisions or scattering of trapping light, would represent much longer lifetimes (estimates are given in [44]). For all traps of radius $\geqslant 3$ μm, the atom number was sufficiently large for TOF measurements, which yield a consistent temperature of 90 ± 10 μK. This is on the same scale as the calculated trap depth.

We furthermore verified the versatility of the DMD by trapping atoms in arbitrary shaped potentials. The trap arrays shown in fig. 4.2 underline the scalability of the scheme: such arrays could be used to implement a large register of atomic qubits. In the first two images, the radius of each individual trap is 3 μm, and the average atom number in each is

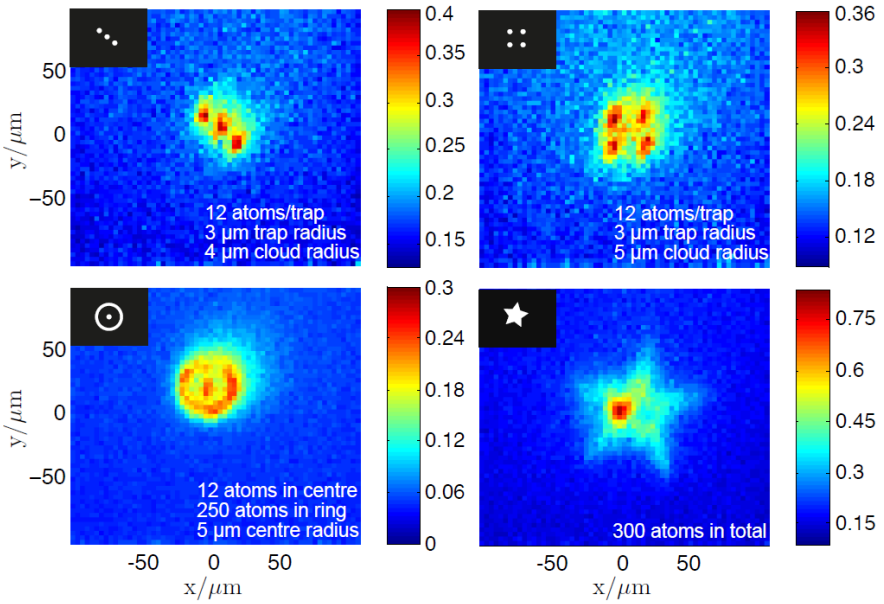

Figure 4.2: 200 µm × 200 µm EMCCD captured fluorescence images of atoms trapped in various arbitrary trapping geometries. Each image is an average over 20 consecutive trap loading cycles. The colour scale has units of atoms per µm^2. The actual patterns on the DMD used to produce the traps are shown in top left of the respective insets using the same length scale. The halo seen in the first three fluorescence images can be attributed to diffusion of atoms in the light sheet.

12 ± 2. The third image shows atoms trapped in a bullseye-shaped trap. The Ø 6 µm centre of the bullseye contains 12 ± 2 atoms, whilst the ring contains 250 ± 33 atoms. This ring structure shows that it should be possible to transport atoms not just along straight paths, but also along curved trajectories.

The last image in fig. 4.2 shows 300 ± 40 atoms in a star-shaped trap which is affected by an inhomogeneity in the trapping light. The intensity variation of the laser over the whole area of the DMD is about 30 %. This has no significant impact on smaller traps. However, in larger flat

bottomed traps like the star, it leads to a congregation of atoms in the regions of highest intensity. Notwithstanding, the large variety of different shapes highlights the flexibility of trap generation with the DMD. Trapped atoms can be arranged into arbitrary patterns using the DMD to impose any desired shape of the trapping potential.

For the larger traps depicted in fig. 4.1 and fig. 4.2, the atom number stated is always restricted to those atoms exposed to the light sheet due to diffusion of the hottest atoms out of the trap. For trap radii $\leqslant 3\,\mu m$, confinement along the vertical is dominated by the waist of the trapping beam, so the atom number measured equals the real atom number in the trap. The density of atoms and the small size of the traps leads to a maximum reduction of the fluorescence of 1 % due to re-absorption, and hence does not lead to an underestimation of the observed atom number.

4.2 CONTROLLED TRANSPORT OF ATOMS

So far, we have shown that atoms can be held in a variety of arbitrarily shaped traps. This includes regular arrays of atoms, which one could use as quantum registers in a scalable quantum processor. However, to fill such an array with preferentially one atom per site, or to arbitrarily

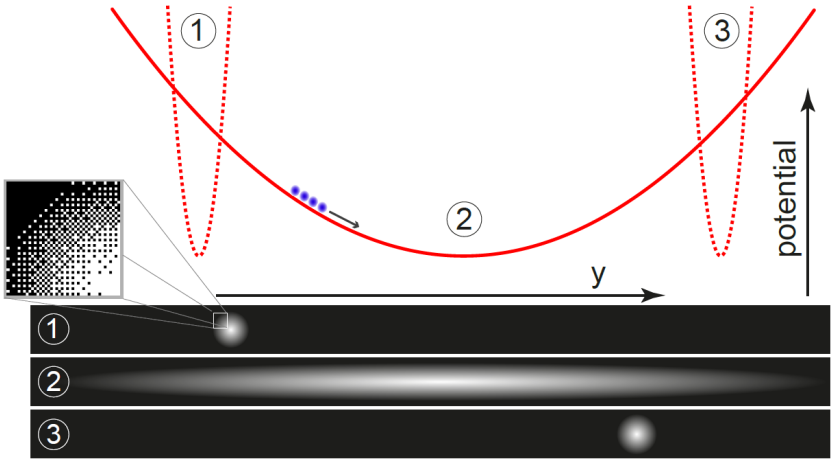

Figure 4.3: Illustration of the concept of the atom transport via ballistic 'release and recapture' (not to scale). The atoms are first confined in trap (1), then move along the harmonic transport trap (2) and refocus at the destination when the end trap (3) is switched on. The close-up view shows the dithering of the mirror pattern we apply to obtain a smooth trapping potential.

access a random cell within a register, it is necessary to move atoms independently from one trapping site into another. Here, we show how to accomplish this task and deterministically transport atoms between two well defined positions. The most intuitive way for doing so would be to move the trap of interest by gradually changing the image on the DMD such that the centre of the trap gets displaced. However, this approach is hampered by the discrete switching of the DMD's mirrors, which results in the trap hopping along its trajectory rather than in a smooth motion. In turn, the atoms are lost due to excess heating.

Our solution therefore is to let the atoms swing along a harmonic potential before recapturing them in the outer turning point. This ballistic 'release and recapture' transport effectively entails opening an elon-

gated harmonic trapping channel between a start and end position, and timing the recapture to coincide with half the oscillation period of the atoms in this potential well. Fig. 4.3 illustrates this procedure and also shows the dithered mirror pattern used to obtain a smooth trapping potential in the image plane. The transport is accomplished in two steps: First, we switch the image on the DMD from the initial harmonic trap (1) to the elongated transport trap (2). Second, after half a period of oscillation, we switch the image on the DMD to the final trap (3). At this very moment, all atoms normally regroup at the destination, regardless of their initial temperature, provided the transport trap is purely harmonic. As the DMD is a mechanical device, 'switching' between images consists of changing the tilt angle of the micro-mirrors. The switching takes a minimum of 50 µs and cannot be altered. This is slow on the time scale of the transverse trapping frequency of $2\pi \times 18\,\mathrm{kHz}$ of the initial and final traps (of 6 µm waist), but sudden if compared to the $2\pi \times 1\,\mathrm{kHz}$ oscillation frequency in the transport trap.

In general, one has to take into account that the atoms move in three dimensions. The DMD controls the potential in the trapping plane, while the confinement perpendicular to it is controlled by a combination of the near-field propagation and standing-wave effects resulting from the interference between the trapping light and its own reflection.

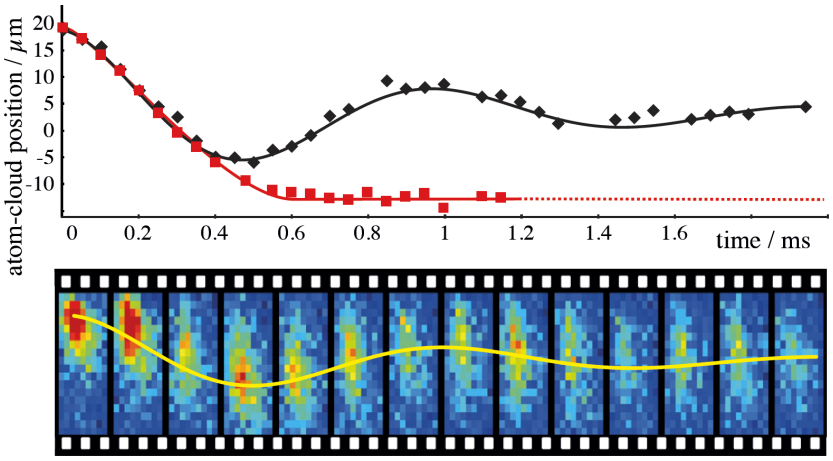

Figure 4.4: Ballistic transport of atoms in a single trap. The harmonic transport traps, $U \propto -(1-(x/w_x)^2-(y/w_y)^2)$, are $w_x = 6\,\mu m$ wide and $w_y = 26\,\mu m$ wide, whilst the round harmonic start and end traps all have a waist of $w_r = 6\,\mu m$. Free Oscillation (black trace), and recapture (red trace) of atoms. The filmstrip below shows a sequence of fluorescence images taken at various instants of the transport.

We calculated the near-field intensity distribution away from the image plane using the Fresnel-Kirchhoff diffraction integral. The divergence is moderate enough to yield a standing-wave modulation visibility of 75 % at the height of the image. This is very strong, and most atoms are confined to the resulting anti-nodal planes. Therefore, we effectively have 20 identical two-dimensional trapping planes within the width of the light sheet. This subdivision into various trapping planes only holds during transport, and does not affect the initial and final traps which have Rayleigh lengths that are much shorter than the trap to mirror distance.

Fig. 4.4 shows atoms oscillating along the transport channel (black trace) and illustrates that we are capable of recapturing them at the turning point after half a period of oscillation (red trace). The displayed atom-cloud position is the centre-of-mass of the recorded fluorescence images, which were taken at constant rate. Of the 22 atoms initially in the trap, 12 atoms are recaptured. Most surprisingly, this cannot be attributed to heating-induced losses, as time-of-flight measurements reveal a temperature rise of only 10 μK. Instead, the reduction in fluorescence is to some extent explained by atoms not exactly regrouping at the destination. The primary reason for that limitation is the small anharmonicity of the transport trap, resulting in a 1.3 ms damping time of the harmonic motion (see fig. 4.4, black trace). The secondary loss mechanism is a diffusion of the most energetic atoms along the standing wave, i.e. away from the image plane. Both losses could be easily reduced using either a more intense trapping beam (i.e. at higher laser power or with different magnification not to exceed the damage threshold of the DMD), or a more sophisticated cooling method to start with much colder atoms that are less sensitive to anharmonicities of the transport trap. Hence disregarding the spreading, the successful ballistic transport in harmonic traps illustrates that the DMD is an ideal tool for positioning atoms in a deterministic way.

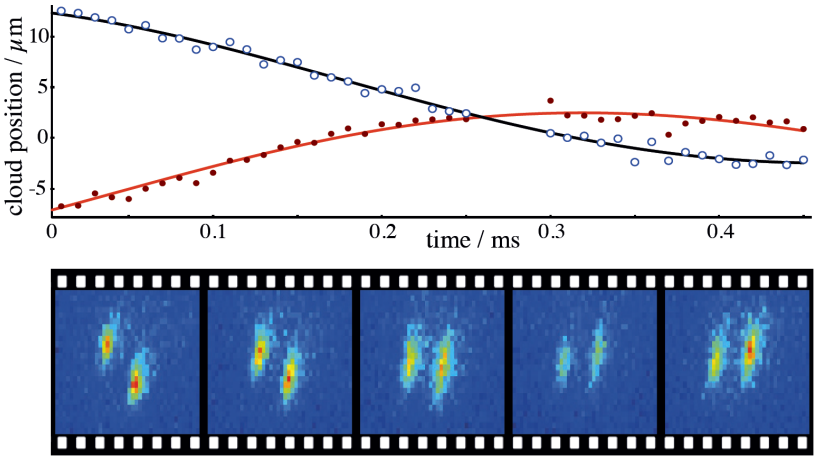

Figure 4.5: Double trap transport. The harmonic transport traps, $U \propto -(1 - (x/w_x)^2 - (y/w_y)^2)$, are $w_x = 6\,\mu m$ wide and $w_y = 26\,\mu m$ wide, whilst the round harmonic start traps has a waist of $w_r = 6\,\mu m$. The traps are filled with 10-15 atoms oscillating past each other in two separate harmonic wells. The shown fit curves model a damped harmonic motion.

The manipulation of individual information carriers in a large-scale quantum network relies on the capability of re-arranging atoms sitting at different nodes of an array independently from each other. To demonstrate that this can be done, we use two transport channels to move atoms in opposite directions from two different starting positions. We apply the same release and recapture method as discussed above. Fig. 4.5 shows atoms oscillating past each other in these harmonic potentials. The atoms move to destinations 8 μm and 9 μm away from their respective starting points, with the two destinations chosen independently. This individual transport of randomly selected trapping sites shows that DMD-controlled atom traps have the potential of re-grouping arrays of trapped atoms to any arbitrary pattern. Hence, the

random access of arbitrary registers, which is essential in any computer (whether classical or quantum), could be achieved with DMD-based optical dipole traps.

4.3 LIMITATIONS OF THE SYSTEM

As mentioned in the introduction, the two most promising candidates for including a cavity into this experiment were and fibre-tip cavities and cavities in photonic band-gap crystals. For latter, the idea was to embed the cavities directly into the dielectric mirror used to retro-reflect the dipole trapping light. However we were never able to trap atoms sufficiently close to the mirror surface for this to become a viable option, and this design was abandoned. Although coupling dipole trapped atoms to photonic band-gap cavities has been achieved recently [55], we did not believe it was possible with the equipment we had available at the time and in our particular scheme. So the rest of this thesis is devoted to the analysis of fibre-tip cavities, with a view to allowing atoms to be manoeuvred into the mode with our DMD dipole traps.

There also turned out to be some technical difficulties associated with the inclusion of the dielectric mirror. The enforced use of a MOST proved problematic. The molasses beams had to be reflected at an angle

off the surface of the mirror, making the system hard to align. Changes in current in the U-shaped wire or bias field, used to create the approximate quadrupole field, changed the shape and position of the MOST cloud in non trivial ways, making fine control of the cloud and loading of atoms into the dipole traps difficult. Finally, scattered light from the dielectric mirror made detecting single atoms in the dipole traps challenging. Chapter 6 explores the removal of the dielectric mirror in favour of a free space MOT, and how this would be compatible with the inclusion of fibre-tip cavities.

Part II

FIBRE-TIP MICRO-CAVITIES

5

CAVITY QUANTUM ELECTRODYNAMICS

Before we being to explore the intricacies of fibre-tip cavities, we first take a detailed look at some of the theory behind cavity QED. In this chapter we investigate the formation of optical cavities, their key principles of operation and why they are so popular in light-matter interaction experiments.

5.1 OPTICAL RESONATORS

An optical cavity (or optical resonator) is an arrangement of mirrors whose geometry allows for light waves of a certain frequency to form a standing wave within them. The reflectivity of these mirrors is often chosen so that the light oscillates close to a million times within the cavity before escaping. Optical cavities are a key component of lasers, allowing light to pass through the same piece of gain medium many times, providing much greater amplification in a small region of space.

They can also be used to magnify the interaction strength between an atom and radiation oscillating within the cavity, since the light is reflected through the atom numerous times.

The simplest cavity model, the parallel plane or Fabry-Pérot cavity, consists of two opposing flat mirrors separated by a distance L. Each mirror is characterized by an amplitude reflectivity coefficient r and an amplitude transmission coefficient t. In practice, there will also be an amplitude loss coefficient l associated with each mirror. From energy conservation the coefficients are connected by:

$$r^2 + t^2 + l^2 = 1$$

Ignoring losses for now, consider a plane electromagnetic wave E_{in} which enters a Fabry-Pérot cavity from the left hand side. Part of the incoming field $t_1 E_{in}$ is transmitted through the first mirror and the rest is reflected. This light travels to the second mirror, acquiring a propagation phase shift of $e^{-i\phi}$ along the way. At the second mirror the field is again partially transmitted ($E_{tr1} = t_1 t_2 E_{in} e^{-i\phi}$) and partially reflected ($t_1 r_2 E_{in} e^{-i\phi}$). As shown in fig. 5.1 , the light continues bouncing back

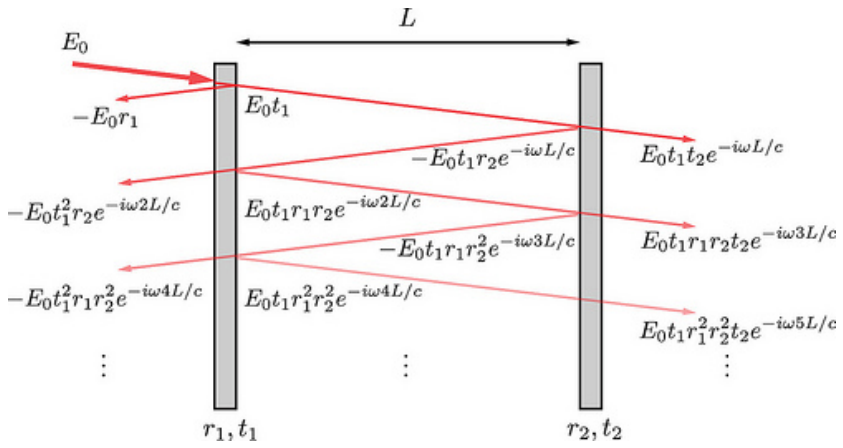

Figure 5.1: A Fabry-Pérot cavity setup. Light entering the cavity is reflected multiple times at each of the mirrors.

and forth in such a manner. The transmitted components interfere with each other, summing up to form a geometric sequence:

$$\begin{aligned} E_{tr} &= E_{tr1} + E_{tr2} + \dots \\ &= E_{in} t_1 t_2 \sum_{k=0}^{\infty} E_{in} r_1^k r_2^k e^{-i(2k+1)\phi} \\ &= E_{in} t_1 t_2 e^{-i\phi} \frac{1}{1 - r_1 r_2 e^{-2i\phi}} \end{aligned} \tag{5.1}$$

The transmitted intensity is given by the square of the field:

$$\frac{I_{tr}}{I_{in}} = \left|\frac{E_{tr}}{E_{in}}\right|^2 = \underbrace{\frac{t_1^2 t_2^2}{(1 - r_1 r_2)^2}}_{\text{Maximum Transmission, } T_{max}} \frac{1}{1 + \frac{4 r_1 r_2}{(1 - r_1 r_2)^2} \sin^2 \frac{\omega L}{c}} \tag{5.2}$$

where the single trip phase in free space is simply $\phi = kL = \omega L/c$ in this setup.

From this expression, we can see that the cavity exhibits strong resonance every time the cavity length is a multiple of $\lambda/2$, which corresponds to when the round-trip phase shift $2\omega L/c$ is a multiple of 2π:

$$\frac{2\omega_n L}{c} = n \cdot 2\pi \tag{5.3}$$

where n is a positive integer. This is represented by a series of peaks in the transmission spectrum as shown in fig. 5.2. The frequency interval between successive transmission peaks is a useful construct for cavity analysis and description, and is known as the *free spectral range* (FSR):

$$\Delta\omega_{FSR} = \omega_{n+1} - \omega_n = 2\pi\frac{c}{2L} \tag{5.4}$$

From eqn. 5.1 we can also work out the *linewidth* or *full-width half-maximum* (FWHM) of each transmission peak, defined as the entire width of the peak at half the maximum transmission intensity:

$$\frac{I_{tr}}{I_{in}} = \frac{T_{max}}{2} \implies \frac{1}{1+\frac{4r_1r_2}{(1-r_1r_2)^2}\sin^2\frac{\omega L}{c}} = 1$$

$$\frac{2\sqrt{r_1r_2}}{1-r_1r_2}\frac{\omega L}{c} \simeq \pm 1$$

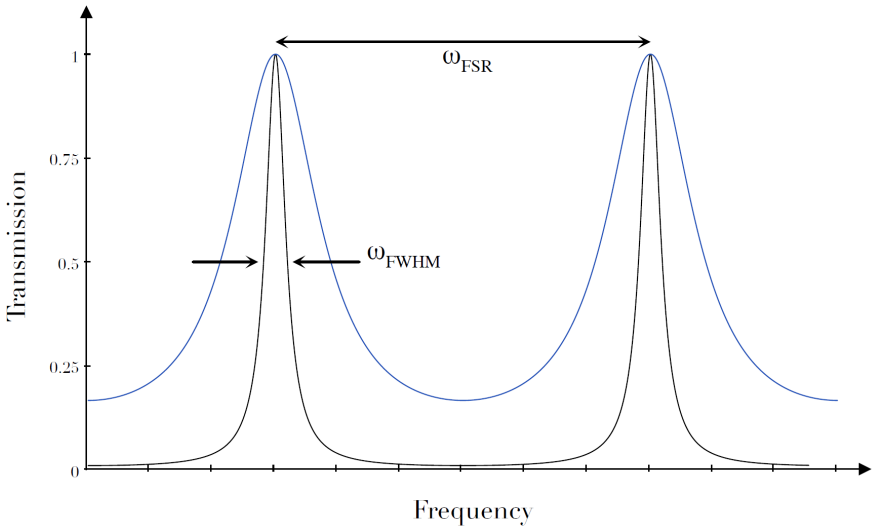

Figure 5.2: Transmission spectrum of a cavity. The finesse is defined as the ratio of the cavity linewidth (ω_{FWHM}) and mode separation (ω_{FSR}). As the finesse increases from $\mathcal{F} = 2$ (in blue) to $\mathcal{F} = 10$ (in black) the individual peaks can be more easily resolved. Figure taken from [56].

so:

$$\Delta\omega_{FWHM} = \frac{1 - r_1 r_2}{\pi\sqrt{r_1 r_2}} 2\pi \frac{c}{2L} \tag{5.5}$$

The ratio:

$$\mathcal{F} = \frac{\Delta\omega_{FSR}}{\Delta\omega_{FWHM}} = \frac{\pi\sqrt{r_1 r_2}}{1 - r_1 r_2} \tag{5.6}$$

is known as the *finesse* of the cavity and is dependent only on the reflectivity of the mirrors. It can be understood as the average number of times a photon is reflected back and forth within a cavity until it is finally transmitted through one of the mirrors.

The field inside the cavity forms a standing wave. At an anti-node all forward and reverse reflections interfere constructively and give an overall resonant intra-cavity field strength:

$$E_{cavity} = E_{in} t_1 (1 + r_2)(1 + r_1 r_2 + r_1^2 r_2^2 + ...) = E_{in} \frac{t_1 (1 + r_2)}{1 - r_1 r_2} \quad (5.7)$$

For the example of two identical high reflectively lossless mirrors ($r_1 = r_2 = r \approx 1$ and $t^2 = 1 - r^2$):

$$E_{cavity} \approx E_{in} \frac{2}{\sqrt{(1 - r^2)}} \quad (5.8)$$

Which gives an intra-cavity intensity at an anti-node of:

$$I_{cavity} \approx I_{in} \frac{4}{1 - r^2} = 4 \frac{\mathcal{F}}{\pi} I_{in} \quad (5.9)$$

This shows that the cavity enhances the intensity of incident radiation by a factor of $4\mathcal{F}/\pi$. This is the main reason why cavities are used in atom-photon interaction experiments, and why higher finesses are usually desirable. If the atom is not localised to an anti-node along

the resonator axis, it will experience an average intensity over one or several periods of the standing wave:

$$I_{cavity}^{mean} = 2\frac{\mathcal{F}}{\pi} I_{in} \tag{5.10}$$

This assumes that the atom is only non-localised in one dimension (along the main cavity axis). To understand the full interaction between the atom and cavity, we must examine a three dimensional treatment of the cavity.

5.2 TRANSVERSE MODES

For nearly all optical cavities of interest, the total propagation of the light through one round trip in an optical resonator can be described by a propagation integral of the general form:

$$E^{(1)}(x, y) = e^{-2i\phi} \iint K(x, y, x_0, y_0) E^{(0)}(x_0, y_0) dx_0 dy_0 \tag{5.11}$$

where the integral is over the transverse coordinates at an arbitrary reference or input plane. The function K is commonly called the propagation kernel, since the field $E_{n+1}(x, y)$ after one propagation step can be obtained from the initial field $E_n(x_n, y_n)$ through the operation of

the linear propagator $K(x, y, x_0, y_0)$. The exact form of the kernel K will depend on the reference plane chosen.

Usually during resonator analysis we separate out the propagation kernel from the on-axis phase shift term $e^{-i\phi}$. We discussed the on-axis phase shift previously and it represents the longitudinal modes of the cavity, leaving all the necessary information for evaluation of transverse field patterns in the remaining kernel $K(x, y, x_0, y_0)$.

Given that K is linear, we may then ask whether there exists a set of eigenmodes E_{nm} such that:

$$E^{(1)}_{nm}(x, y) = \int\int K(x, y, x_0, y_0) E^{(0)}_{nm} = \gamma_{nm} E^{(0)}_{nm}(x, y) \tag{5.12}$$

with γ_{nm} being the corresponding set of eigenvalues. If eigensolutions that satisfy eqn. 5.12 do exist, then these eigensolutions represent the self-reproducing transverse eigenmodes which exist in a stable optical cavity.

It is in general not possible to prove these transverse eigenmodes form a complete set. However, the Hermite-Gaussian or Laguerre-Gaussian (for exactly cylindrically symmetric geometries) functions closely approximate the eigenmodes in ideal optical resonators, and do form a complete basis set.

5.2.1 *Hermite Gaussian Modes*

Real resonators are typically built with spherically concave mirrors, allowing the beam to be continuously refocused and thus mitigating any diffraction losses due to the finite size of the mirrors. The propagation of the electromagnetic field is described by the Maxwell equations with the mirrors as boundary conditions. For fields propagating along one direction, the z-axis, the eigenmodes can be described in the paraxial approximation by standing wave Hermite-Gaussian modes [57]:

$$E_{nm}(x, y, z, t) = u_n(x, z)v_m(y, z)e^{i(\omega t - kz)} \tag{5.13}$$

As a function of the x and z coordinates, the solution of the wave equation has the form:

$$u_n(x, z) = \frac{1}{\sqrt{w(z)}} H_n\left(\sqrt{2}\frac{x}{w(z)}\right) \exp\left(-\frac{x^2}{w^2(z)} - i\frac{kx^2}{2R(z)} + i\frac{2n+1}{2}\Psi(z)\right) \tag{5.14}$$

where:

- H_n is the Hermite polynomial of the n^{th} order,

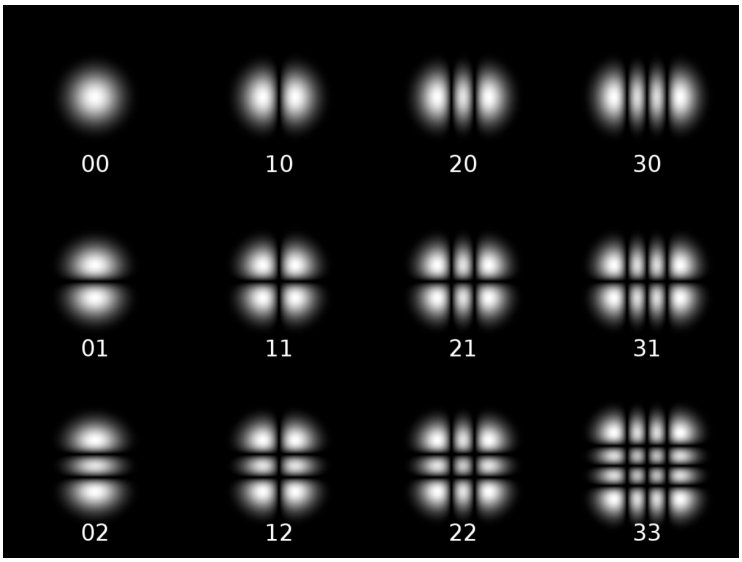

Figure 5.3: The first twelve Hermite-Gaussian modes.

- $w(z)$ is the beam radius at which the field amplitude and intensity drop to $1/e$ and $1/e^2$ of their axial values respectively,

- $R(z)$ is the radius of curvature of the beam's wavefronts, and

- $\Psi(z) = \arctan(z/z_R)$ is the Guoy phase.

The expression in the y direction $v_m(y,z)$ can be written analogously.

These modes are know as the *Transverse Electromagnetic* modes and typically abbreviated to TEM_{nm}. The first few are shown in fig. 5.3. The lowest order mode, TEM_{00} or *fundamental* mode, is usually the most prevalent within an optical cavity:

$$\begin{aligned} E_{00}(x,y,z,t) = & E_0 \frac{w_0}{w(z)} \exp\left(\frac{x^2+y^2}{w^2(z)}\right) \\ & \times \exp\left(-ikz + i\omega t - i\frac{k(x^2+y^2)}{2R(z)} + i\Psi(z)\right) \end{aligned} \tag{5.15}$$

5.2.2 *Gaussian Beam Parameters*

A Gaussian beam is a beam of electromagnetic radiation whose transverse field and intensity profiles are well approximated by Gaussian functions. Many lasers emit beams that approximate a Gaussian profile since they usually operate on the TEM_{00} mode of their optical resonator. The mathematical form of a Gaussian beam is the same as that of the TEM_{00} mode.

The geometry and behaviour of a Gaussian beam is governed by the set of beam parameters described in fig. 5.4. The spot size (radius) of a Gaussian beam will be at its minimum value at one place along the beam axis, namely at the focus. This radius is known as the *beam waist* w_0. For a beam of wavelength λ the variation of the spot size as a function of distance along the optical axis is given by:

$$w(z) = w_0 \sqrt{1 + \left(\frac{z}{z_R}\right)^2} \tag{5.16}$$

where the origin of the z-axis is defined to coincide with the beam waist, and where $z_R = \frac{\pi \omega_0^2}{\lambda}$ is what is known as the *Rayleigh length*. This is defined such that at a distance from the waist equal to z_R, the width of the beam is $w(\pm z_R) = \sqrt{2} w_0$. The distance between then these two

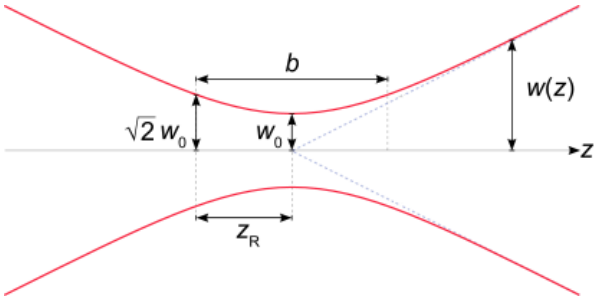

Figure 5.4: Parameters used to describe a Gaussian beam. The red line outlines where the beam intensity has fallen to $1/e^2$ times its maximum value. Subsequently w_0 is defined to be the waist of the beam, $w(z)$ the size of the beam at some axial distance z from the focus, z_R the Rayleigh length and b the confocal length. Figure from [58].

points $b = 2z_R = \frac{2\pi w_0^2}{\lambda}$ is known as the *confocal parameter* or *depth of focus* of the beam.

As we move further away from the waist, the radius of curvature (R) of the wave front also changes:

$$R(z) = z\left[1 + \left(\frac{z_R}{z}\right)^2\right] \tag{5.17}$$

This shows that to fit such a Gaussian inside a symmetric cavity, its waist is uniquely defined by the radius of curvature of the mirrors used, and the distance of these mirrors from the centre:

$$w_0^2 = \frac{\lambda}{\pi}\sqrt{R(z)z - z^2} \tag{5.18}$$

5.2.3 *High Order Modes*

The overall phase for the electromagnetic wave is:

$$-kz - \frac{k(x^2+y^2)}{2R(z)} + (n+m+1)\Psi(z) \tag{5.19}$$

The first term is the usual longitudinal propagation term. The second term represents the extra distance the parts of the beam off the optical axis travel due to its Gaussian profile. The final term, associated with the Guoy phase, indicates that as the Gaussian beam passes through a focus, it acquires an additional phase shift of π in addition to the usual phase shift expected from a plane wave.

The $(n+m+1)$ factor in eqn. 5.19 indicates that there are different phase shifts for different transverse modes inside the cavity. Consider a cavity formed with two mirrors of radius of curvature R_1 and R_2 positioned at z_1 and z_2 respectively away from the focus of the beam (a diagram is available in fig. 6.4 in the following chapter). The single trip phase shift along the z-axis would be:

$$\begin{aligned}\phi_{n,m} &= -kL + (n+m+1)[\Psi(z_2) - \Psi(z_1)] \\ &= \frac{\pi}{\Delta\omega_{FSR}}\omega - (n+m+1)[\Psi(z_2) - \Psi(z_1)]\end{aligned} \tag{5.20}$$

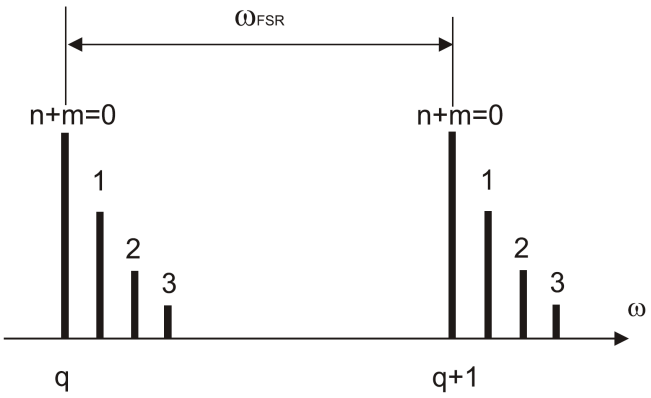

Figure 5.5: Transmission frequencies of transverse cavity modes.

Therefore the resonance eqn. 5.3 can be generalised to $\phi_{n,m} = q\pi$, giving:

$$\omega_{n,m,q} = \Delta\omega_{FSR}\left[q + (n+m+1)\frac{\Psi(z_2) - \Psi(z_1)}{\pi}\right] \tag{5.21}$$

where

$$\Psi(z_2) - \Psi(z_1) = \arccos\left(\sqrt{\left(1 - \frac{L}{R_1}\right)\left(1 - \frac{L}{R_2}\right)}\right) \tag{5.22}$$

is the Guoy-phase phase shift. This lifts the degeneracy of the transverse cavity modes, as shown in fig. 5.5.

5.3 ATOM-PHOTON INTERACTION

In our experiment, we wish to harness the power of the optical cavity in order to increase the interaction strength between light and matter. It is therefore necessary to analyse what happens when atoms are placed inside a cavity.

5.3.1 *Quantisation of the Electromagnetic Field*

Up until now we have only considered a classical treatment of the electromagnetic fields in the cavity. In order to understand the quantum mechanical properties of the field we must investigate it on a single photon level. We assuming that our cavity is limited to running in a single transverse mode while on resonance, the fundamental mode for instance. If the resonant mode is of frequency ω_c then the energy of the radiation field inside the cavity would be $n\hbar\omega_c$, where n is the number of photons in the field. Introduction of a photon into the field would raise the energy total by $\hbar\omega_c$ and removal of a photon would lower the total energy by $\hbar\omega_c$. This equidistant energy spacing lends itself to

an analogous treatment of the field as a harmonic oscillator with total energy:

$$E_{field} = \hbar\omega_c \left(n + \frac{1}{2}\right) \tag{5.23}$$

where the leftover $\frac{1}{2}\hbar\omega_c$ (when $n = 0$) is known as the *vacuum energy* or *zero-point energy*, which represents the underlying background energy of an empty electromagnetic field containing zero photons.

Consequently we can use the *creation* and *annihilation operators* of the harmonic oscillator, $\hat{a}^\dagger$ and $\hat{a}$, to represent the introduction or removal of a photon into the field; and to write the quantum mechanical Hamiltonian for the cavity as:

$$H_{cavity} = \hbar\omega_c \left(\hat{a}^\dagger\hat{a} + \frac{1}{2}\right) \tag{5.24}$$

with photon number eigenstates $|0\rangle$, $|1\rangle$, $|2\rangle$, ...

This is an idealised Hamiltonian which does not take into account any interaction with external environments.

5.3.2 *Atom-Cavity Coupling*

The seemingly stochastic emission of a photon from an excited atom can be considered as a stimulated emission induced by the vacuum fluctuations of a quantized electromagnetic field. This interaction with vacuum is dependent on the number of electromagnetic modes with which the atom is interacting. With the use of a resonant optical cavity, it is possible to engineer one vacuum interaction to be dominant over the rest, enhancing the change of spontaneous emission into that particular mode. The strength of this enhancement will depend on the specific characteristics on the cavity.

The strength of the interaction between the cavity and the atom is given by the coupling constant, g. In single-atom single-photon experiments, $g = \frac{\mu.E}{\hbar}$ where μ is the atomic dipole moment and E is the strength of the intra-cavity electric field generated by one single photon. For a cavity mode volume V and resonant cavity frequency w_c this is given by $E = \sqrt{\frac{\hbar\omega_c}{2\epsilon_0 V}}$, which leads to a coupling constant of:

$$g = \mu\sqrt{\frac{\omega_c}{2\hbar\epsilon_0 V}} = \sqrt{\frac{3\lambda^2 c\gamma}{\pi^2 w_0^2 L}} \tag{5.25}$$

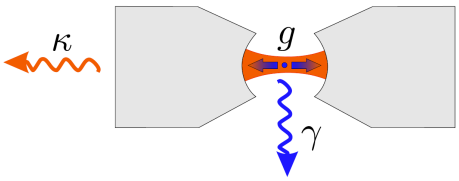

Figure 5.6: This shows the cavity QED parameters. Decays can occur via spontaneous emission of the atomic excited state or photon leakage from the cavity.

where L is the cavity length and w_0 is the waist of the cavity mode as defined in fig. 5.4.

In a real cavity, there are two decay processes (shown in fig. 5.6) that compete with the coupling of the atom with the desired cavity mode. The spontaneous emission of the atom into free space, with polarisation decay constant γ being the same as for a free atom; and the decay of a photon out of the cavity mode, dependent on a field decay constant $\kappa = \frac{\pi c}{2\mathcal{F}L}$, with $\mathcal{F}$ being the finesse of the cavity. This gives a combined effective decay rate of:

$$\gamma_{eff} = \gamma + 4\frac{g^2}{\kappa} \tag{5.26}$$

A useful parameter to define here is the *cooperativity*, which represents the ratio between cavity-enhanced stimulated emission and spontaneous emission into a non-cavity mode.

$$C = \frac{g^2}{2\kappa\gamma} = \frac{3\lambda^2\mathcal{F}}{\pi^3 w_0^2} \tag{5.27}$$

For $C \ll 1$ we are in what is known as the textitweak coupling regime where photons are lost from the atom-cavity system faster than the characteristic interaction time between the atom and the cavity. As discussed in the introduction, this is an irreversible effect which only allows for decoherent emission of photons in a similar way to spontaneous emission, which is undesirable for processing or transferring of quantum information stored within atoms. A more detailed discussion on weak coupling can be found in [59].

5.3.3 *Jaynes-Cummings Model*

As we increase to $C \gg 1$, we enter the textitstrong coupling regime. In these conditions the interaction between photons in the cavity mode and the atom is reversible. The atom emits a photon into a resonant mode, which then bounces between mirrors and is re-absorbed faster than it is lost from the mode. The interaction between a resonant quantised cavity field with a strongly coupled two level atom was first analysed by Jaynes and Cummings [60]. We summaries their model in this section.

Consider a two level atom which has ground state $|g\rangle$ and excited state $|e\rangle$ of energies $\hbar\omega_g$ and $\hbar\omega_e$ respectively. The Hamiltonian for such an atom in a resonant cavity mode would read:

$$H_{atom} = \hbar\omega_g|g\rangle\langle g| + \hbar\omega_e|e\rangle\langle e| = \hbar\omega_g\hat{\sigma}\hat{\sigma}^\dagger + \hbar\omega_e\hat{\sigma}^\dagger\hat{\sigma} \tag{5.28}$$

where we have introduced operators $\hat{\sigma}^\dagger = |e\rangle\langle g|$ and $\hat{\sigma} = |g\rangle\langle e|$ which create and annihilate atomic excitation.

In a closed system with no spontaneous emission, any change in the internal state of the atom must be reflected in the number of photons in the cavity. The atom can be excited by absorbing a photon from the cavity, or return to the ground state by emitting this photon back into the cavity:

$$H_{int} = \hbar g\left[|e\rangle\langle g|\hat{a} + \hat{a}^\dagger|g\rangle\langle e|\right] = \hbar g\left(\hat{\sigma}^\dagger\hat{a} + \hat{\sigma}\hat{a}^\dagger\right) \tag{5.29}$$

where g is the coupling constant.

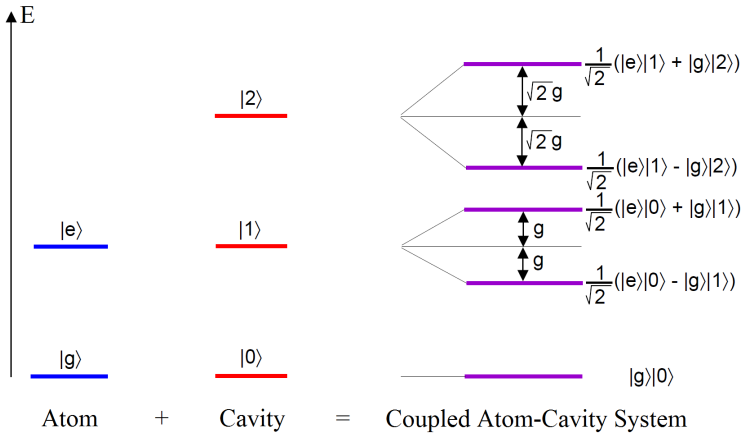

Figure 5.7: The eigenstates of a resonant two level atom-cavity system. The splitting of the combined system has been exaggerated for clarity and is not to scale.

The combination of the H_{cavity}, H_{atom} and H_{int} gives the total energy for a two level atom in the mode of an optical cavity is given by the total. This is know as the Jaynes-Cummings Hamiltonian:

$$\begin{aligned} H_{JC} &= H_{cavity} + H_{atom} + H_{int} \\ &= \hbar\omega_c \left(\hat{a}^\dagger \hat{a} + \frac{1}{2}\right) + \hbar\omega_0 \hat{\sigma}^\dagger \hat{\sigma} + \hbar g \left(\hat{\sigma}^\dagger \hat{a} + \hat{\sigma} \hat{a}^\dagger\right) \end{aligned} \tag{5.30}$$

where $\omega_0 = \omega_e - \omega_g$ is the frequency gap between ground and excited states.

In the submanifold of H_{JC}, we can write the Hamiltonian:

$$H_n = \frac{\hbar}{2} \begin{pmatrix} \Delta_c & 2\sqrt{n+1} \cdot g \\ 2\sqrt{n+1} \cdot g & -\Delta_c \end{pmatrix} \tag{5.31}$$

where $\Delta_c = \omega_c - \omega_0$ is the detuning between the cavity and atom.

This can be diagonalised to give the non-degenerate energy eigenstates of the combined system:

$$E_n = \pm\frac{\hbar}{2}\sqrt{\Delta^2 + 4(n+1)g^2} \tag{5.32}$$

These are known as *light dressed states* and are shown in fig. 5.7

To ensure the best atom to cavity coupling strength we would like the cooperativity of an atom-cavity system to be as high as possible. To increase cooperativity, we can decrease cavity losses (decreasing κ and/or γ). γ is difficult to control experimentally and we often wish to vary κ for specific desired outputs (such as decreasing the reflectivity of one mirror to encourage photons to exit the cavity in a certain direction). Alternatively we can increase the coupling constant g by decreasing the cavity mode volume. Through the use of microcavities with extremely small V we can achieve much high cooperativities than in standard macrocavities. Mode waists of 5 µm would not be unusual in such cavities. With such small waists, and for our desired 780 nm cavity resonance wavelength, even a cavity finesse as low as 5000 would achieve a cooperativity of 12. This would already satisfy our condition

for strong coupling, but we hope to achieve finesses much higher than this.

6

FIBRE-TIP MICROCAVITIES

In a fibre-tip cavity, the mirror substrates of the standard Fabry-Pérot cavity are replaced with two optical fibres. The tips of these are stripped down to the bare fibre (any protective insulation removed) and their end faces are ablated to form a concave structure. The ends are coated with a reflective dielectric stack and positioned facing each other to form the mirrors of the cavity.

The fabrication process, which will be discussed in more detail in the following chapter, involves shooting the tip of the optical fibre with a high power CO_2 laser, temporarily liquefying the glass surface. In 2006, Jakob Reichel's group at the École Normale Supérieure (E.N.S.) in Paris used such a process to produced concave fibre tips, and created a fibre-tip cavity [61]. Since then fibre-tip cavities have been gaining popularity with various groups adopting them, improving upon the fabrication and coating techniques.

Before fabrication, feasibility report was compiled discussing the inclusion of fibre-tip cavities into our DMD trapping experiment, while simultaneously alleviating many of the limitations of the setup by removing the dielectric mirror used to retro-reflect the incoming dipole trapping light [62]. This chapter is adapted and updated from the report to better fit the thesis. We consider both the design of the fibre-tip cavity itself, and schemes of how it would be integrated into a redesigned DMD trapping experiment.

6.1 CAVITY DESIGN CONSIDERATIONS

As mentioned in the previous chapter, one of the main benefits of using fibre-tip cavities is the extremely small mode volume which can be obtained, resulting in extremely strong atom-photon couplings. However, other advantages and disadvantages in implementing them for our particular experiment also need to be considered. We investigate these by comparison with a standard macroscopic Fabry-Pérot cavity.

Currently, other members of our group are using a Fabry-Pérot cavity as part of an atomic fountain based single photon pistol [26, 27]. If we were to use a macroscopic cavity in the DMD experiment, it would be similar to this in design. The cavity (shown in fig. 6.1) is constructed

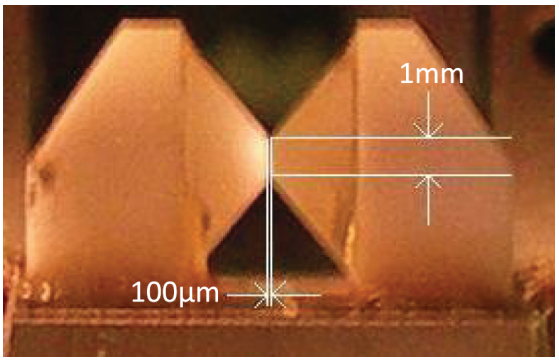

Figure 6.1: The Fabry-Pérot cavity used in the atomic fountain experiment. It is clear that the geometry would limit DMD dipole trapping light from entering the cavity.

from two ultra-polished high reflectivity mirrors, one with intensity transmission of $\mathcal{T}_\infty = t_1^2 = 2$ parts per million (ppm) for 780 nm wavelength light and the other with $\mathcal{T}_2 = 40$ ppm. Examining eqn. 5.6 and bearing in mind that r_1 and r_2 are amplitude coefficients of reflectivity, and that they are very close to 1 in our cases, we can simply our finesse equation:

$$\mathcal{F} = \frac{\pi\sqrt{r_1 r_2}}{1 - r_1 r_2} \simeq \frac{\pi}{(1 - \sqrt{\mathcal{R}_1 \mathcal{R}_2})} \tag{6.1}$$

where $\mathcal{R}_1 = (1 - \mathcal{T}_1 - \mathcal{L}_1)$ is the reflectivity of the first mirror and $\mathcal{R}_2$ is the reflectivity of the second mirror. With this we see our macrocavity allows for a maximum finesse of around 150,000. The higher transmission of one of the mirrors allows us to more reliably predict from which side of the cavity photons are likely to be emitted. The mirrors

both have a radius of curvature (ROC) of 5 cm and are mounted such that the separation between them is 100 µm. From eqn. 5.18 this cavity geometry gives us a fundamental mode waist of 22 µm. With this we calculate the cooperativity to be around 18 from eqn. 5.27, which would put us in the strong coupling regime. The mirrors are controlled using shear piezos[1] driven by a high voltage amplifier[2], providing a scan range of 300 nm with a 2 fm stability.

For the DMD experiment, we would like to form the single atom dipole traps within our cavity mode, with the optical axis of the dipole traps perpendicular to the optical axis of the cavity. The aspheric lens used to focus light coming from the DMD has a numerical aperture of 0.54, meaning the beam would converge to a focus into the cavity at an angle of 30°. For the Fabry-Pérot cavity, this would severely restrict our cavity length to a minimum of 1 mm in order to allow all the light in. At this separation the cooperativity would fall to around 6.

To the best of our knowledge, all previous fibre-tip cavities have been constructed using one single mode fibre for input of laser light into the cavity and one multi-mode fibre for the output. Multi-mode fibres have been used for the output so far due to the major difficulties in mode matching the cavity mode with the core of single-mode fibres. The fab-

1 Noliac CSAP03
2 Falco WMA-01LF

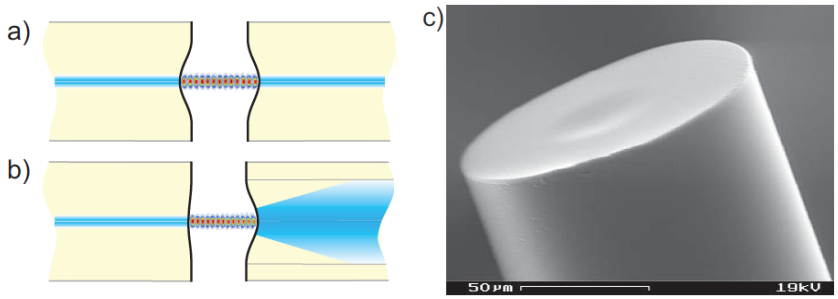

Figure 6.2: The concept of the fibre-tip microcavity with a) two single-mode optical fibres and b) with one single-mode and one multi-mode optical fibre. c) is an scanning electron microscope (SEM) image of a laser-machined fibre end face. Figure taken from [37].

rication process at E.N.S. produces a low-roughness concave depression on the fibre tip with ROC ranging between 40 µm and 2000 µm. Using interferometric microscopy they mapped the surface topography of the uncoated fibre surface (fig. 6.2) and obtained estimates of scattering loss through surface roughness ($\mathcal{S}$) of 10 ppm for $\lambda = 780$ nm [37]. An ion sputtering technique was originally used to deposit a multilayer coating on the end of the fibre tip. The group at E.N.S. measured finesses of 38,000 [36], but subsequently discovered that the imperfect coating technique produced a large amount of surface roughness which greatly limited the finesse. State of the art 'supermirror' coatings provide negligible increase in roughness, with absorption loss $\mathcal{A} = 2$ ppm being realistically obtainable [63]. With the new supermirrors the E.N.S. group have subsequently measured finesses of up to 100,00 [40]. Rainer Blatt's group at the University of Innsbruck has also investigated the use of

these fibre tips with supermirror coatings, applying them to ion trapping experiments. They have reported a finesse of 72,000 for a cavity length of 85 μm [39]. We would generally prefer to not lose most of the photons in a cavity through scattering or absorption, so as an example we choose transmission equalling losses (that is $\mathcal{T} = \mathcal{L} = \mathcal{S} + \mathcal{A}$). Using the above values we would chose $\mathcal{T} = 12\,\text{ppm}$, with eqn. 6.1 showing that we can expect a maximum finesse of around 130,000.

We do not wish to restrict the area within which the DMD can control the atomic positions of the trapped rubidium to anything less than 100 μm by 100 μm. Thus we require a cavity length of around 150 μm or more. At this separation, the waist at the centre of the cavity is 8 μm (for a ROC of 1 mm). With the mode volume for this waist being much smaller than that of its Fabry-Pérot counterpart, the fibre-tip cavity can achieve a cooperativity of 120.

6.1.1 *Fibre Coupling and Mode Matching*

A possible mismatch between the size of the cavity mode and that within the single mode fibre could be a substantial source of further loss which is absent in Fabry-Pérot cavities. The coupling loss into a

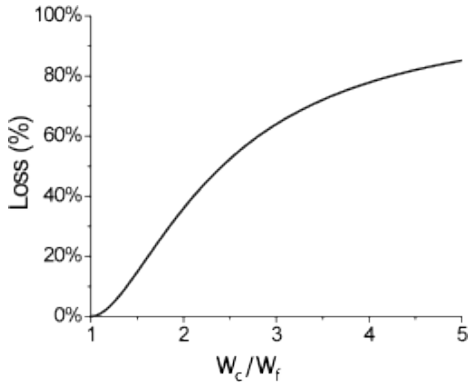

Figure 6.3: Graph showing the amount of coupling loss associated with a mismatched mode field radius of a single mode fibre.

fibre due to a mismatch in mode field radius (defined the same as w_0) is given by [64]:

$$\text{Loss} = 1 - \frac{4}{\left(\frac{w_c}{w_f} + \frac{w_f}{w_c}\right)^2}$$

where w_c is the waist of the cavity mode and w_f is the mode field radius of the fibre. This loss is plotted in fig. 6.3.

The mode field radius of the 780 nm single mode optical fibre[3] used in both the E.N.S. group and our experiment is 3.5 µm, which is a typical core size for light of this wavelength. We can see that for our expected cavity mode waist of 8 µm, w_c/w_f is 2.3, leading to a coupling loss of more than 45%. From this it is obvious that we will need to reduce the waist of the cavity mode.

3 Oxford Electronics SM800-125CB

In their current experiment (for which $\mathcal{F} = 38,000$ was experimentally obtained) the Reichel group have measured 80% single mode fibre coupling efficiency with a mode waist of 3.9 μm and a separation of 39 μm. In our experiment, the separation of the cavity mirrors is required to be much greater, so we must use a smaller ROC to achieve better fibre coupling. As mentioned, the laser machining technique can be used to create fibre tips with a ROC anywhere between 40 μm and 2000 μm, with there being no indication that the small ROC of the fibre mirrors causes any significant reduction of coating quality as compared to reference substrates.

The outer diameter of the fibres is 125 μm so the minimum mirror separation we can implement is 120 μm if we still wish to fit dipole trapping light into the cavity (limited by the 0.5 NA of the aspheric lens). If we use a 200 μm ROC with a mirror separation of $L = 120$ μm, we get $w_0 = 4.8$ μm mode waist. At the mirror surface ($w_1 = w_2 = L/2 = 60$ μm) this translates to a 5.7 μm spot size. This represents a 20% theoretical coupling loss. Reducing the ROC further, although decreasing the size of the waist, gives little reduction in the spot size on the mirror surface. Table 6.1 gives a comparison between a few different set of cavity specifications that could be used for the experiment.

Since a resonant mode in cavity is always incident perpendicular to the mirrors, this restricts how far we can decrease the ROC before light entering the fibre core is lost to the cladding. The numerical aperture of a fibre is an indication of the light collection angle range of the core, which light entering at a greater angle than this no longer being total internally reflected along the fibre. The single mode fibres used in both the experiment E.N.S. and our experiment have a numerical aperture of 0.1, which corresponds to a maximum collection angle of $\approx 5.7°$. The core diameter is 8 μm (radius 4 μm), meaning that for a fibre tip mirror ROC of 150 μm, the maximum angle at which light will enter the core (at the core/cladding edge) will be $\arcsin 4/150 \approx 1.5°$. We will mostly be operating at or above a ROC of 150 μm, so a numerical aperture of 0.1 should bear no restriction on our collection efficiency.

One way to further improve coupling efficiency would have been to obtain fibres with a large core/mean field radius or with a smaller diameter outer cladding to allow for a smaller separation. However it proved rather hard to obtain single-mode fibres with mode field radius bigger than 3.5 μm and there were disadvantages in compatibility (with mounts, couplers, etc...) when using fibres that did not come with the standard 125 μm diameter cladding. In the next section we investigate

	Fibre-Tip			Fabry-Pérot	
$\mathcal{T}_1$	12ppm	40ppm	40ppm	2ppm	2ppm
$\mathcal{T}_2$	12ppm	10ppm	10ppm	2ppm	40ppm
$\mathcal{A}$	2ppm	2ppm	2ppm	2ppm	2ppm
$\mathcal{S}$	10ppm	10ppm	10ppm	2ppm	2ppm
$\mathcal{F}$	130,000	85,000	85,000	525000	125,000
L	150 µm	120 µm	120 µm	1 mm	1 mm
R_1	1 mm	200 µm	200 µm	5 cm	5 cm
R_2	1 mm	200 µm	150 µm	5 cm	5 cm
w_0	8 µm	4.8 µm	4.3 µm	35 µm	35 µm
C	120	220	270	25	6
CL	45%	20%	8%	N/A	N/A

Table 6.1: Table comparing fibre-tip and Fabry-Pérot cavities. $\mathcal{T}_1$ and $\mathcal{T}_2$ are the transmissions of the two mirrors. Absorption ($\mathcal{A}$) and scattering ($\mathcal{S}$) losses apply to both mirrors. $\mathcal{F}$ is the finesse. L is the cavity length, R_1 and R_2 are the radius of curvatures of the mirrors, and w_0 is the waist of the cavity mode. C is the cooperativity. CL is the theoretical loss for coupling into a 3.5 µm mean field radius single mode fibre. The cooperativities in this table are calculated using $V = w_0^2 L$, assuming that the atom is trapped at the waist of the cavity mode.

an alternate approach which involves making the cavity asymmetric by having the ROC of one mirror larger than that of the other.

6.1.2 *Asymmetric Fibre-Tip Cavities*

Fig. 6.4 shows a optical cavity constructed from two mirrors of different ROC. The equations which govern the geometry of the fundamental mode formed inside such a cavity can be obtained by rearranging the equations in section 5.2.2:

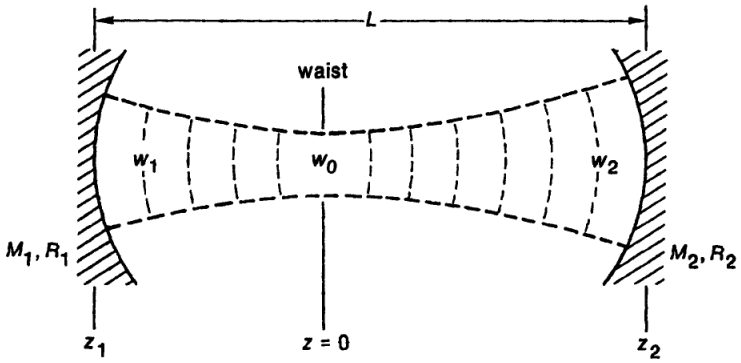

Figure 6.4: This shows a cavity comprised of two mirrors M_1 and M_2 with radius of curvature R_1 and R_2 respectively. w_0 is the waist of the Gaussian mode formed within the cavity, with w_1 and w_2 being the spot sizes on the surface of the mirrors. z_1 and z_2 are the distances of the mirrors from the waist and L is the total cavity length. Figure from [57].

$$w_0^2 = \frac{L\lambda}{\pi}\sqrt{\frac{g_1 g_2(1-g_1 g_2)}{(g_1+g_2-2g_1 g_2)^2}}$$

$$w_1^2 = \frac{L\lambda}{\pi}\sqrt{\frac{g_2}{g_1(1-g_1 g_2)}}$$

$$w_2^2 = \frac{L\lambda}{\pi}\sqrt{\frac{g_1}{g_2(1-g_1 g_2)}}$$

where $g_1 = 1 - L/R_1$, $g_2 = 1 - L/R_2$, w_1 and w_2 are the spot sizes of the mode on the surface of M_1 and M_2 respectively, and the other parameters are defined as in fig. 6.4. The distance of each mirror from the focus is also given:

$$z_1 = \frac{g_2(1-g_1)}{g_1+g_2-2g_1 g_2)}L$$

$$z_2 = \frac{g_1(1-g_2)}{g_1+g_2-2g_1 g_2)}L$$

Note that if mirror M_1 is located to the left of the beam waist, so that the waist is inside the cavity, then z_1 as measured from the waist will be negative.

It is obvious from these equations that real and finite solutions for Gaussian beam parameters and spot sizes can exist only if g_1, g_2 parameters are confined to a stability range defined by $0 \leqslant g_1 g_2 \leqslant 1$. As such, let us consider the example when $R_1 = 200\,\mu m$ and $R_1 = 150\,\mu m$, with a cavity length $L = 120\,\mu m$. From this we find $g_1 = 0.4$, $g_2 = 0.2$, which fulfills our stability criteria with $g_1 g_2 = 0.08$. With these parameters we can calculate the spot sizes of the mode at the mirrors:

$$w_0 = 4.3\,\mu m$$

$$w_1 = 4.7\,\mu m$$

$$w_2 = 6.6\,\mu m$$

So, if we were to use the fibre tip which forms M_1 as the output of the cavity, the mode matching loss when coupling into the single mode fibre would only be 8%. This is a considerable improvement over using a symmetric cavity. The extreme version of this would be to have an entirely flat fibre as the output fibre; with the correct ROC for the other fibre and cavity distance, we could achieve 100 % coupling efficiency. It

would presumably be very hard to construct such a cavity in a stable manner, but a few flat fibre tips were coated for experimentation.

6.2 THE ROLE OF THE LIGHT SHEET

In the proposed redesign of the DMD experiment, the dielectric mirror is removed to tackle the problems outlined in section 4.3. Instead we propose using the light sheet, which is previously used to illuminate atoms for fluorescence imaging, to confine the trapped rubidium atoms in a plane at the focus of the aspheric lens. The light sheet would operate on the same basis as a dipole trap, but is extended along one axis perpendicular to direction of propagation. The 'thickness' of the light sheet can be controlled by using a cylindrical lens to focus the laser beam down in one direction. The 'width' of the light sheet can be generated by imaging a slit of with 100 µm into the centre of the cavity (fig. 6.6), which will give uniform intensity distribution along that axis. How this appears inside the cavity is shown in fig. 6.5

We assume that the new light sheet will be implemented using a Toptica DLX110 laser running at 785 nm. The DMD dipole traps need to be focused down to around a 0.85 µm waist to enter the collisional blockade regime (this is equivalent to a FWHM or 1 µm). These traps

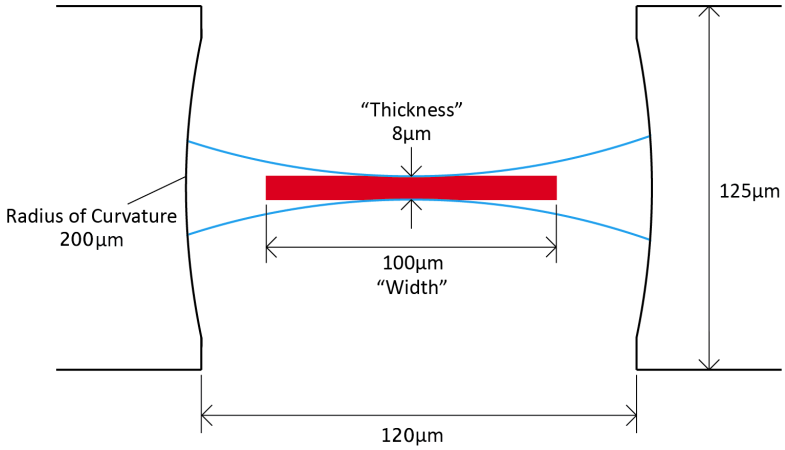

Figure 6.5: A cross section through the centre of the cavity in a plane perpendicular to the direction of propagation of the light sheet.

would have a Rayleigh length of 3 μm, representing good confinement in the axial direction. However when the larger transport traps are opened, the Rayleigh lengths become much bigger ($\gtrsim 100\,\mu m$) and we instead rely on the light sheet for confinement perpendicular to the DMD trapping light. Ideally we would like the waist of the light sheet to be around 3 μm as well. However at 3 μm the Rayleigh length of the light sheet would be only 35 μm. Considering that we wish to move the atoms around in a space of 100 μm by 100 μm, and how hard it will be to position the exact focus of the light sheet within the cavity mode, this Rayleigh length is somewhat inadequate. Since the Rayleigh length scales with w_0^2, increasing the waist slightly to the same as the waist of our cavity mode, which is 8 μm, gives us a much more reasonable Rayleigh length of 258 μm. This represents only a 7.1 % increase in the

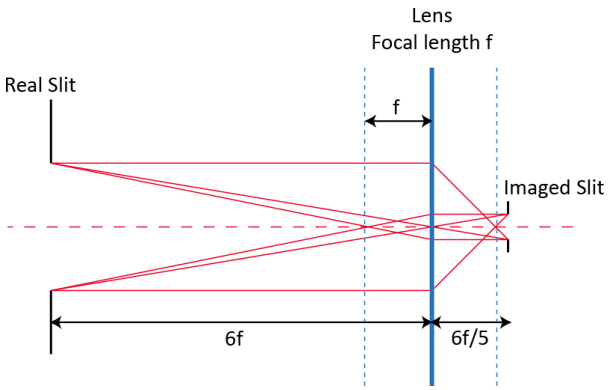

Figure 6.6: The 'width' of the light sheet is set by imaging a slit into the middle of the cavity. The setup shown is designed to give a magnification of 1/5 and so images a 500 μm slit into a 100 μm wide light sheet.

thickness of the light sheet over 100 μm either side of the focus, and a 1.9 % increase in thickness 50 μm either side of the focus.

6.2.1 *Transporting Atoms into the Cavity*

Since we hope to use the existing vacuum chamber for the redesigned experiment, the setup of the light sheet has to be designed around it. Ideally we wish the centre of the cavity to be in the centre of the vacuum chamber and the imaging components for the light sheet outside of the vacuum chamber. The distance from the centre of the vacuum chamber and the edge is 86 mm, so let us assume we want the cylindrical lens used to focus the light sheet down is 100 mm away from the cavity.

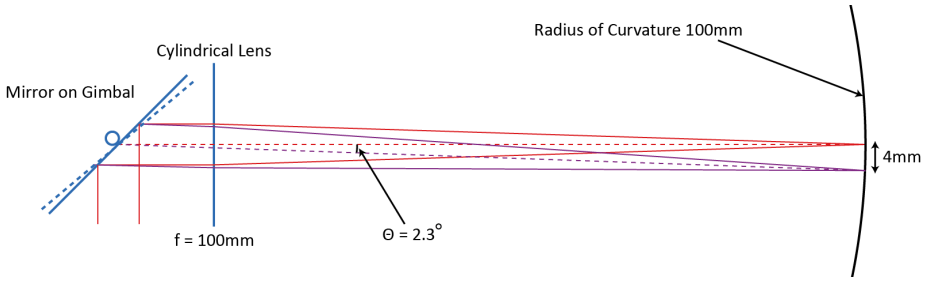

Figure 6.7: Collimated light striking an ideal thin lens will be focused according to the angle at which it hits the lens. Where the focus will be is defined by an arc with radius of curvature equal to the focal length of the lens. The red beam represents the beam when the light reflected off the gimbal mounted mirror is in the 'zeroth position', where it forms a well focused light sheet in the centre of the cavity. The purple beam shows the 'shifted position' of the light, which is focused to somewhere within the MOT cloud, where it can collect atoms. This demonstrates that the gimbal mounted mirror will have to deflect the light by 2.3° in order to move the focus by 4 mm.

Light hitting this lens must have a w_0 of 3.125 mm (6.25 mm diameter) to be focused down a 8 µm waist.

With the mount for the cavity and the aspheric lens, forming a MOT in the middle of the cavity will most likely prove to be difficult. It is thus proposed that the MOT be formed just below the cavity, and atom loaded into the light sheet. The light sheet will then be moved into place between the cavity mirrors. Once in place the DMD dipole traps can then be loaded with atoms from within the light sheet.

One way to move the light sheet is to move the cylindrical lens itself with a piezo stack. Since the distance moved in this scheme is relatively large ($\gtrsim 4$ mm), this seems like an inappropriate design. Instead, we consider using a mirror in a computer controlled gimbal mount to

change the angle of the incoming light by a small amount. Assuming that the light is well collimated as it is reflected off the mirror, and the mirror is close to the cylindrical lens which forms the light sheet (such that the tilt of the mirror changes mostly the angle of the light with little change to the position of where the light hits the lens), then we expect the light to behave as shown in fig. 6.7.

The setup will be such that the 'zero position' of the gimbal mounted mirror corresponds to a well formed light sheet that travels exactly through the centre of the cylindrical lens and has focus exactly in the centre of the cavity. The 'shifted position' then tilts the incoming light by 2.3°, which is the amount needed to vertically displace the focus of the light sheet by the required 4 mm. We can then load atoms into the light sheet from the MOT and transport them into the centre of the cavity. The exact position of the MOT can be shifted with magnetic bias coils to coincide with the focus of the shifted light sheet.

An alternative to moving the light sheet would be to take advantage of the fact the light sheet is essentially a dipole trap. We can thus load it from a MOT some distance away from the focus and allow the atoms to be drawn to the area of high intensity at the focus. The DMD light can also be used as an atomic funnel. We switch all the mirrors on the DMD to the 'on' position and create the MOT above the focus. When

the MOT beams are switched off, the atoms would fall under gravity and be guided by the DMD light to the cavity.

Since a dipole trap has no cooling properties, both these implementations would require a way of damping the motion of the transported atoms. This can be achieved simply by running a cooling beam parallel (or almost parallel) to the direction of transport, aided with cavity cooling which provides effective cooling along the cavity axis (such a scheme is documented in [65]).

6.3 ATOMIC CONFINEMENT WITHIN THE CAVITY

For light-matter interaction experiments, we would like a trapped atom to be well confined within the cavity mode. So at this point it would be useful for us to investigate what atomic confinement our new scheme, with the combination of DMD dipole traps and light sheet, has to offer.

6.3.1 *Dipole Trapping Light*

After the light from the DLX110 is reflected off the DMD, each mirror can be considered as a point source. The light passes through an ensemble of optics and the aspheric lens to form an airy pattern in the

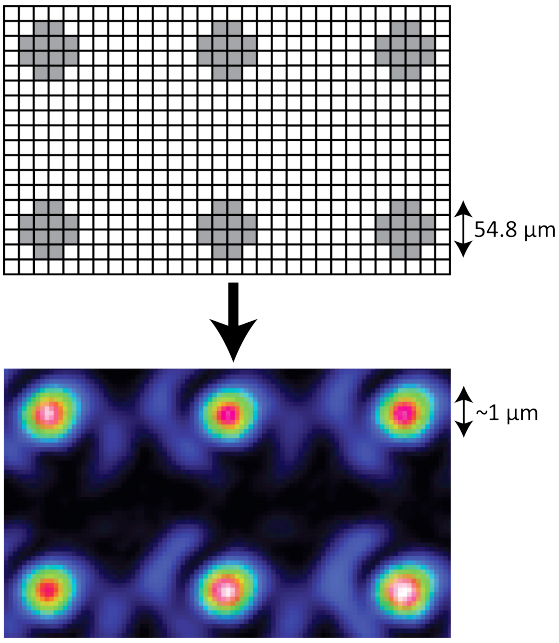

Figure 6.8: A 4 by 4 block of micro-mirrors (with the corners removed) forms a rough spot of size 55 μm. This is then focused to 1 μm to form the dipole traps.

trapping region. We can then convolute this airy pattern with the point spread function of all the micro-mirrors in the 'on' position to get the overall shape of the trap. For large traps, formed by a large number of mirrors, this is close to a top hat function with smooth sides. For small traps formed by a small number of mirrors, the shape of the trap to a good approximation is that of a Gaussian. The current magnification of the optical ensemble and aspheric lens is $M = 1/57$ and we can form traps with a FWHM of around 1 μm by using a 4 by 4 block of mirrors on the DMD with the corners removed (see fig. 6.8).

Thus we can assume for now a Gaussian intensity distribution:

$$I(r,z) = I_0 \left(\frac{w_0}{w(z)}\right)^2 e^{-\frac{2r^2}{w(z)^2}} \tag{6.2}$$

where z and r are the axial and radial directions respectively, and everything else is as defined in fig. 5.4. For a Gaussian intensity distribution, a FWHM of 1 µm translates to a waist ($1/e^2$) of 0.85 µm. Looking at radial confinement at the focus we set $w(z) = w_0$ and obtain the equation:

$$I(r) = I_0 e^{-\frac{2r^2}{w_0^2}} \tag{6.3}$$

The incident light on the DMD illuminates around 75% of its total area, and the total power of the light reflected off the DMD is around 230 mW when all the mirrors are in the 'on' position. This gives an average intensity of 3.9×10^{-4} mW/micro-mirror directly after the DMD. So the power that goes into forming each trap (made of the 12 micro-

mirrors) is 4.7×10^{-3} mW. Integrating over all space after the aspheric lens ($w_0 = 0.85\,\mu m$), we can obtain a value for I_0:

$$P = \int_0^{2\pi}\int_0^{\infty} I_0 e^{-\frac{2r^2}{w_0^2}} r dr d\theta = 2\pi I_0 \frac{w_0^2}{4} \tag{6.4}$$

$$I_0 = \frac{2P}{\pi w_0^2} \simeq 410,000\,mW/cm^2 \simeq 165,000\,I_{sat} \tag{6.5}$$

with I_{sat} being the saturation intensity of ^{87}Rb ($2.5\,mW/cm^2$).

6.3.2 *Potential*

Recall from eqn. 2.1 that the potential within a dipole trap resulting from a Gaussian beam is given by:

$$U_{dipole} \simeq \frac{\hbar\Gamma}{8}\frac{\Gamma}{\delta}\frac{I}{I_{sat}} = \frac{\hbar\Gamma}{8}\frac{\Gamma}{\delta}\frac{I_0}{I_{sat}} e^{-\frac{2r^2}{w_0^2}} \tag{6.6}$$

where Γ is the decay rate of the transition (the $5^2S_{1/2} \rightarrow 5^2P_{3/2}$ of the D_2 line in ^{87}Rb in our case) and δ is the detuning of the laser from resonance (negative for red detuning).

We can now find the outer limit of where an atom can be in this trap by assuming that after MOT cooling, the atom is at around 100 μK. At

the turning point it will have no kinetic energy and so we can equate $U_{dipole}(r)$ to $k_B T$:

$$\frac{\hbar\Gamma}{8}\frac{\Gamma}{\delta}\frac{I_0}{I_{sat}}e^{-\frac{2r^2}{w_0^2}} = U_{dipole}(0) + k_B T \tag{6.7}$$

$U_{dipole}(0)$ being the potential at the centre of the beam ($r = 0$) where the intensity is highest, and as such being the most negative point of the dipole potential (see fig. 6.9). In our experiment, $\Gamma = 38.12\,\text{MHz}$ and $\delta = c/785\,\text{nm} - c/780\,\text{nm} = -2.45\,\text{THz}$, which gives a trap depth of $U_{dipole}(0) \simeq -k_B(590\,\mu\text{K})$. From Chapter 4, we now know that experimentally the trap depth is actually much lower than this; somewhere of the region of $100\,\mu\text{K}$.

$$e^{-\frac{2r^2}{w_0^2}} = \frac{8k_B(-590\,\mu\text{K} + 100\,\mu\text{K})\delta}{\hbar\Gamma^2}\frac{1}{I_0/I_{sat}} \tag{6.8}$$

$$r^2 = \frac{w_0^2}{2}\ln\left[\frac{-8k_B(490\,\mu\text{K})\delta}{\hbar\Gamma^2}\frac{1}{I_0/I_{sat}}\right] \tag{6.9}$$

$$r \simeq 1\,\mu\text{m} \tag{6.10}$$

This means we can confine an atom within one of these traps to around 1-2 μm, which is more than sufficent to hold the atom within a cavity mode. Comparing this to the node separation of the cavity, which is around 390 nm (for 780 nm light), then it seems we will at best

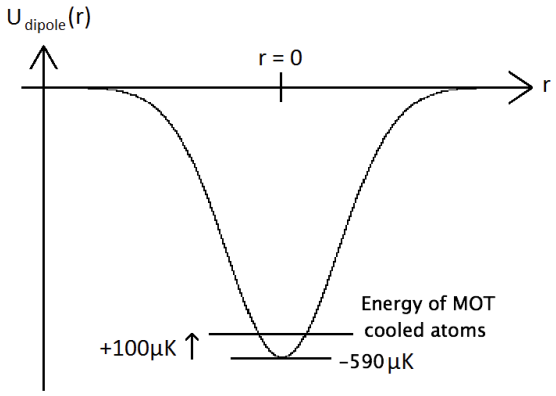

Figure 6.9: The confining potential generated by the DMD dipole trap within which an atom sits.

be able to confine the atom within a few nodes. However we might again be able to use a cavity cooling scheme to better localise the atom at an antinode [65].

6.3.3 *Axial Confinement*

Axial confinement will come from a combination of the proposed light sheet and focusing of DMD dipole trapping light.

An estimate of 100 mW can be used for the total power within the light sheet. As such:

$$P = \int_0^{100\,\mu m} \int_0^{\infty} I_0 e^{-\frac{2z^2}{w_0^2}} dz dy = (10^{-4}) \frac{I_0}{2} \sqrt{\frac{\pi w_0^2}{2}} \tag{6.11}$$

$$I_0 = \frac{2P}{(10^{-4})}\sqrt{\frac{2}{\pi w_0^2}} \simeq 20 \times 10^6\,\mathrm{mW/cm^2} \tag{6.12}$$

$$\simeq 8 \times 10^6\, I_{sat} \tag{6.13}$$

where dy is the integral over the full 100 μm 'width' of the light sheet, z now represents the 'thickness' of the light sheet (from the centre), and $w_0 = 8\,\mu m$.

Γ and δ remain the same, which gives a potential along the central plane of the light sheet ($z = 0$) of $U_{ls}(0) = -k_B(28{,}500\,\mu K)$. Again taking the turning point for MOT temperatures of 100 μK:

$$e^{-\frac{2z^2}{w_0^2}} = \frac{8k_B(-28500\,\mu K + 100\,\mu K)\delta}{\hbar\Gamma^2}\frac{1}{I_0/I_{sat}} \tag{6.14}$$

$$z^2 = \frac{w_0^2}{2}\ln\left[\frac{-8k_B(28500\,\mu K)\delta}{\hbar\Gamma^2}\frac{1}{I_0/I_{sat}}\right] \tag{6.15}$$

$$z \simeq 3.15\,\mu m \tag{6.16}$$

So the light sheet offers confinement of an atom within a 6.3 μm interval along the direction perpendicular to the DMD dipole traps.

For the DMD dipole trap axial confinement, we take the z dependence of the Gaussian intensity distribution along $r = 0$, to give a $U_{dipole}(z)$ of:

$$U_{dipole}(z) = \frac{\hbar\Gamma}{8}\frac{\Gamma}{\delta}\frac{I_0}{I_{sat}}\left(\frac{w_0}{w(z)}\right)^2 \tag{6.17}$$

We have values for $I_0 = 165,000\, I_{sat}$ and $U_{dipole} = -k_B(590\,\mu K)$ from the pervious section, so:

$$U_{dipole}(0) + k_B T = \frac{\hbar\Gamma}{8}\frac{\Gamma}{\delta}\frac{I_0}{I_{sat}}\left(\frac{w_0}{w(z)}\right)^2 \tag{6.18}$$

$$w^2(z) = \frac{\hbar\Gamma}{8}\frac{\Gamma}{\delta}\frac{I_0}{I_{sat}}\frac{w_0^2}{-k_B(490\,\mu K)} \tag{6.19}$$

$$w(z) \simeq 1\,\mu m \tag{6.20}$$

$$z = \frac{\pi w_0}{\lambda}\sqrt{w^2(z) - w_0^2} \simeq 1.8\,\mu m \tag{6.21}$$

From the focusing of the DMD dipole trap we can get a confinement within a 3.6 μm region for the 1 μm small traps, again this is well within our anticipated cavity mode.

Overall, the combination of the DMD dipole trap and light sheet should provide good confinement of an atom within the cavity mode and allow for strong coupling.

7

FIBRE-TIP FABRICATION

CO_2 lasers, typically operating at wavelengths of around 10.6 μm, have traditionally been a powerful tool for machining glass (or fused silica) surfaces. They have been used for surface polishing [66], repairing damaged optical elements [67] and tapering optical fibres [68]. The method utilises the thermal effects from strong absorption of the radiation within the first few μm to liquidate the material in a controlled and repeatable way, relying on surface tension in the molten layer to smooth out any surface imperfections up to scales comparable to the thickness of the layer.

At higher laser intensities the increased radiation absorbed causes a higher temperature within the molten layer. As the temperature approaches $T \sim 2600 - 3000\,K$ material loss due to evaporation becomes an important factor. For $T \geqslant 2800\,K$ the vapour pressure of the fibre material begins to exceed ambient room pressure and rapid ablation takes place. The concave profile at the fibre end face which we desire

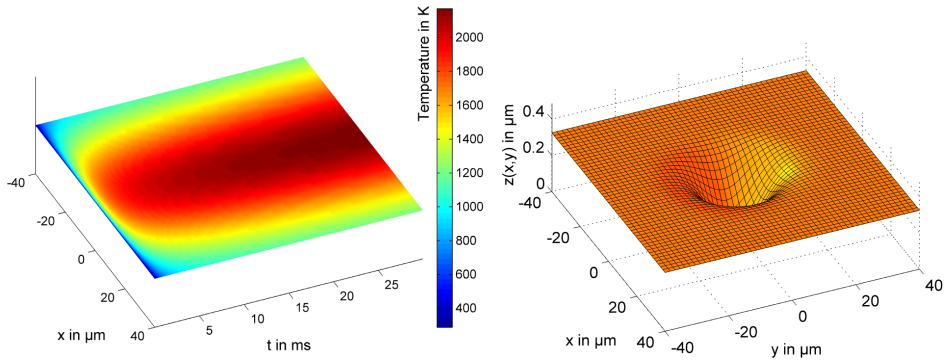

(a) (b)

Figure 7.1: (a) The calculated surface temperature of fused silica during the first 15 ms of irradiation from an incident CO_2 laser beam of P = 570 mW and $w_0 = 40\,\mu m$. (b) The corresponding expected surface profile for a laser pulse of duration $\tau = 15$ ms. Figure from [69].

for the use in fibre tip-cavities is mainly formed by direct evaporation of the fibre material. The Gaussian intensity distribution of the incoming laser radiation leads to a temperature distribution of similar shape (shown in fig. 7.1(a)). Hence most of the material is removed from the centre and resulting in a crater with a Gaussian profile (fig. 7.1(b)).

Due to surface area minimising effect of surface tension, the melting of large volumes of material results in the formation of convex structures. This has been employed in the fabrication of convex microsphere resonators [70] and the transformation of microdiscs into microtoroidal resonators [71], but is undesirable in our application. The thickness of the molten layer is the major deciding parameter for this process, and we must ensure this thickness is kept smaller than the desired lateral dimension of our ablation crater. The melt depth is primarily controlled by the duration of the laser pulse. Fig. 7.2(b) shows how this varies,

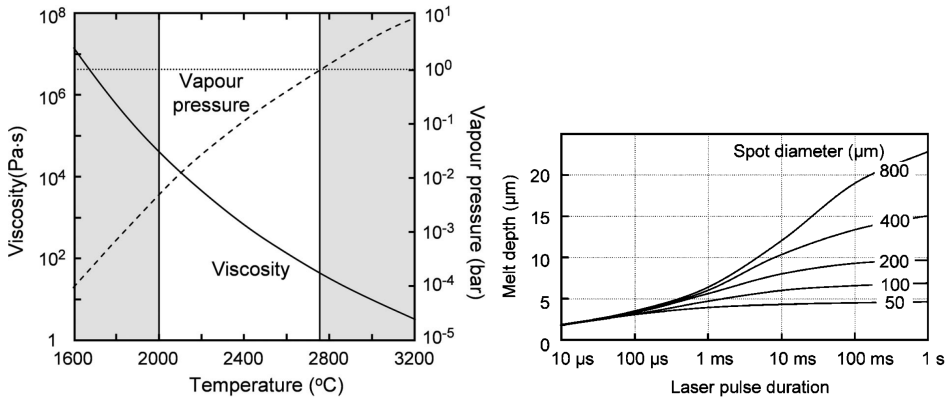

(a) (b)

Figure 7.2: (a) Variation of viscosity and vapour pressure of silica with temperature. (b) Variation of melt depth versus pulse duration for several different values of laser spot diameter. Figure from [67].

and how the increase starts to differ significantly for different spot diameters above pulse durations of ~500 µs. We can still take advantage of the surface tension to flatten out any irregularities on the end face, providing a smoothing effect on the surface. This helps mitigate any finesse loss of the final cavity due to surface roughness.

7.1 EXPERIMENTAL SETUP AND MANUFACTURING

There are a few major factors that influence the experimental setup of the fabrication system:

- Power Stability - The surface temperate of the fibre tip reached during the absorption process is proportional to P/w_0. Due to the exponential behaviour of the evaporation rate, even small fluctu-

ations in power can completely change the shape of the concave structure (a 1% variance in power for a pulse with $P = 570\,\mathrm{mW}$, $w_0 = 40\,\mu\mathrm{m}$ and $\tau = 15\,\mathrm{ms}$ changes the total structure depth by 18%) [69]. So for repeatable and predictable results the power must be controlled precisely on timescales for both fibre preparation ($\sim$ min) and ablation pulse duration ($\sim$ ms).

- Positioning - Ideally we would want the evaporated concave to be directly centred onto the fibre core, which is necessary for efficient coupling of core and resonator modes. To achieve this we would like precise control over the position perpendicular to the beam axis ($x-$ and $y-$ axes). Vibrations through the fibre or beam optics, as well as long term drift, should be minimised. Accuracy of adjustment in parallel to the beam ($z-$axis) affects the spot size, and so is important for the same reasons as in the previous bullet point.

- Dust Free Environment - Any dust on the tips of the fibres is hugely detrimental to the dielectric coating process. Since the size of the fibre-tip mirrors and fibre core are so small, any dust can completely destroy the finesse of a fibre-tip cavity or block light from entering/exiting the fibre. Thus any contamination prior to coating would demand a suitable cleaning process. The best

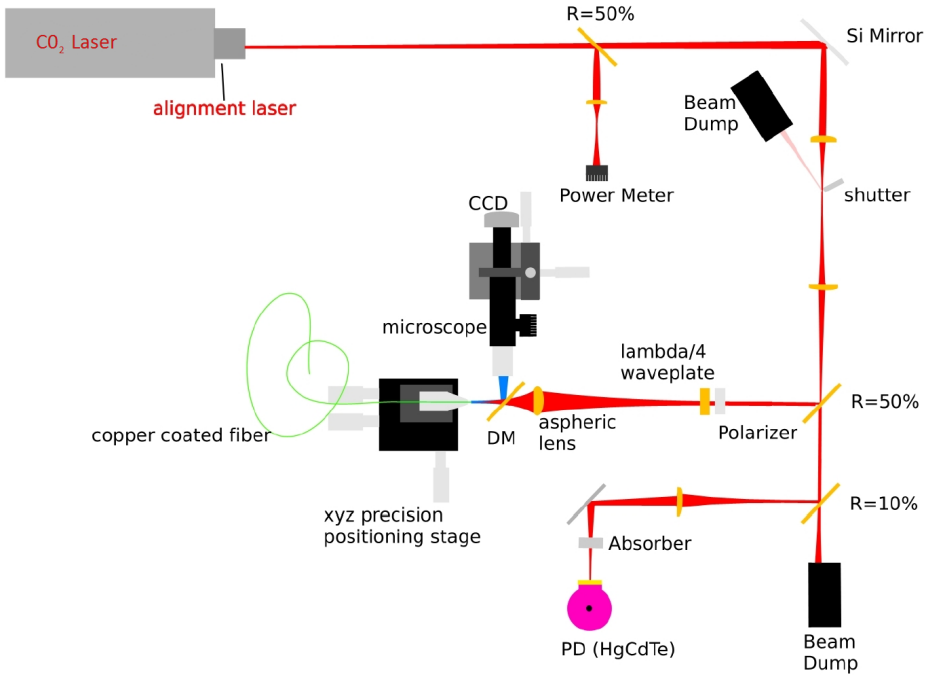

Figure 7.3: The setup of the apparatus for the CO_2 laser ablation of fibre tips. Figure from [69].

cleaning mechanism comes from the laser blast itself, so keeping the fibre clean afterwards is the most preferable solution.

Fig. 7.3 shows the experimental setup for fabricating the fibre tips. The CO_2 laser[1] provides 10.6 µm light which passes through a telescope-like lens ensemble and focused down onto the cleaved end facet of the fibre by an aspheric lens. A dichroic filter, set up to transmit 10.6 µm light, reflects visible light into an CCD camera[2] attached to an optical microscope[3], allowing us to observe the fibre tip. A solid state laser emitting 650 nm light is attached to the output of the CO_2 laser and is

1 Synrad Firestar v20
2 DeltaPix DP300
3 Navitar Ultrazoom 12x

set up to propagate coaxially with the IR beam, aiding in the alignment of the optical elements. A polariser along with a $\lambda/4$ waveplate are included as an optical isolator to minimise feedback.

The fibre is held onto a metallic v-groove block with a magnet. And the block itself is mounted onto translational stage, providing x, y and z-axis degrees of freedom. The stage allows high precision adjustments of the fibre in all three directions when viewed through the microscope. The most effective way to control the duration of the pulse is to block the beam using a tiny mirror glued to a mechanical shutter, which diverts the light into a beam dump.

A thermopile detector[4] is used to monitor the beam power. The power at this location is cross calibrated with the beam power at the fibre position. The response time of this detection system is $\sim 1\,\mathrm{s}$, so a liquid nitrogen cooled HgCdTe-Photodiode is included to monitor the short term behaviour of the laser up to a rate of $50\,\mathrm{MHz}$. The whole apparatus is set on a breadboard which is vibration damped through active pneumatic regulation; and placed in a flow box delivering dust free air.

Before fabrication began, mountings to house the produced fibres were manufactured. The design of these mounts had to take into con-

4 Newport 818P-020-12

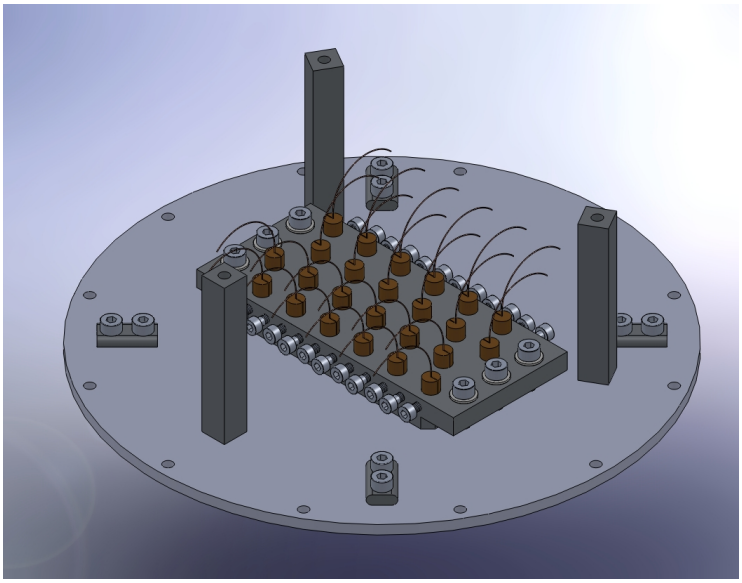

Figure 7.4: The mount for the storage, transport and eventual coating of the manufactured fibre tips.

sideration the clean storage and transport of the fibres for the eventual reflective coating process, which is documented in further detail in a subsequent section. Fig. 7.4 shows a schematic for the transport module. A thin brass tab holds the fibre itself into a cylindrical brass chuck. An aluminium block is machined to fit 24 such chucks. Each chuck hole has a thin rim which is designed to hold the chuck 1.5 mm above the bottom face of the block. This allows the fibre to protrude over edge of the chuck, helping to keep the tip clean and exposing it the for coating process. The aluminium block then sits on a aluminium disc such that the fibre tips are face down, protecting them from contamination. The detached block is specified to fit within the coating apparatus directly, eliminating the need to remove the fibres and risk contamination.

The dielectric coating process takes place within a vacuum chamber under high heat. Standard acrylate polymer coatings used to protect optical fibres do not fare well in such conditions. So instead fibres coated in CuBALL copper alloy, which is stable up to 500°C, were used. Prior to exposure to the laser, the copper was removed using Fe(III)Cl solution (although nitric acid would be a recommended alternative). The stripped fibres were cleaned carefully and cleaved with a high precision ultrasonic cleaver[5] to produce a clean, flat and orthogonal end facet to the fibre. The cleaving process often leaves small kinks and glass fragments on the surface of the fibre, but these are smoothed out by the laser pulse, which blows away any residual dirt left from the cleave.

To calibrate the system, the laser is first shot at a glass plate with varying powers at pulse durations. These are then examined to determine their ROC and depth, giving us a rough starting point for the fibres. This was also used to ensure that the centre of the laser we aligned to a marker on the screen. Several test fibres were produced initially to ensure we were getting our desired ROC range, and that the fibre core was at the centre of the laser shot. Fig. 7.5 shows how the fibre looks before and after exposure to the laser.

5 Photon Kinetic FK 12

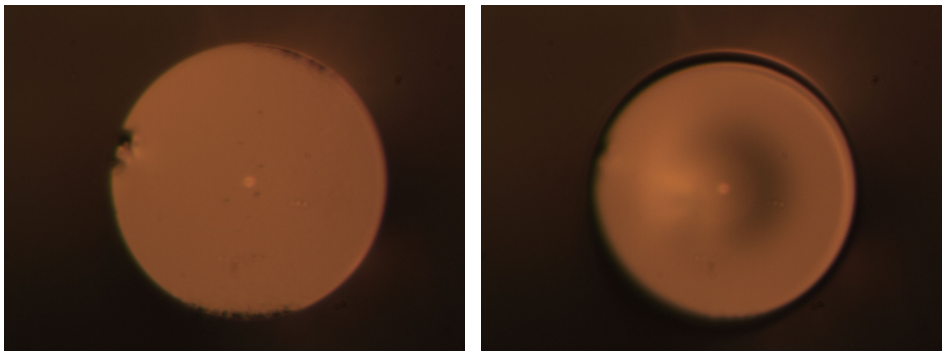

(a) Before (b) After

Figure 7.5: CCD pictures taken of the fibre end face (a) before and (b) after a pulse from the CO_2 laser of power 3.02 W and duration 14.5 ms. This resulted in a crater of diameter of 41.2 µm and depth of 1.75 µm, with a ROC of 209 µm along its minor axis and ratio of 1.09 between the ROC of the major and minor axes.

Fabrication was focused mainly on producing single mode fibres[6] - 125 µm CuBALL cladding, 7 µm core diameter, NA 0.1, designed for 780-800 nm light. However a few graded index multimode fibres[7] where also prepared- 125 µm CuBALL cladding, 50 µm core diameter, NA 0.15. The fibres were prepared in batches of 24 before characterisation. Those which were found to be contaminated or where the mirror was not in line with the fibre core, were re-fabricated. A total of 72 usable fibre tips (three blocks) were made from around 150 fabrications.

6 SM800-125CB
7 G150-125CB

7.2 CHARACTERISATION

A important part of the fabrication process in the characterisation of the concave structure left by the laser pulse. The overall shape of the fibre tip is measured by optical interferometric profiling. Fig. 7.6 shows a typical laser ablated surface. From this we are able to obtain the radius of curvature, R; the structure diameter, d; the structure depth, t; and also the ellipticity of the craters. Each fabricated fibre was profiled in this way, with dirty or damaged ones sent back for re-machining.

The surface roughness is determined by atomic force microscopy (AFM) measurements at different positions on the fibre tip, with scan areas of 0.5, 2 and 5 μm. All noise corrected measurements show a comparable roughness of $\sigma = 0.22\,\text{nm}$ rms [40]. The scattering loss this causes can be estimated by $\mathcal{S} \approx (4\pi\sigma/\lambda)^2$ [72], which predicts $\mathcal{S} = 12.6\,\text{ppm}$ at $\lambda = 780\,\text{nm}$.

7.3 DIELECTRIC COATING

The final part of the fabrication process is to coat the fibre tips with a reflective dielectric stack, creating the mirrors which are ultimately

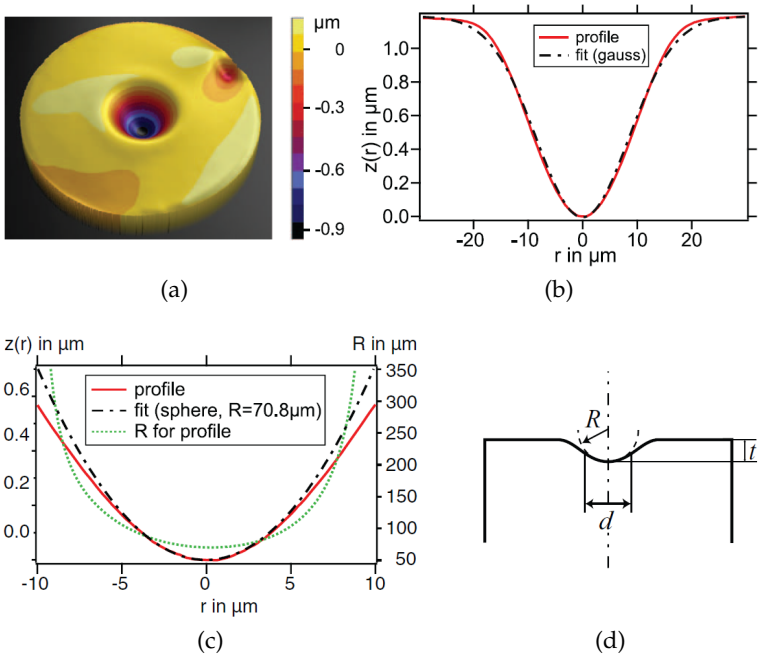

Figure 7.6: (a) Surface profile of a machined fibre measured by optical profiling. Beam parameters are $P = 420\,\mathrm{mW}$, $w = 28\,\mu\mathrm{m}$, $\tau = 27\,\mathrm{ms}$. (b) Cut through the centre of the profiled fibre tip (solid red line) and its fit to to a Gaussian (black dash-dotted line). (c) Central part of the same data (solid red line) along with a circle fitted to the centre yielding $R = 70.8\,\mu\mathrm{m}$ (green dotted line). Also shown is the local radius of curvature as calculated from a high-order polynomial fit to the data (green dotted line). (d) Quantities used to characterize the profile. R designates the radius of curvature in the centre of the structure. d is the structure diameter and t the depth of the structure. Figure from [40].

used to form a cavity. This was done through the company Advanced Thin Films who use an ion spluttering (IBS) technique whereby high energy ions are used to eject material from a dielectric source, depositing the it layer by layer upon the fibre tips. This technique has the advantage of yielding extremely low absorption ($< 2\,\mathrm{ppm}$) coatings with extremely low surface roughness ($< 1\,\text{Å}$), which helps minimise losses due to scatter. To produce such low absorption and surface roughness,

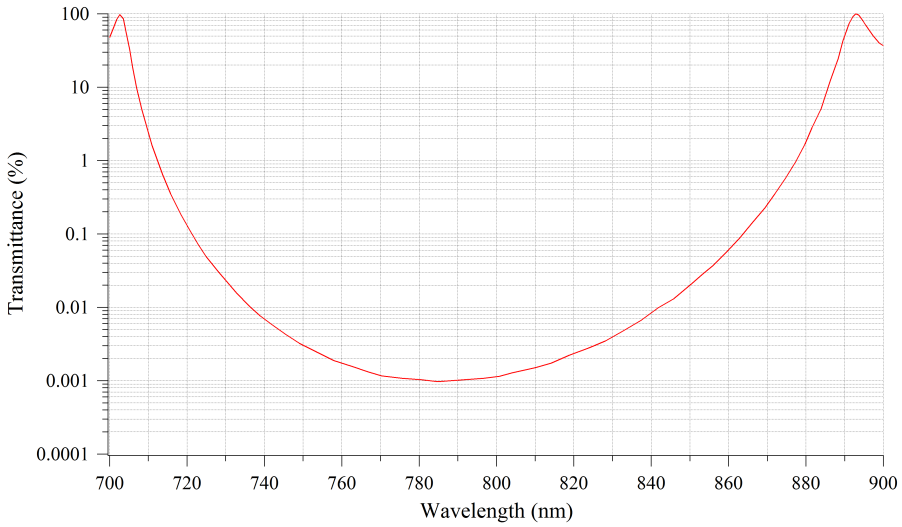

Figure 7.7: This is a graph showing the theoretical transmission of the dielectric coating with respect to the wavelength of incident light.

the deposition process takes place within a vacuum to reduce the possibility of contaminates becoming trapped within the dielectric layers. As mentioned previously our fibres were initially held in brass chucks. However the outgassing rate of brass, at 4×10^{-6} torr litre/s/cm^2 [73], is very high compared to that of other metals and had the potential to lower the quality of the coatings. Aluminium, from which the rest of the transport module was made, has an outgassing rate of only 7×10^{-9} torr litre/s/cm^2, three orders of magnitude lower than that of brass. So to help ensure the highest quality coating possible, we transferred the fibres from the original brass chucks to new aluminium before coating.

Fig. 7.7 shows the theoretical transmission profile of the dielectric coating we requested. Both the value of minimum transmission and wavelength where this minimum rests can be controlled with the IBS coating technique. We would eventually like to manipulate the hyperfine states of ^{87}Rb atoms held within the cavity and ideally be able to interchange between the D1 and D2 transitions, which are at 795 nm and 780 nm respectfully. A theoretical transmission curve with a minimum transmission of 10 ppm resting at 787 nm would result in a 12 ppm - 14 ppm transmission at the 795 nm and 780 nm. In reality the minimum wavelength can only be controlled with a precision of ± 7 nm, so the experimental transmission at these wavelengths could lie anywhere between 10 ppm and 15 ppm.

8

CAVITY CHARACTERISTICS

As mentioned in the introduction, our ultimate application for the fabricated fibre tips is to construct a cavity which we can move dipole trapped atoms into for state manipulation experiments. Previous cavities attempts by other research groups have mainly focused on cavities made from one single mode and one multimode fibre, which are easier to realise due to the large core diameter of the multimode fibre providing easy coupling to the cavity modes. While these are useful for applications such as atom detection and state readout [74], for full coherent control of the internal state of an atom, we require a cavity comprising of two single mode fibres to preserve coupling into one single optical mode. This is essential if we wish to use any output photons as flying qubits to transmit information within a quantum network [16], for remote entanglement of atoms [75] or for linear optical quantum computation experiments [76]. This chapter outlines how we made the first

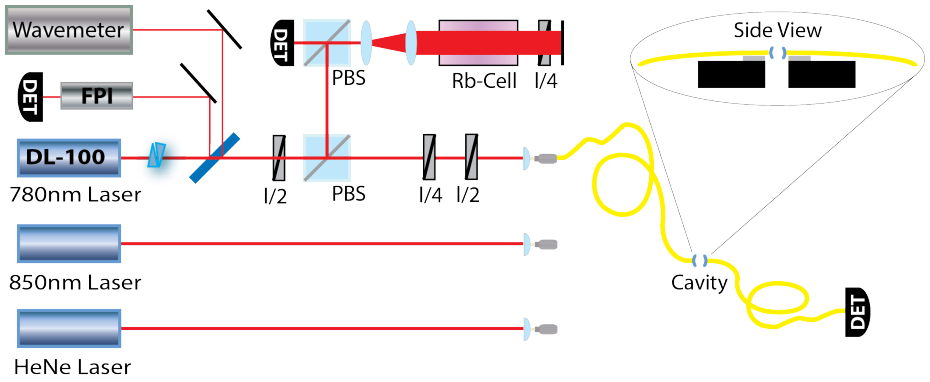

Figure 8.1: The experimental schematic for the alignment and characterisation of a single mode to single mode fibre-tip cavity. The input fibre can be moved to one of three lasers (discussed in the text). The bubble contains a zoomed in side view of the cavity. The fibres (in yellow) sit facing each other to form the cavity (in blue). They rest on shear piezos (in grey) which can scan the cavity length. The piezos are attached to translation stages (in black) which allows for control of the angle position of the fibres.

(to the best of our knowledge) single mode fire to single mode fibre-tip cavity and characterises some of its essential features.

Fig. 8.1 shows our full experimental setup, which is examined in great detail in the following section. For the purpose of this experiment, we assume that we will eventually wish to address the 780.24 nm D2 line of a ^{87}Rb atom confined with our DMD dipole trapping apparatus. Thus a Toptica DL100 laser running at 780.24 nm is coupled into the single mode input fibre of the cavity. Another single mode fibre is used for the output, which feeds light transmitted by the cavity directly to a photo diode. Each fibre is attached to a shear piezo, allowing it it be scanned over a 530 nm range, and both piezos rest on translation stages which control the cavity alignment. Two further lasers are included

in the setup to help in the alignment process. The entire experiment, including any fibre preparation steps, is carried out on a sealed optical table under a flowbox to minimise the risk of dust contaminating the cavity mirrors.

8.1 CAVITY SETUP AND ALIGNMENT

Before we can attempt a cavity setup with the coated fibres, the uncoated end must first be connectorised to allow light to be coupled into it. An alternative would be to cleave the uncoated end and couple into the bare fibre, but this can be tricky, and using connectorised fibres gives us the ability to couple various different lasers into the cavity simply by attaching the connectorised end of the input fibre to a different coupler. The Thorlabs connectorization kit[1] was used to terminate the fibres with FC/APC single mode connectors[2]. These had a ø126 µm bore (designed to fit 125 µm fibres) and are polished at an angle of 8° to prevent reflected light from travelling back along the same path. The copper coating of the optical fibres was quickly removed with nitric acid, leaving behind a graphite layer. Although extremely thin, this was enough to prevent the fibre from fitting inside the connector bore.

1 Thorlabs CK05
2 Thorlabs 30126A9

A concentrated sodium hydroxide solution was used to slowly dissolve the graphite layer over 8 - 10 hours. The snug fit of the bare fibre into the bore helps ensure that the fibre core was in the same place over different connectorised fibres. This means that once light is coupled into a fibre it can be replaced with another similarly terminated fibre and still maintain at least a few percent coupling efficiency; or that the fibre can be placed into other similarly aligned laser and coupler systems. This flexibility in switching between different connectorised fibres (or the same fibre to different lasers) turned out to be extremely useful when initially setting up a cavity and when testing different fibre tip combinations.

8.1.1 *Fibre-Tip Mounting*

Due to their small mode volumes, alignment of fibre-tip cavities must be extremely precise. Both in order to get the right translational and angular geometry to form a cavity mode in the first place, and to ensure this mode is coupled to the core of the output fibre. To achieve this level of precision we mount the fibres onto multi-axis translation stages with finely threaded actuator screws. The first translation stage is a 5-axis

unit[3] with piezo driven actuators, and the second is a 3-axis stage with manual actuators for coarse adjustment. 125 µm v-grooves are attached to the mounts, within which sit the two fibre tips facing each other. In the experimental setup the fibres were simply anchored into the v-grooves using Blu-Tack, since the fibres needed to be easily exchanged or adjusted. A better attachment solution would be recommended for any future designs, as Blu-Tack would occasionally snap the tips of the fibres while they were removed.

The 5-axis stage is driven by an Ethernet control module[4]. Two of the three translational axes are controlled by two actuators each. If these these are driven asynchronously (one forward, one back for example) a tilt can be created relative to the translation axis, giving us a small degree of angle control when aligning the cavity. Although a hand input terminal[5] is attached to the control module for simple executions, the module also accepts a set of Telnet commands which can be used to control the individual piezo actuators. A LabVIEW program was written to utilise these commands in a meaningful way to control the stage.

3 New Focus 9081
4 New Focus Intelligent Picomotor Control Modules. A pair of Model 8753 drivers attached to a Model 8750 Ethernet controller.
5 New Focus Model 8757 Intelligent Picometor Hand Terminal.

The piezo actuators work on a 'stick-slip' principle of static and dynamic friction. Two jaws grasp the finely threaded screw, and a piezoelectric transducer slides the jaws in opposite directions. Slow action of the actuator (high static friction) causes the screw to rotate while fast action (low dynamic friction) causes no rotation. By sending pulses with fast rise and slow fall times, the piezo will rotate the screw counterclockwise. Similarly, pulses with slow rise and fast fall times will cause a clockwise rotation. The operating principle of these actuators turned out to be ill suited to our needs. Because it is a friction mechanism, it does not produce identical steps for each input pulse. This made it hard to accurately change the translation or angle in a finely controlled manner, and meant we could not step back exactly to a previous location. On top of this, there was a considerable hysteresis effect when changing the direction of a motor. Despite these issues, the specifications state a step size of sub 30 nm per pulse, which was sufficient for cavity setup. For future experiments, extremely fine threaded manual actuators with piezo stacks at the tips for precision control would be suggested. These would allow for a more continuous, precise and repeatable scan over the region of interest.

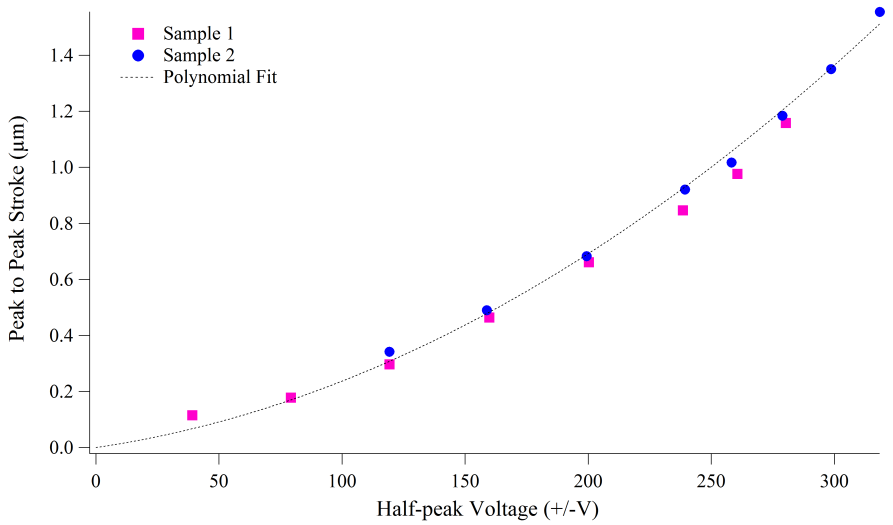

Figure 8.2: A graph showing the scan range of the shear piezo for different applied peak voltages. The form of the fit is quadratic.

Sandwiched between each mount and v-groove is a shear piezo[6]. The piezoelectric material is non-linear with respect to the voltage applied to its surfaces; its behaviour takes a quadratic form up to a maximum voltage of $\pm 320\,\mathrm{V}$, as shown in fig. 8.2. The material also exhibits a hysteresis when scanned peak to peak. The shape of the hysteresis curve varies depending the load on top of piezo, the voltage range, and the shape and frequency of the applied signal. The shear piezo is driven with a battery powered high voltage amplifier[7], capable of outputting $\pm 175\,\mathrm{V}$ with extremely low noise ($< 0.2\,\mathrm{mVrms}$). This allows the piezo to be scanned over $\sim 530\,\mathrm{nm}$ peak to peak, which is more than sufficient to scan over one free spectral range of a cavity for 780 nm light. The

6 Noliac CSAP03
7 Falco WMA-02LF

amplifier takes an input signal from a function generator. The generator provides a triangle wave to scan the piezo, and can also incorporate a DC offset so we can adjust the cavity length to match a particular transmission peak. The low noise is partially provided by a low pass filter attached internally to the input of the amplifier, causing the maximum output voltage to drop rapidly for scan frequencies greater than ~ 30 Hz.

8.1.2 *Laser System*

Fig. 8.1 shows the setup of the laser system used to couple light into the fibre-tip cavity. The system is a composite of a 633 nm helium-neon (HeNe) laser pointer, a collimated infra-red laser diode running at ~ 850 nm, and a grating-stabilised external cavity diode laser running at 780.24 nm. The DL100 is set up in a very similar way to the rubidium cooling laser in the diode trapping portion of the experiment. Light exiting the external cavity passes through an optical isolator before an amorphous prism pair corrects its beam profile from elliptical to circular. A glass plate is used to create two weak reflections, to provide light for the wavemeter and Fabry-Pérot interferometer. A small fraction of the light is then siphoned off to pass through a rubidium vapour glass

reference cell, expanded to fill up the entire cross section of the gas. The siphoned light is retro-reflected back through the reference cell and focused onto a photo diode, providing a high resolution Doppler-free saturated absorption spectrum. This is used to monitor the exact output of the DL100 and to allow locking of the laser to a resonant transition. The reference cell contains both ^{85}Rb and ^{87}Rb, and the large tuning range afforded by the grating feedback external cavity setup allows us to lock to any D_1 or D_2 transition crossover line from either isotope. For now the laser runs on the D_2 line of ^{87}Rb at 780.24 nm. Each of the laser systems ends in a collimator which focuses the light into the core of a fibre. A connectorised test fibre, with no dielectric coating, is used to optimised the in-coupling. This fibre is then be exchanged for the input fibre of the cavity. A $\lambda/4$ and $\lambda/2$ waveplate sit just before the collimator, allowing us to fully control the polarisation entering the cavity.

The coefficient of reflectivity of the dielectric coating deposited on the end face of the fibres is extremely high for 780 nm light. So in order to get any light from the input fibre, through the cavity and into the output fibre, the cavity must be aligned well enough for a cavity mode to potentially exist. This mode must then be sufficiently well coupled with the core of the output fibre and the cavity must also be extremely close

to resonance. As this is nearly impossible to do all at once, we can use a laser which is running at a wavelength where the reflectivity of dielectric coatings is extremely low to aid the alignment process. Coupling this laser into the input fibre, we can at least ensure that the fibre cores are coaxial by adjusting the position of the fibres until transmitted light is detected exiting the output fibre. A HeNe running at 633 nm serves this purpose well, and although we do not know the exact reflectivity of the dielectric coating at this wavelength, the coefficient is sufficiently low that we can easily detect light transmitted directly though the cavity. By observing the light exiting the output fibre, we can optimise the coupling efficiency of the HeNe into the input fibre and adjust the translation stage to maximise transmission. The small amount of reflection provided by the coatings (and the glass surface of the fibre) gives us a weak cavity effect, albeit with very low finesse. The peaks are extremely broad, but by adjusting the angle and position of the fibres to get the most pronounced effect, we can maximise the chance of forming a cavity mode when the connectorised end of the input fibre is transferred to the DL100.

8.2 SINGLE MODE TO MULTIMODE FIBRE-TIP CAVITY

The first cavity we attempted and realised was formed form a single mode fibre as the input fibre, and a multimode fibre as the output fibre. The multimode fibre has a core diameter of 50 µm, around an order of magnitude larger than the single mode core, making it significantly more likely that it will be coupled with any cavity mode which exists. Following the rough setup process with the HeNe laser, the input fibre was transferred to the 780.24 nm laser. The cavity was then scanned over the three translational axes in order to find a faint transmission signal. This process of switching the fibre between lasers would occasionally need to be repeated a few times to detect any light. After a faint signal was observed, we altered the different angle and translation settings of the stage to optimise the transmission.

Only 7 multimode fibres were fabricated and sent for coating. Out of these, some were chipped upon inspection under the camera. This most likely occurred during the transfer of fibres from the brass chucks to the aluminium ones. A few other ones had not be coated correctly since they had sunk into the chuck and were shielded during the coating process. It was also extremely difficult to remove the fibres from the chucks, so they occasionally had their tips snapped off, or slipped

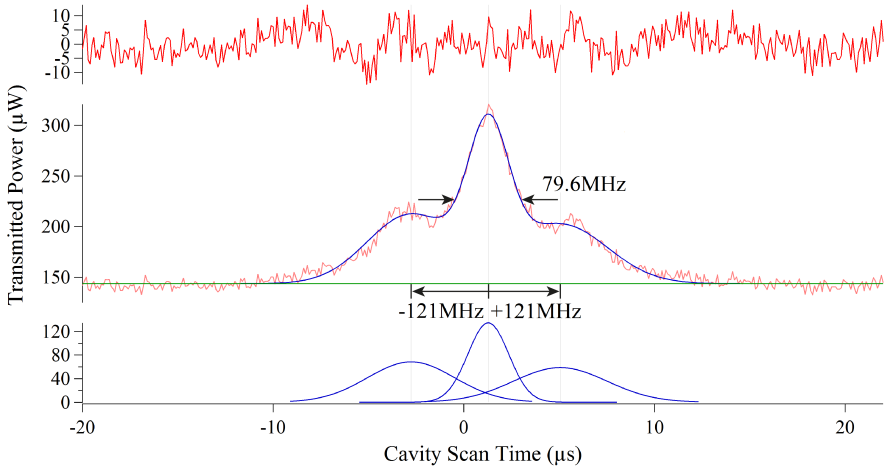

Figure 8.3: The transmission spectrum of 780.24 nm laser light through a single mode to multimode fibre-tip cavity, close to the fundamental mode. The FWHM is inferred from sidebands 121 ± 5 MHz from the carrier peak. The middle graph is the signal (in red) fitted to a combination of three Lorentzian peaks (in blue); the bottom graph shows the three fitted peaks separately; and the top graph is the residual between the signal and the fit. The FSR, estimated from the cavity length of approximately 40 ± 10 µm, is 3.75 ± 1.0 THz. This leads to an estimated finesse of $47{,}000 \pm 10{,}000$.

inside the chuck which exposed them to dirt. Fortunately, despite all this, we were able to find a suitable multimode fibre. However, when it was being swapped out of the v-groove, the Blu-Tack unfortunately snapped the tip off. Since the fibre we could not find a suitable replacement, we moved forward with our attempt to construct a cavity from two single mode fibres.

This initial multimode to single mode cavity was simply a test cavity, so not much data was collected. However, some preliminary transmission spectra were recorded and we were able to extract an estimate of the finesse, as detailed in fig. 8.3. Since this test cavity fibres were ex-

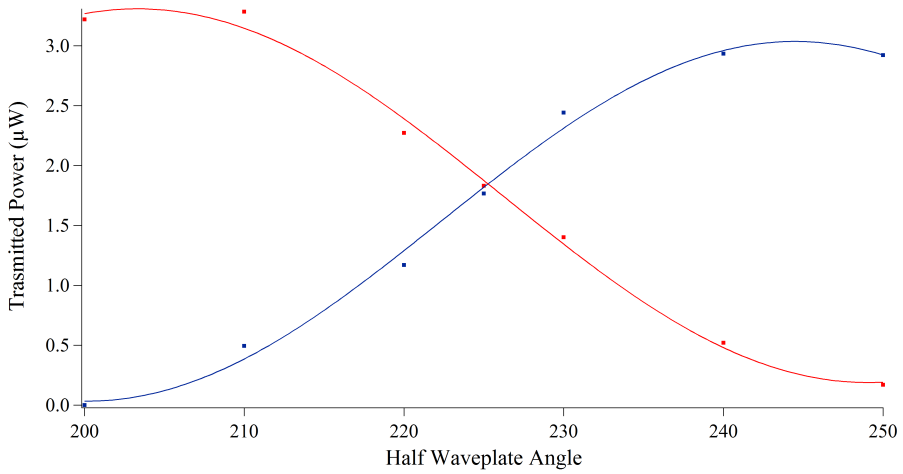

Figure 8.4: Two polarisation dependant peaks exist on the first higher order cavity mode. A $\lambda/2$ waveplate is used to control the polarisation of the 780.24 nm laser light entering the cavity. The two lines shows how the power in each peak varies with the positions of the waveplate, fitted to sine functions. We can see that intensity is transferred from one peak entirely to the other with a 45° rotation of the waveplate. This phenomenon does not appear in the fundamental mode.

tremely dirty by the time any transmission peaks were observed, we obtained a value for the finesse much lower than the theoretical value. We expected the measured finesse from future cavities to be much higher. There was also clear indications of polarisation dependent structures, shown in fig. 8.4. The analysis of both the finesse measurement and the polarisation dependency is discussed in much greater detail in the section below, where more extensive and conclusive data is presented.

8.3 SINGLE MODE TO SINGLE MODE FIBRE-TIP CAVITY

8.3.1 *850 nm Light*

When switching to a cavity constructed from two single mode fibres, the core of the output fibre becomes much smaller. This drastically increases the difficulty in getting any transmitted light, especially with extremely narrow resonance peaks. The difficulty was confounded by the fact it was hard to know exactly if two fibres were able to form a cavity (they may be damaged, dirty, or coated imperfectly). As an intermediary step between switching from the HeNe laser to 780.24 nm laser, we attempt to construct a cavity with 850 nm laser light. The reflectivity of the dielectric coating is around 1.5 orders of magnitude lower at this wavelength, leading to a reduced finesse and wider resonance peaks.

Fig. 8.5 shows the transmission spectrum from a cavity constructed from two single mode fibres. The 850 nm laser was a bare diode with a collimator. It was uncharacterised and likely ran in a highly multi-mode fashion, so it was used only as an intermediary to aid alignment for the 780 nm laser. It proved much easier to find the initial faint transmission signal using this diode. After optimising the transmission power with the translation stage, transfer of the input fibre to the 780.24 nm

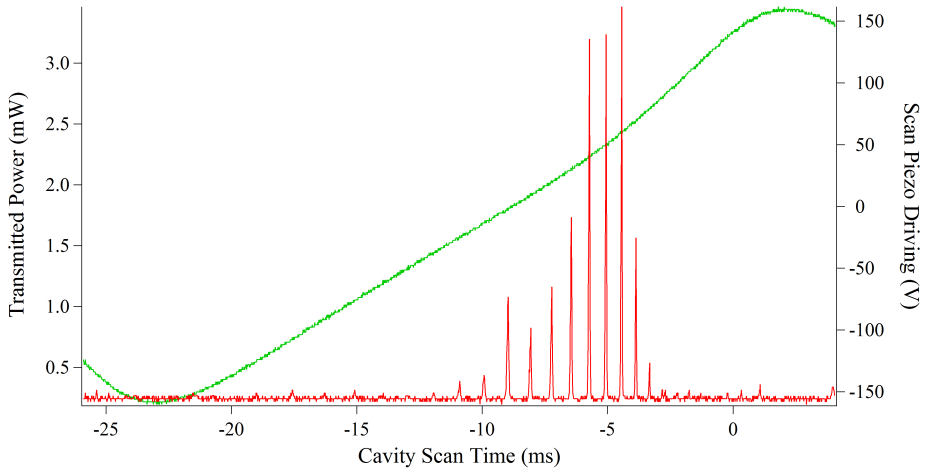

Figure 8.5: The transmission spectrum of a 850 nm diode laser through a cavity formed from two single mode fibre tips. The red line shows how the transmitted intensity varies as we scan the piezo over the range represented by the green line. The scan voltage is read through a 10x attenuated scope probe, so a signal 10x higher is actually sent to the piezo. We see the existence of many resonant modes. By comparison with the cavity mode separation seen in fig 8.7(b) (the cavity length remains similar), it appears that these are most likely due to the multi-mode operation of the diode, rather than higher order transverse cavity modes.

laser usually result in a direct observation of a 780.24 nm transmission spectrum through the cavity.

8.3.2 *780.24 nm Light*

A single mode to single mode fibre-tip cavity was the ultimate goal of the experiment and, after the addition of the 850 nm diode to aid alignment, this was finally realised. It comprised of the two fibres shown in fig. 8.6 with ROCs of 197 µm and 117 µm. The fibres used were

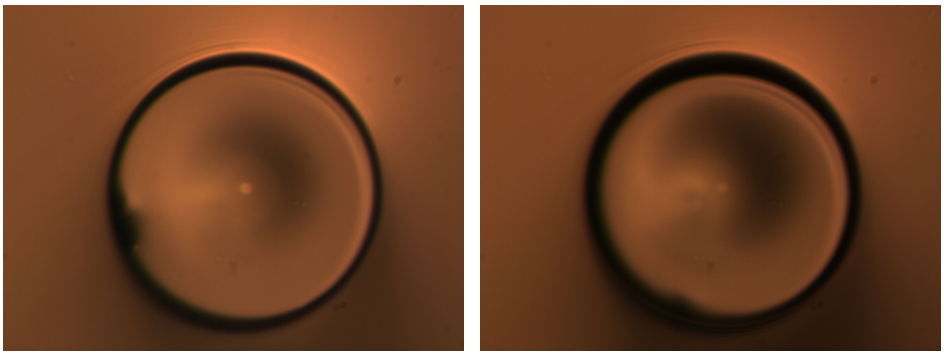

(a) Input Fibre (b) Output Fibre

Figure 8.6: The final cavity was realised with two single mode fibres. (a) The input fibre had a radius of curvature of 197 µm along its major axis with a ratio of 0.94 between the ROC along its major and minor axes. The diameter of the concave indentation was 37 µm with a depth of 2.0 µm. (b) The output fibre had a radius of curvature of 117 µm along its major axis with the ratio being 0.85 between its major and minor axes. The diameter was 36 µm and the depth was 2.8 µm.

prepared extremely carefully and never moved after being placed into the v-grooves, providing a fantastic opportunity to properly classify the characteristics of a single mode to single mode fibre-tip cavity.

The first step was to obtain an accurate estimate for the finesse of such a cavity. A naive method would have been to simply divide the measured value for the FSR by the measured value of the FWHM. We can obtain the FSR from the transmission spectrum shown in fig. 8.7 by measuring the distance between fundamental peaks; and we can measure the FWHM by scanning over a much smaller distance with the piezo and zooming in on one particular peak. Unfortunately, due to the non linearity and the hysteresis effect of the shear piezo, these measurements would not be on the same scale. Although one way to

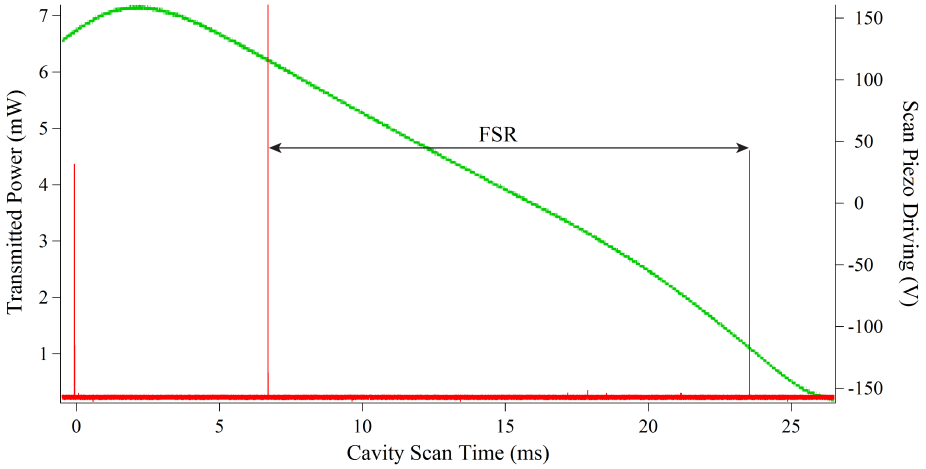

(a) 780.24 nm Transmission Spectrum

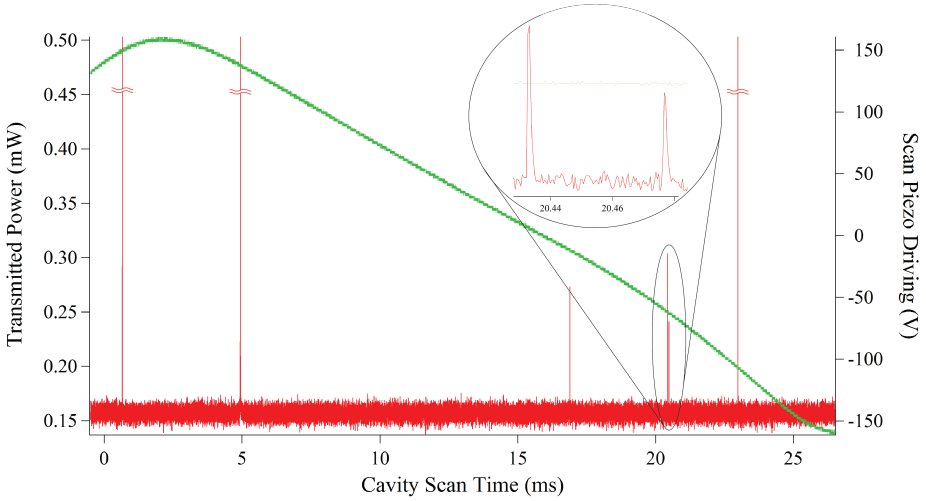

(b) High Order Modes

Figure 8.7: (a) The transmission spectrum of a 780.24 nm laser through a cavity constructed from two single mode fibres. The red line shows how the transmitted intensity varied as we scanned the piezo over the range represented by the green line. The scan voltage is read through a 10x attenuated scope probe, so a signal 10x higher is actually sent to the piezo. We can see clearly two fundamental modes over one FSR, with a third visible as the piezo scans the other way. (b) A version of the transmission spectrum on a more sensitive signal scale, where the fundamental mode is too large to fit. This enables us to better see the higher order transverse modes of the cavity. The bubble contains a zoomed in view of the TEM_{10} and TEM_{01} modes.

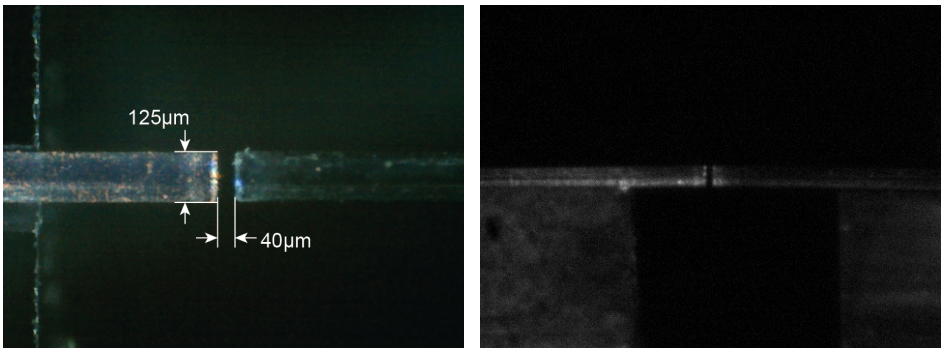

(a) Top View (b) Side View

Figure 8.8: (a) A birds eye view of the cavity. Scattered laser light is visible emanating from the input fibre. We can infer a fibre separation of 40 ± 5 µm by comparison with the known fibre diameter of 125 µm. (b) A horizontal side view of the cavity.

proceed would be to fully characterise the scan of the piezo for different voltages (under a load similar to that used for the cavity) and attempt a theoretical scale correction of the FSR and FWHM measurements, a simpler way exists to estimate the finesse.

From eqn. 5.4, $\Delta\omega_{FSR} = 2\pi\frac{c}{2L}$, we see that we can obtain an value for the FSR of a cavity with an estimate of the cavity length L. Fig. 8.8 shows us photographs of the cavity taken using the cameras set up to observe the cavity. From the known diameter of the bare fibre (125 µm) we can infer the cavity length is $\sim 40 \pm 5$ µm, translating to a FSR of 3.75 ± 0.5 THz. To obtain a measurement for the FWHM of the fundamental mode, we require a known scale for comparison. For this we introducing a low amplitude 110 ± 5 MHz current modulation into the 780 nm laser, creating sidebands in the transmission spectrum 110 MHz

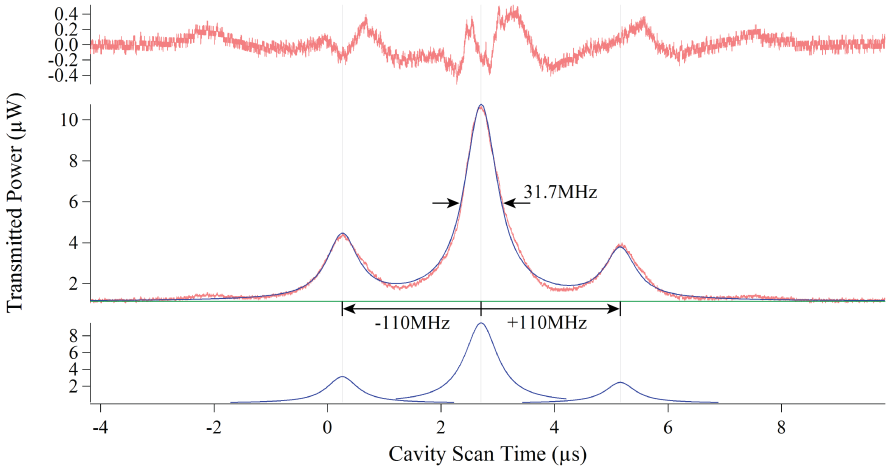

Figure 8.9: The transmission spectrum of 780.24 nm laser light through a single mode to single mode fibre-tip cavity, close to the fundamental mode. The laser signal is superimposed with a 110 ± 5 MHz modulation in frequency, creating two sidebands in the transmission. Triple peak fitting is used to determine the FWHM of the carrier peak, using the position of the sidebands as reference frequencies. The middle graph is the signal (in red) fitted to a combination of three Lorentzian peaks (in blue); the bottom graph shows the three fitted peaks separately; and the top graph is the residual between the signal and the fit.

away from the main peak. In fig. 8.9 we use a multi-peak fit algorithm to fit three Lorentzian profiles to the recorded data. Comparing how far the peaks are from each other to the width of the main peak we estimate the FWHM of the fundamental mode to be 31.7 ± 1.5 MHz. Dividing the FSR by the FWHM gives us a finesse of around $120{,}000 \pm 15{,}000$. This agrees, within experimental error, with the theoretical finesse of 130,000 for mirror coatings of 12 ppm transmission and 12 ppm losses (as calculated in table 6.1).

Zooming in on one of the higher order modes, we see the same polarisation dependent structure as for the multimode cavity. Fig. 8.10

shows two distinct peaks 139 MHz apart. The distribution of the power between these peaks can be controlled using waveplates to control the polarisation of the input laser light.

One possible explanation of this effect is the birefringence associated with the combination of the concave profile of the fibre tip and the crystalline structure of the dielectric coating. The usual rigid structure of the dielectric deposit is compressed at the surface since it is curing upwards to match the concave fibre tip. The resulting stress causes a small birefringence along the radial axis of the mirror. In the ideal case where both mirrors are perfectly spherical and coaxial, the horizontal and vertical formed would be degenerate. This degeneracy is lifted by the eccentricity of the fibre tips, implying that the curvatures along the major and minor axes are different, and therefore the horizontal and vertical polarisation modes experience slightly different path lengths within the cavity. The exact shape of the possible modes will depend on the curvatures and eccentricities of the two mirrors, as well as how they are oriented with respect to each other (the major axes of the two mirrors are unlikely to be parallel). The measured 139 MHz between the two peaks would be consistent with the 200 MHz splitting observed [37] for the same effect.

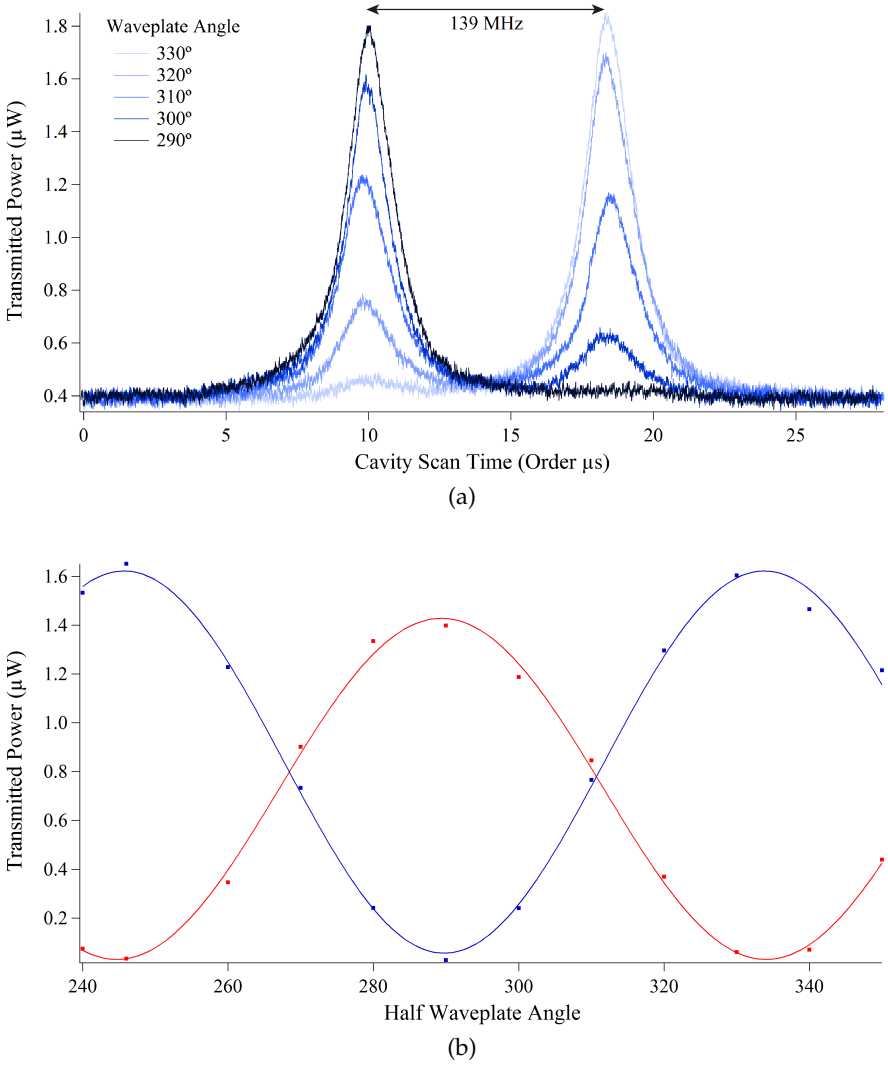

Figure 8.10: Two polarisation dependant peaks exist on the first higher order cavity mode. A $\lambda/2$ waveplate is used to control rotate the linear polarised light entering the cavity. (a) This shows how power is transferred from one peak to the other as the waveplate is rotated. The separation of the peaks is 139 MHz. (b) A graph showing how the power in each peak varies with the positions of the waveplate, fitted to sine functions. The red line is the transmission intensity of the right peak, and the blue of the left. Power is transferred entire from one peak to the other with a 45° rotation of the waveplate.

Another possible explanation for our observations in fig. 8.10 is that these are the TEM_{10} and TEM_{01} modes; and that light of a particular polarisation couples better into one than the other. We can discount this theory based on the separation of the peaks. A quick application of eqn. 5.21 for mirrors with a ROC of 197 µm along the major axis and 0.94×197 µm along the minor axis (which is the geometry of on of the fibre tips used in our experiment), shows that we would expect a splitting of around 25 GHz between the TEM_{10} and TEM_{01} modes. Although the exact value of this would depend on the geometry of the other fibre, and the orientation of the two fibres with respect to each other, it is much greater than the 139 MHz we observe.

It is interesting that we do not observe this effect in the fundamental mode of the cavity. There is only one peak which does change not depending on the polarisation of the input light. This leads us to believe that the birefringence has a minimal effect on the TEM_{00} mode in our system. Hopefully meaning that the modes of orthogonal linear polarisation for TEM_{00} are degenerate in our system, which is advantageous for experiments where quantum information is coded in the emitted photons [77, 78]. If the effect is small and unresolvable compared to the linewidth of the cavity, it could still cause an increase in the observed

FWHM, meaning that the actually finesse of the cavity may be even higher than the 120,000 we measured.

Another group has also observed non-degenerate polarisation modes [39]. The mode splitting ranges from ~ 30 MHz to a few GHz and is not constant for different TEM modes within a cavity. They replace their multimode output fibre, since it does not preserve the cavity mode, with a mirror fabricated on superpolished substrate. The mirror was coated with the same coating as for the fibre tips, and allows them to view the geometry of the cavity mode with a CCD camera while measuring the transmission. Further investigation into this area of our experiment is needed for a more definitive picture.

8.4 OPTOMECHANICAL BISTABILITY

When we scan the cavity length using an optical power above a certain threshold, or if the piezo scan amplitude is too small (resulting in a slower change in cavity length), we observe a strong optical bistability. This is induced by the absorption of a small fraction of the intracavity power into the mirror coatings, which causes local heating and thermal expansion of the mirror and the fibre.

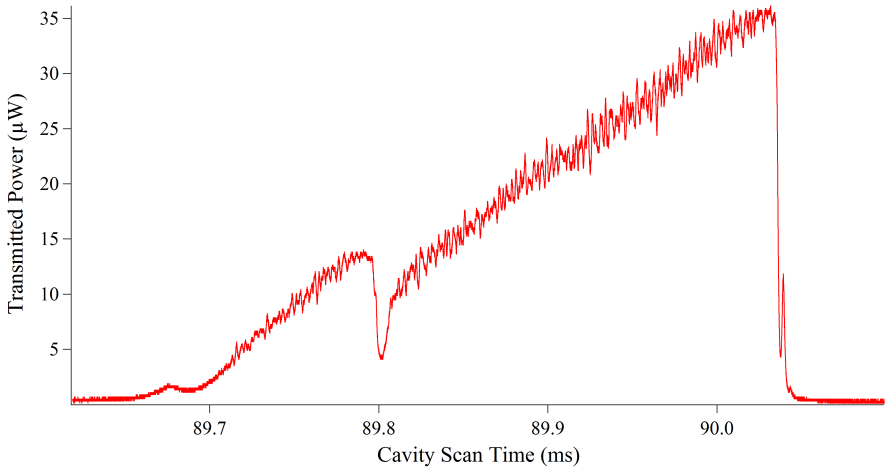

(a) Increasing Cavity Length

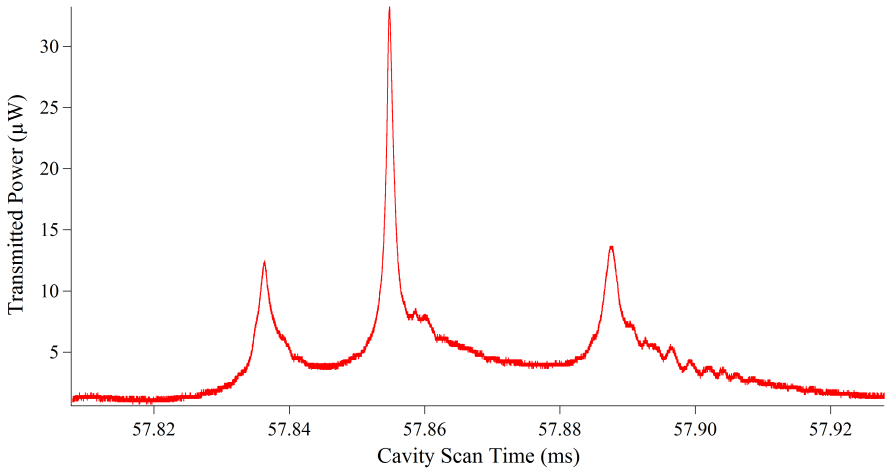

(b) Decreasing Cavity Length

Figure 8.11: This figure shows the difference in transmission the 780.24 nm laser through a single mode to single mode fibre-tip cavity, as the cavity length is (a) increased and (b) decreased. The scan is over the fundamental mode of the cavity, and includes sidebands at 110 MHz. The discrepancy in observed signal is explained by the absorption of intercavity power into the mirror coatings, which cause heating and thermal expansion of the mirror and fibre. Notice that the time scale of (a) is much longer than that of (b). This corresponds to the thermal expansion compensating for cavity length increase in the first case, broadening the peaks; and aiding the cavity length decrease in the latter case, narrowing the peaks.

Fig. 8.11 shows the transmission spectrum of a 780.24 nm laser through the cavity as it is scanned over increasing and decreasing cavity lengths. For scans towards increasing cavity length, we observe a strong broadening of the resonance lines, showing a almost linear increase followed by a sharp drop. This can be explained by the expansion of the substrate compensating for the length increase from the scanning piezo. For scans towards decreasing cavity length, we see a very narrow peak. This corresponds to the cavity length decrease being aided by the thermal expansion, and 'pushing' the cavity across the resonance. These results are very similar to those documented in [37], where a detailed analysis of the effect can be found.

For the measurements made in fig. 8.9 and fig. 8.10, we used a neutral density filter wheel to decrease the intensity of light going into the cavity, until the scans towards increasing and decreasing cavity length produced the identical transmission peaks.

Part III

CONCLUSION

9

TOWARDS A QUANTUM NETWORK

In this thesis, we have demonstrated many of the essential elements for constructing a quantum network. Our DMD based optical dipole trap setup has provided a flexible scheme for the manipulation and transport of neutral atoms. Individual trapping sites within a large array can be controlled independently, which is essential for a scalable system.

With the fibre-tip cavity we have demonstrated that a cavity formed of two single mode fibres is possible, allow us to preserve the optical mode structure of the emitted photon. The cavity offers a high measured finesse of 120,000 and exhibits degeneracy of the linearly polarisation modes within the TEM_{00}.

9.1 IMPROVEMENTS AND OUTLOOK

Many of the improvements for the DMD experiment have already been discussed throughout this thesis. My friend and colleague, Dustin Stuart, has been in charge of implementing the changes to the setup outlined in Chapter 6. The dielectric mirror has been removed and we operate a free space MOT. The DMD is now in a holographic configuration, rather than direct imaging. With this improved setup, we have been able to get to the single atom regime and are now able to trap an array of single atoms. The next step is to attempt transport of individual atom and introduce our characterised fibre-tip cavity into the system.

On the cavity side, the main improvement would be a better translation stage which offers precise and predictable control over both the angle and position of the fibres. A scheme to lock the cavity to the 780.24 nm must be tested before we can combine it with the DMD experiment. For future fabrication, a better mounting system would be advised. The chucks holding the fibres for coating should be constructed from aluminium (or a material with a similarly low outgassing rate) in the first instance. It would be ideal if the scheme was designed in such a way that these chucks could be easily attached to and removed from

the shear piezo without removing the fibres from them. This would minimise the risk of damaging or destroying the coated fibre tips and allow many fibre-tip cavities to be tested and characterised in a safe and expedient manner.

Fibre-tip cavities have already been put into good use for experiments in various parts of atomic physics. Our collaborators at E.N.S. use them for detecting atoms on atom chips [79]. At Imperical College London, the group of Ed Hinds have constructed microcavities using one flat fibre tip mirror and an arrays of concave mirrors fabricated in silicon [80] with a variety of applications. While both the groups of Rainer Blatt [39] and Mattias Keller [38] apply fibre tip cavities to ion trap quantum computation experiments with a view to adding ions as nodes to quantum networks. With the inclusion of our new single mode to single mode fibre tip cavities we can now preserve phase information on any photons emitted from these cavity experiments and we can begin to show real promise towards constructing a quantum network. These cavities can also be implemented in the whole host of existing cavity experiments (highlighted in the introduction) which have taken steps towards a quantum network, such as single photon pistols, quantum teleportation schemes and remote entanglement experiments. They can add the benefit of increased atom-cavity coupling, take advantage of

the fact the output photon is already directly coupled into a fibre, or applied where their small form factor aids the setup of the experiment.

BIBLIOGRAPHY

[1] P. W. Shor. Polynomial-time algorithms for prime factorization and discrete logarithms on a quantum computer. *SIAM Journal on Scientific Computing*, 26:1484–1509, 1997.

[2] L. K. Grover. Quantum computers can search arbitrarily large databases by a single query. *Physical Review Letters*, 79:4709–4712, 1997.

[3] S. Lloyd. Universal quantum simulators. *Science*, 273:1073–1078, 1996.

[4] B. P. Lanyon, C. Hempel, D. Nigg, M. Müller, R. Gerritsma, F. Zähringer, P. Schindler, J. T. Barreiro, M. Rambach, G. Kirchmair, M. Hennrich, P. Zoller, R. Blatt, and C. F. Roos. Universal digital quantum simulation with trapped ions. *Science*, 334:57–61, 2011.

[5] J. Simon, W. S. Bakr, R. Ma, M. E. Tai, P. M. Preiss, and M. Greiner. Quantum simulation of antiferromagnetic spin chains in an optical lattice. *Nature*, 472:307–312, 2011.

[6] M. A. Nielson and I. L. Chuang. *Quantum Computation and Quantum Information*. Cambridge University Press, 2000.

[7] D. Deutsch. Quantum theory, the church-turing principle and the universal quantum computer. *Proceedings of the Royal Society of London A*, 400:97–117, 1985.

[8] D. P. DiVicenzo. The physical implementation of quantum computation. *Fortschritte der Physik*, 48:771, 2000.

[9] M. Saffman, T. G. Walker, and K. Mølmer. Quantum information with rydberg atoms. *Review of Modern Physics*, 82:2313–2363, 2010.

[10] A. Gaëtan, Y. Miroshnychenko, T. Wilk, A. Chotia, M. Viteau, D. Comparat, P. Pillet, A. Browaeys, and P. Grangier. Observation of collective excitation of two individual atoms in the rydberg blockade regime. *Nature Physics*, 5:115–118, 2009.

[11] D. Loss and D. P. DiVincenzo. Quantum computation with quantum dots. *Physical Review A: Atomic, Molecular, and Optical Physics*, 57:120, 1998.

[12] A. Kiraz, M. Atatüre, and A. Imamoğlu. Quantum-dot single-photon sources: Prospects for applications in linear optics quantum-information processing. *Physical Review A: Atomic, Molecular, and Optical Physics*, 69:032305, 2004.

[13] A. Imamoğlu, D. D. Awschalom, G. Burkard, D. P. DiVincenzo, D. Loss, M. Sherwin, and A. Small. Quantum information processing using quantum dot spins and cavity qed. *Physical Review Letters*, 83:4204, 1999.

[14] A. Wallraff, D. I. Schuster, A. Blais, L. Frunzio, R.-S. Huang, J. Majer, S. Kumar, S. M. Girvin, and R. J. Schoelkopf. Strong coupling of a single photon to a superconducting qubit using circuit quantum electrodynamics. *Nature*, 431:162–167, 2004.

[15] M. Steffen, M. Ansmann, R. C. Bialczak, N. Katz, E. Lucero, R. McDermott, M. Neeley, E. M. Weig, A. N. Cleland, and J. M. Martinis. Measurement of the entanglement of two superconducting qubits via state tomography. *Science*, 313:1423–1425, 2006.

[16] H. J. Kimble. The quantum internet. *Nature*, 453:1023–1030, 2008.

[17] P. Zoller, Th. Beth, D. Binosi, R. Blatt, H. Briegel, D. Bruss, T. Calarco, J. I. Cirac, D. Deutsch, J. Eisert, A. Ekert, C. Fabre, N. Gisin, P. Grangiere, M. Grassl, S. Haroche, A. Imamoglu, A. Karlson, J. Kempe, L. Kouwenhoven, S. Kröll, G. Leuchs, M. Lewenstein, D. Loss, N. Lütkenhaus, S. Massar, J. E. Mooij, M. B. Plenio, E. Polzik, S. Popescu, G. Rempe, A. Sergienko, D. Suter, J. Twamley, G. Wendin, R. Werner, A. Winter, J. Wrachtrup, and A. Zeilinger. Quantum information processing and communication: Strategic report on current status, visions and goals for research in europe. *European Physics Journal D*, 36:203–228, 2005.

[18] J. I. Cirac and P. Zoller. Quantum computations with cold trapped ions. *Physical Review Letters*, 74:4091, 1995.

[19] R. Blatt and D. Wineland. Entangled states of trapped atomic ions. *Nature*, 453:1008–1015, 2008.

[20] A. Myerson, D. Szwer, S. Webster, D. Allcock, M. Curtis, G. Imreh, J. Sherman, D. Stacey, A. Steane, and D. Lucas. High-fidelity readout of trapped-ion qubits. *Physical Review Letters*, 100:200502, 2008.

[21] D. Heine, M. Wilzbach, T. Raub, B. Hessmo, and J. Schmiedmayer. Integrated atom detector: Single atoms and photon statistics. *Physical Review A: Atomic, Molecular, and Optical Physics*, 79:021804, 2009.

[22] J. Reichel and V. Vuletic. *Atom Chips*. Wiley, 2011.

[23] M. Karski, L. Förster, J.-M. Choi, A. Steffen, W. Alt, D. Meschede, and A. Widera. Quantum walk in position space with single optically trapped atoms. *Science*, 325:174–177, 2009.

[24] J. Beugnon, C. Tuchendler, H. Marion, A. Gaëtan, Y. Miroshnychenko, Y. R. P. Sortais, A. M. Lance, M. P. A. Jones, G. Messin, A. Browaeys, and P. Grangier. Two-dimensional transport and transfer of a single atomic qubit in optical tweezers. *Nature Physics*, 3:696–699, 2007.

[25] T. Wilk, S. C. Webster, A. Kuhn, and G. Rempe. Single-atom single-photon quantum interface. *Science*, 317:488–490, 2007.

[26] P. B. R. Nisbet-Jones, J. Dilley, D. Ljunggren, and A. Kuhn. Highly efficient source for indistinguishable single photons of controlled shape. *New Journal of Physics*, 13:103036, 2011.

[27] J. Dilley, P. B. R. Nisbet-Jones, B. W. Shore, and A. Kuhn. Single-photon absorption in coupled atom-cavity systems. *Physical Review A: Atomic, Molecular, and Optical Physics*, 85:023834, 2012.

[28] R. Hughes and T. Heinrichs. Quantum computation roadmap. Technical report, Los Alamos National Laboratory, 2004.

[29] R. Raussendorf and H. J. Briegel. A one-way quantum computer. *Physical Review Letters*, 86:5188, 2001.

[30] A. Reiserer, N. Kalb, G. Rempe, and S. Ritter. A quantum gate between a flying optical photon and a single trapped atom. *Nature*, 508:237–240, 2014.

[31] S. M. Spillane, T. J. Kippenberg, K. J. Vahala, K. W. Goh, E. Wilcut, and H. J. Kimble. Ultrahigh-q toroidal microresonators for cavity quantum electrodynamics. *Physical Review A: Atomic, Molecular, and Optical Physics*, 71:013817, 2005.

[32] C. Wuttke, G. D. Cole, and A. Rauschenbeutel. Optically active mechanical modes of tapered optical fibers. *Physical Review A: Atomic, Molecular, and Optical Physics*, 88:061801, 2013.

[33] H.-Y. Ryu, J.-L. Hwang, and Y.-H. Lee. The smallest possible whispering-gallery-like mode in the square lattice photonic-crystal slab single-defect cavity. *IEEE Journal of Quantum Electronics*, 39:314–322, 2003.

[34] Z. Di, H. V. Jones, P. R. Dolan, S. M. Fairclough, M. B. Wincott, J. Fill, G. M. Hughes, and J. M. Smith. Controlling the emission from semiconductor quantum dots using ultra-small tunable optical microcavities. *New Journal of Physics*, 14:103048, 2012.

[35] A. N. Vamivakas, C.-Y. Lu, C. Matthiesen, Y. Zhao, S. Fält, A. Badolato, and M. Atatüre. Observation of spin-dependent quantum jumps via quantum dot resonance fluorescence. *Nature*, 467:297–300, 2010.

[36] Y. Colombe, T. Steinmetz, G. Dubois, F. Linke, D. Hunger, and J. Reichel. Strong atom-field coupling for bose-einstein condensates in an optical cavity on a chip. *Nature*, 450:272–276, 2007.

[37] D. Hunger, T. Steinmetz, Y. Colombe, C. Deutsch, T. W. Hänsch, and J. Reichel. A fiber fabry-perot cavity with high finesse. *New Journal of Physics*, 12:065038, 2010.

[38] H. Takahashi, A. Wilson, A. Riley-Watson, F. Orucevic, N. Seymour-Smith, M. Keller, and W. Lange. An integrated fiber trap for single-ion photonics. *New Journal of Physics*, 15:053011, 2013.

[39] B. Brandstätter, A. McClung, K. Schüppert, B. Casabone, K. Friebe, A. Stute, P. O. Schmidt, C. Deutsch, J. Reichel, R. Blatt, and T. E. Northup. Integrated fiber-mirror ion trap for strong ion-cavity coupling. *Review of Scientific Instruments*, 84:123104, 2013.

[40] D. Hunger, C. Deutsch, R. J. Barbour, R. J. Warburton, and J. Reichel. Laser micro-fabrication of concave, low-roughness features in silica. *AIP Advances*, 2:012119, 2012.

[41] C. Muldoon. *Control and Manipulation of Cold Atoms Trapped in Optical Tweezers*. PhD thesis, University of Oxford, 2012.

[42] C. Muldoon, L. Brandt, J. Dong, D. Stuart, E. Brainis, M. Himsworth, and A. Kuhn. Control and manipulation of cold atoms in optical tweezers. *New Journal of Physics*, 14:073051, 2012.

[43] L. Brandt. *Trapping of Rubidium Atoms using Optical Tweezers*. PhD thesis, University of Oxford, 2011.

[44] L. Brandt, C. Muldoon, T. Thiele, J. Dong, E. Brainis, and A. Kuhn. Spatial light modulators for the manipulation of individual atoms. *Applied Physics B: Lasers and Optics*, 102:443–450, 2011.

[45] C. Marr, A. Beige, and G. Rempe. Entangled-state preparation via dissipation-assisted adiabatic passages. *Physical Review A: Atomic, Molecular, and Optical Physics*, 68:033817–033828, 2003.

[46] C. J. Foot. *Atomic Physics*. Oxford University Press, 2004.

[47] S. Wildermuth, P. Krüger, C. Becker, M. Brajdic, S. Haupt, A. Kasper, R. Folman, and J. Schmiedmayer. Optimized magneto-optical trap for experiments with ultracold atoms near surfaces. *Physical Review A*, 69:030901–030905, 2004.

[48] J. Reichel. Microchip traps and bose-einstean condensation. *Applied Physics B: Lasers and Optics*, 74:469–487, 2002.

[49] P. D. Lett, W. D. Phillips, S. L. Rolston, C. E. Tanner, R. N. Watts, and C. I. Westbrook. Optical molasses. *Journal of the Optical Society of America*, 6:2084–2107, 1989.

[50] N. Schlosser, G. Reymond, I. Protsenko, and P. Grangier. Sub-poissonian loading of single atoms in a microscopic dipole trap. *Nature*, 411:1024–1027, 2001.

[51] N. Schlosser, G. Reymond, and P. Grangier. Collisional blockade in microscopic optical dipole traps. *Physical Review Letters*, 89:023005, 2002.

[52] T. Grünzweig, A. Hilliard, M. McGovern, and M. F. Andersen. Near-deterministic preparation of a single atom in an optical microtrap. *Nature Physics*, 6:951–954, 2010.

[53] D. A. Steck. Rubidium 87 d line data. Technical report, Los Alamos National Laboratory - http://steck.us/alkalidata, 2001.

[54] E. D. Black. An introduction to pound-drever-hall laser frequency stabilization. *American Journal of Physics*, 69:79, 2001.

[55] T. G. Tiecke, J. D. Thompson, N. P. de Leon, L. R. Liu, V. Vuletic, and M. D. Lukin. Nanophotonic quantum phase switch with a single atom. *Nature*, 508:241–244, 2014.

[56] P. B. R. Nisbet-Jones. *Shaping Single Photons*. PhD thesis, University of Oxford, 2012.

[57] A. E. Siegman. *Lasers*. University Science Books, 1990.

[58] Wikipedia. Gaussian beam page.

[59] M. Fox. *Quantum Optics*. Oxford University Press, 2006.

[60] E. Jayne and F. Cummings. Comparison of quantum and semi-classical radiation theories with application to a beam maser. *IEE Proceedings*, 51:89–109, 1963.

[61] T. Steinmetz, Y. Colombe, D. Hunger, T. W. Hänsch, A. Balocchi, R. J. Warburton, and J. Reichel. A stable fiber-based fabry-perot cavity. *Applied Physics Letters*, 89:111110, 2006.

[62] J. Dong. Redesign of the dmd dipole trap experiment. Technical report, University of Oxford, 2010.

[63] C. J. Hood, H. J. Kimble, and J. Ye. Characterization of high-finesse mirrors: Loss, phase shifts, and mode structure in an optical cavity. *Physical Review A: Atomic, Molecular, and Optical Physics*, 64:033804, 2001.

[64] L. Moore. Single mode fiber coupling: Sensitivities and toleranc-ing. Technical report, University of Arizona, 2006.

[65] P. Maunz, T. Puppe, I. Schuster, N. Syassen, P. W. H. Pinkse, and G. Rempe. Cavity cooling of a single atom. *Nature*, 428:50–52, 2004.

[66] K. M. Nowak, H. J. Baker, , and D. R. Hall. Efficient laser polishing of silica micro-optic components. *Applied Optics*, 45:162–171, 2006.

[67] E. Mendez, K. M. Nowak, H. J. Baker, F. J. Villarreal, and D. R. Hall. Localized co_2 laser damage repair of fused silica optics. *Applied Optics*, 45:5358–5367, 2006.

[68] F. Bayle and J.-P. Meunier. Efficient fabrication of fused-fiber bi-conical taper structures by a scanned co_2 laser beam technique. *Applied Optics*, 44:6402–6411, 2005.

[69] C. Deutsch. High finesse fibre fabry-pérot resonators: Production, characterization and application. Master's thesis, École Normale Supérieure, 2008.

[70] D. W. Vernooy, V. S. Ilchenko, H. Mabuchi, E. W. Streed, and H. J. Kimble. High-q measurements of fused-silica microspheres in the near infrared. *Optical Letters*, 23:247–249, 1998.

[71] D. K. Armani, T. J. Kippenberg, S. M. Spillane, and K. J. Vahala. Ultra-high-q toroid microcavity on a chip. *Nature*, 421:925–928, 2003.

[72] J. M. Bennett. Recent developments in surface roughness characterization. *Measurement Science and Technology*, 3:1119, 1992.

[73] P Danielson. Choosing the right vacuum materials. Technical report, The Vacuum Lab, 2006.

[74] R. Gehr, J. Volz, G. Dubois, T. Steinmetz, Y. Colombe, B. L. Lev, R. Long, J. Estève, and Jakob Reichel. Cavity-based single atom preparation and high-fidelity hyperfine state readout. *Physical Review Letters*, 104:203602, 2010.

[75] S. Olmschenk, D. N. Matsukevich, P. Maunz, D. Hayes, L.-M. Duan, and C. Monroe. Quantum teleportation between distant matter qubits. *Science*, 323:486–489, 2008.

[76] E. Knill, R. Laflamme, and G. J. Milburn. A scheme for efficient quantum computation with linear optics. *Nature*, 409:46–52, 2001.

[77] S. Ritter, C. Nölleke, C. Hahn, A. Reiserer, A. Neuzner, M. Uphoff, M. Mücke, E. Figueroa, J. Bochmann, and G. Rempe. An elementary quantum network of single atoms in optical cavities. *Nature*, 484:195, 2012.

[78] A. Stute, B. Casabone, P. Schindler, T. Monz, P. O. Schmidt, B. Brandstätter, T. E. Northup, and R. Blatt. Tunable ion-photon entanglement in an optical cavity. *Nature*, 485:482–485, 2012.

[79] J. Volz, R. Gehr, G. Dubois, J. Estève, and J. Reichel. Measurement of the internal state of a single atom without energy exchange. *Nature*, 475:210–213, 2011.

[80] M. Trupke, E.A. Hinds, S. Eriksson, E.A. Curtis, Z. Moktadir, E. Kukharenka, and M. Kraft. Microfabricated high-finesse optical cavity with open access and small volume. *Applied Physics Letters*, 87:211106, 2005.